David B. McCallen, Center Director

The growth of computer power and connectivity, together with advances in wireless sensing and communication technologies, is transforming the field of complex distributed systems. The ability to deploy large numbers of sensors with a rapid, broad-band communication system will enable high-fidelity, near real-time monitoring of complex systems. These technological developments will provide unprecedented insight into the actual performance of engineered and natural environment systems, enable the evolution of many new types of engineered systems for monitoring and detection, and enhance our ability to perform improved and validated large-scale simulations of complex systems.

One of the challenges facing engineering is to develop methodologies to exploit the emerging information technologies. Particularly important will be the ability to assimilate measured data into the simulation process in a way which is much more sophisticated than current, primarily *ad hoc* procedures.
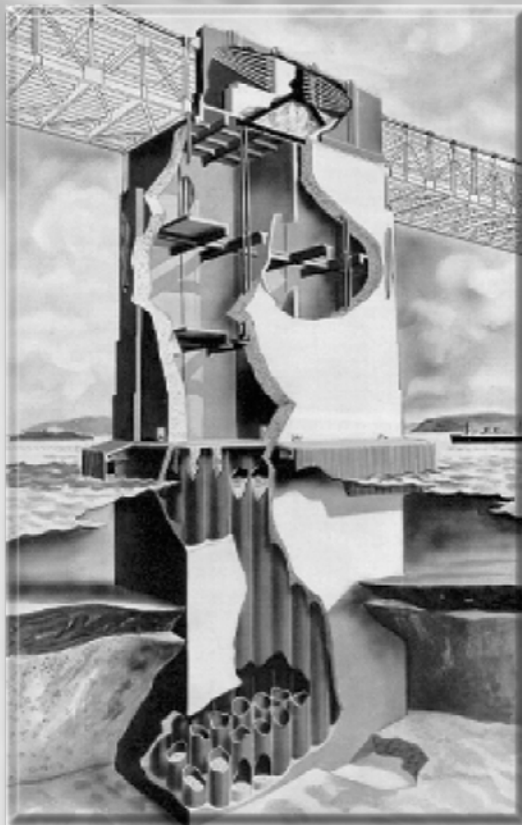
The reports contained in this section on the Center for Complex Distributed Systems describe activities related to the integrated engineering of large complex systems. The first three papers describe recent developments for each link of the integrated engineering process for large structural systems. These include 1) the development of model-based signal processing algorithms which will formalize the process of coupling measurements and simulation and provide a rigorous methodology for validation and update of computational models; 2) collaborative efforts with faculty at the University of California at Berkeley on the development of massive simulation models for the earth and large bridge structures; and 3) the development of wireless data acquisition systems which provide a practical means of monitoring large systems like the National Ignition Facility (NIF) optical support structures.

These successful developments are coming to a confluence in the next year with applications to NIF structural characterizations and analysis of large bridge structures for the State of California. Initial feasibility investigations into the development of monitoring and detection systems are described in the papers on imaging of underground structures with ground-penetrating radar, and the use of live insects as sensor platforms. These efforts are establishing the basic performance characteristics essential to the decision process for future development of sensor arrays for information gathering related to national security.

Center for Complex Distributed Systems

1

1. Center for Complex Distributed Systems

A Reduced-Order Model for Nonlinear Suspension Bridge Analysis

David B. McCallen
Center for Complex Distributed Systems

Abolhassan Astaneh-Asl
Department of Civil and Environmental Engineering
University of California
Berkeley, California

With the proliferation of commercially available software tools for structural mechanics and powerful compute engines, computational simulation of long-span cable-supported bridges is experiencing rapid growth. However, due to the physical size and large number of individual members in these structures, the application of general purpose computational mechanics software may not represent the optimal solution, particularly for computationally intensive nonlinear analyses and parametric studies where multiple simulations are required. We have developed a numerical simulation tool specific to the nonlinear, transient, dynamic analysis of cable-supported bridges. The methodology is predicated on special element technologies which allow a significant reduction in the number of global equations in the bridge system model. The solution of the equations of motion is based on a hybrid implicit/explicit procedure in which the bridge gravity configuration is determined with an implicit solution, and the transient time-stepping solution is based on explicit integration of the equations of motion.

Introduction

In recent years, the design and analysis of large, distributed structural systems has become increasingly reliant on large-scale computational simulation. Linear simulations have been the mainstay of design computations. However, as performance-based design procedures become more prevalent, there will be increased demand for accurate numerical models capable of simulating nonlinear response and ultimate structural collapse.

The computational requirements for nonlinear analyses, which include changes in the global model geometry, impact between adjacent bridge segments, and material inelasticity, can be prohibitive if general purpose finite-element programs are used. This fact begs for efficient nonlinear computational models which allow parametric studies essential to developing a clear understanding of the dynamic bridge response.

In addition to computational difficulties, there continue to be phenomenological issues in the analyses of these important structures. The effects of spatially varying earthquake ground motions;

near-field earthquake ground motions containing long-period ground displacement pulses and permanent ground displacements; and fluid-structure interaction between a bridge and the turbulent atmosphere, are topics for which scientific and engineering understanding are incomplete. Appropriate characterization of damping mechanisms in a long-span cable bridge remains an area of great uncertainty.

A rigorous understanding of the mechanics of cable bridge damping, which discriminates between complex aerodynamic and mechanical damping mechanisms, has yet to be developed, and it remains necessary to rely on simple spectral representations of damping. Spectral damping representations are complicated by the fact that cable bridge dynamics can be very broad-band with long wavelength modes of a flexible deck system on the order of 10- to 15-s periods, and modes of stiff towers on the order of 0.1- to 0.2-s periods.

There have been extensive analytical and numerical studies of the vibrational characteristics of cable-supported bridges undergoing small amplitude, linear vibrations. The early work of Abdel-Ghaffar[1-3] was important in developing

basic understanding of the linear vibratory dynamics of suspension bridges. Abdel-Ghaffar's work developed analytical models for the natural vibrations of suspension bridges and provided insight on the vibrational interactions between towers, cables, and deck systems. As part of a combined simulation and field observation study, Dumanoglu, Brownjohn, and Severn[4] used 2- and 3-D linear computational models to investigate the natural vibrations of the Fatih Sultan Mehmet suspension bridge (Turkey) and extracted a large number of modes for the structure.

Long-span cable bridges are complex and distributed dynamic systems and model validation and parameter calibration (such as selection of appropriate damping forms) must rely on experimentally obtained observational data. The only database currently available for suspension bridges consists of low amplitude, linear vibrations.[5-9]

The cited experimental and computational studies have generally demonstrated the ability of computational models to adequately represent the lower natural modes associated with small amplitude, linear dynamics of a suspension bridge vibrating about the gravity configuration of the system. Due to the complexities and computational difficulties of large-scale nonlinear analyses, and a lack of measured response data in the nonlinear regime, the effect of nonlinearities on cable bridge response has been investigated to a lesser extent.

Abdel-Ghaffar and Rubin[10,11] demonstrated the nonlinearity associated with modal coupling in amplitude-dependent free vibrations of suspension bridges with applications for the Golden Gate and Vincent Thomas Bridges. Computational studies by Nazmy and Abdel-Ghaffar[12,13] have indicated the importance of geometric nonlinearities in cable-stayed bridges with long spans and reinforced the importance of considering the spatial variation of earthquake ground motions.

In addition to research studies, consideration of nonlinearities in cable-supported bridges is beginning to infiltrate into engineering practice. Ingham, Rodriguez and Nadar[14] have described practical design application of nonlinear analysis in the seismic retrofit studies of the Vincent Thomas Bridge.

Further study is necessary to develop a clear understanding of the nonlinear response of long-span bridges to strong ground motions, particularly when the bridge is located in the near-field of a causative earthquake fault where ground motions may contain both high-frequency and significant long-period motions due to near-field effects. There is no existing observational database for this

response regime, and nonlinear computational simulations must play a central role in developing improved understanding.

The objective of our work was the development of a simple and robust computational model for 3-D, nonlinear transient analysis of suspension bridges. The resulting finite-element model accounts for nonlinearities due to finite displacements, material nonlinearities in the bridge members, impact between adjacent bridge segments, and potential rocking and uplift of large caisson foundations.

Unique features of the model include the element technologies, which are tailored to the construction of a reduced-order model with a significant reduction in the global degrees of freedom; and the use of an explicit time-integration scheme for dynamic analyses. The explicit scheme provides a simple and highly reliable nonlinear solution framework for transient nonlinear analyses, particularly when considering the sudden events associated with impact between adjacent bridge segments, sudden tensioning of slack cables, or collapse of bridge components.

The model incorporates an implicit based, automated procedure for nonlinear gravity initialization of the bridge model, which computes the correct bridge geometry and the correct initial stress field in the cable and deck trusses for gravity loading.

The nonlinear model we have developed can be particularly useful for parametric studies aimed at understanding the complex transient response of long-span bridges and the relationship between bridge response and ground motion characteristics. Because of the importance of validating special numerical models, particular attention was paid to comparison of the reduced order model with both experimental data and higher order detailed models.

Progress

Computational Bridge System Model

The research study which motivated development of the computational model consisted of a multidisciplinary seismological and engineering study of the San Francisco-Oakland Bay Bridge (**Fig. 1**). With approximately 280,000 vehicles per day, the Bay Bridge carries the highest traffic volume of any bridge in the United States. The bridge is a critical transportation link and a seismically interesting structure by virtue of its close proximity to major active earthquake faults.

Two new computational tools for numerical simulation of seismic ground motions and structural
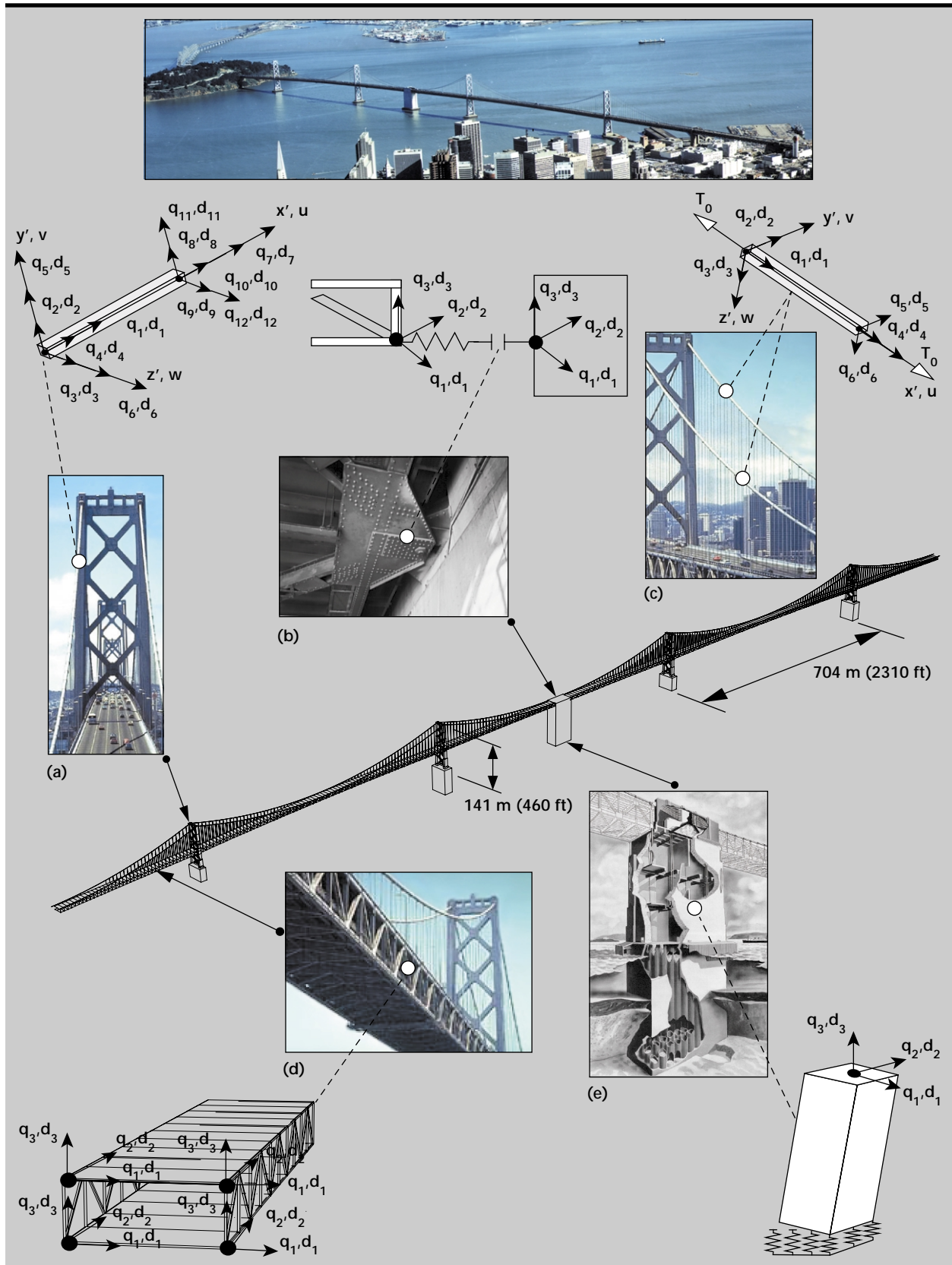
Figure 1. The five elements of the bridge system model. (a) Finite rotation fiber flexure element for the bridge towers; (b) penalty node-to-node contact for deck impact; (c) tension-only two-force member with initial stress for cables; (d) composite membrane, truss, and sway stiffness deck model; (e) caisson block with uplift.

response were developed for this study. A massively parallel, geophysics based finite-difference program has been constructed to model seismic wave propagation.[15,16] The geophysics model, which is described in a companion paper, provides ground motion estimates, including the effects of near-field phenomena such as long-period ground displacement pulses, and coseismic, permanent ground displacements associated with tectonic plate movements.

The second computational tool, and the subject of this paper, consists of the special-purpose finite-element program for nonlinear bridge analysis. The description references the Bay Bridge system. However, the solution algorithms and element technologies described can have broader applicability to other suspension and cable-stayed bridges with appropriate changes in element properties.

The model consists of five major elements, as shown in **Fig. 1**. A finite-rotation, fiber bending element is used to represent the bridge towers. A tension-only cable element with user-defined initial stress represents the bridge cable system. A reduced-order deck model, consisting of a composite combination of truss, membrane, and sway stiffness elements, represents the deck and stiffening truss system. A penalty-based node-to-node contact element captures potential contact and impact between the deck system and towers, and a rocking foundation element represents the large caisson foundations with potential uplift.

Our philosophy was to maintain the greatest possible simplicity in the element formulations and solution algorithms, and to provide a robust algorithm which could handle a multiplicity of strong nonlinearities. An explicit time integration algorithm provided the robustness for strongly nonlinear dynamic problems. Since explicit integration schemes are conditionally stable with the time step size governed by the highest frequency of the simulation model, explicit schemes are typically too costly for long duration dynamic loads such as earthquakes with existing general-purpose finite-element programs. However, the potential advantages of explicit integration are well known for highly nonlinear problems. These advantages include the basic simplicity and reliability of the algorithm when compared with the most efficient quasi-Newton implicit schemes.

Explicit integration provides accuracy and high reliability for large nonlinear structures when strong nonlinearities occur and can readily handle softening systems or contact intensive problems which defy or hamper convergence of implicit integration schemes. Explicit integration is computationally feasible for long duration problems if the element technologies and physical element sizes in the discretized model do not result in prohibitively small time steps. The simple elements developed in this study lead to manageable time steps and thus enable the use of explicit integration. The nonlinear computational elements and algorithms developed have been incorporated into the special purpose finite-element program SUSPNDRS. The methodologies are described briefly in this paper. A complete description, including detailed evaluations of element and software performance, is given elsewhere.[17]

Nonlinear Solution Framework

In the numerical simulation of cable-supported bridge systems subjected to dynamic loads, two distinct steps must be undertaken to obtain the transient solution. The first step is performance of an appropriate static, nonlinear gravity load initialization of the computational model such that the model emulates the correct geometric shape of the bridge with the appropriate forces in the individual bridge deck members, towers, and cable system.

This initialization must take into account the design objectives and construction sequence of the bridge, since the construction procedure can significantly influence gravity-induced forces and the final overall geometrical shape of the bridge. Once the appropriate gravity configuration is achieved, the solution can proceed to a transient dynamic analysis with the static configuration (member forces and model geometry) serving as the initial condition state for the dynamic analysis. The total nonlinear solution must adequately handle both the nonlinear-static and the nonlinear-dynamic solution phases.

Implicit Static Solution. In the computational bridge model, the deformation of the structure is defined by the vector of global displacement components $\{D\}$. For a given set of statically applied external loads on the structure $\{P\}$, the structure is in a state of equilibrium if the external loads equilibrate the internal resisting forces of the structure, denoted $\{Q(\{D\})\}$, and the forces generated by any contact across disjoint parts of the structure (such as expansion joints), denoted $\{\Gamma(\{D\})\}$. In a nonlinear system, the internal and contact forces are nonlinear functions of the system displacements.

Defining a residual vector $\{R(\{D\})\}$ as the difference between the various force components in the direction of each degree of freedom of the model,

$$\{R(\{D\})\} = \{\{Q(\{D\})\} - \{P\} - \{\Gamma(\{D\})\}\} \qquad (1)$$

then an equilibrium configuration of the structure, denoted $\{D^*\}$, results in a null residual vector, such

as R{D*} = 0. If {D*} is the kth approximation to {D*}, then a Taylor series expansion of the residual vector about {D^k} yields,

$$\{R(\{D^*\})\} = \{R(\{D^k\})\}$$

$$+ \left[\frac{\partial \{R(\{D^k\})\}}{\partial D} \right] \{\Delta D\} + o \left\langle \{\Delta D\}^2 \right\rangle \qquad (2)$$

where,

$$\left[\frac{\partial R}{\partial D} \right] = \begin{bmatrix} \frac{\partial Q_1}{\partial D_1} \cdots \frac{\partial Q_1}{\partial D_n} \\ \cdots \cdots \cdots \\ \frac{\partial Q_n}{\partial D_1} \cdots \frac{\partial Q_n}{\partial D_n} \end{bmatrix} - \begin{bmatrix} \frac{\partial \Gamma_1}{\partial D_1} \cdots \frac{\partial \Gamma_1}{\partial D_n} \\ \cdots \cdots \cdots \\ \frac{\partial \Gamma_n}{\partial D_1} \cdots \frac{\partial \Gamma_n}{\partial D_n} \end{bmatrix} . \qquad (3)$$

Neglecting higher order terms in **Eq. 2**, and invoking the fact that {R({D*})} = 0, the incremental displacements are given by,

$$\left[\frac{\partial \{R \langle \{D^k\} \rangle\}}{\partial D} \right] \{\Delta D\} = -\{R \langle \{D^k\} \rangle\} . \qquad (4)$$

The instantaneous stiffness matrix is defined as the immediate rate of change of the internal resisting forces and contact forces with respect to system displacements, thus,

$$\left[K_I(\{D^k\}) \right] = \left[\frac{\partial \{R(\{D^k\})\}}{\partial D} \right] \qquad (5)$$

and the individual terms of this matrix are given by **Eq. 3**. The first matrix in **Eq. 3** represents the stiffness contribution from the structural elements in the bridge model; the second represents the effective stiffness contribution from the penalty-based contact elements activated during contact between disjoint parts. In the absence of contact, the contact stiffness matrix vanishes. The incremental relationship given by **Eq. 4** provides the basis for equilibrium iterations which yield incremental displacements for updating the displacement vector until the nodal force residuals and incremental displacements become acceptably small. In the static solution algorithm implemented in this study, the instantaneous stiffness is completely reformed for each equilibrium iteration, leading to a full Newton-Raphson procedure for equilibrium iterations. Equilibrium iterations proceed until the Euclidean norms of the residual and incremental displacement vectors become acceptably small. In the SUSPNDRS program, the

implicit solution is used for gravity initialization of the bridge system, for other nonlinear static analyses such as push-over tests for a bridge or bridge components, and as a diagnostic tool when implementing new nonlinear elements.

Explicit Dynamic Solution. The transient bridge solution is based on an explicit integration scheme which readily admits arbitrary multiple support earthquake ground motions. The earthquake ground motions are defined by ground displacement time histories at the bridge base support locations referenced to an identical time frame to preserve phasing information across the bridge structure. The coupled equations of motion for the bridge system, constructed from the assembly of element matrices, are given by,

$$[M]\{\ddot{D}(t)\} + [[C_{fsi}]\{\dot{D}(t)\} + [C_{mech}]\{\dot{D}_r(t)\}]$$

$$+ \{Q(\{D(t)\})\} + \{\Gamma(\{D(t)\})\} = \{P_{Boundary}(\{D_{g_i}(t)\})\} \quad (6)$$

where conceptually, $[C_{fsi}]$ defines the damping due to fluid-structure interaction and $[C_{mech}]$ defines the mechanical damping. The vector $\{Q(\{D\})\}$ represents the internal resisting forces of the model elements, vector $\{\Gamma(\{D\})\}$ represents the nodal forces due to contact of disjoint bridge segments, and $\{P_{Boundary}(\{D_{g_i}(t)\})\}$ contains the support point forces generated by applied ground displacements. In **Eq. 6**, the fluid-structure interaction damping forces are assumed proportional to the absolute velocity $\{\dot{D}_r(t)\}$ of the structure and the mechanical damping forces are assumed proportional to the relative velocity $\{\dot{D}_r(t)\}$ of the structure.

The specific form assumed for the bridge energy dissipation, as characterized by the viscous terms in **Eq. 6**, has significant implications for the numerical implementation of the explicit integration procedure for the equations of motion. An appropriate damping form must be inferred from experimentally identified structural damping values. The results of the modal damping observations from several studies[6-9] are constructed in graphical form in **Fig. 2**. In each plot, the experimentally observed damping values are shown as a function of frequency. The experimental data consistently exhibits an inverse relationship between modal damping and modal frequency, the only major difference between the various bridges being the specific amplitude of the damping values. In addition to the experimental values, a solid line is included for each dataset indicating the frequency dependency of damping which would be obtained with an assumption of mass-proportional spectral damping (that is, $[C] = \beta[M]$).

For three of the cases (Golden Gate, Newport, and William Preston), the mass proportional

damping was anchored at the fundamental mode; for the Fatih Sultan Mehmet data, there was a wider scatter and an anchor damping value somewhat lower than the damping of the fundamental mode proved to yield a better fit. For all of the small amplitude vibration data, mass-proportional damping provides a good representation of the observed frequency dependency of damping. While this reveals a general trend in the frequency dependency of the data for these broad-band

Figure 2. Experimentally observed damping in suspension bridges. (a) Golden Gate Bridge (length = 2738 m); (b) Newport Bridge (length = 907 m); (c) William Preston Lane Memorial Bridge (length = 890 m); (d) Fatih Sultan Mehmet Bridge (length = 1510 m); (e) damping overlay for all four bridges.
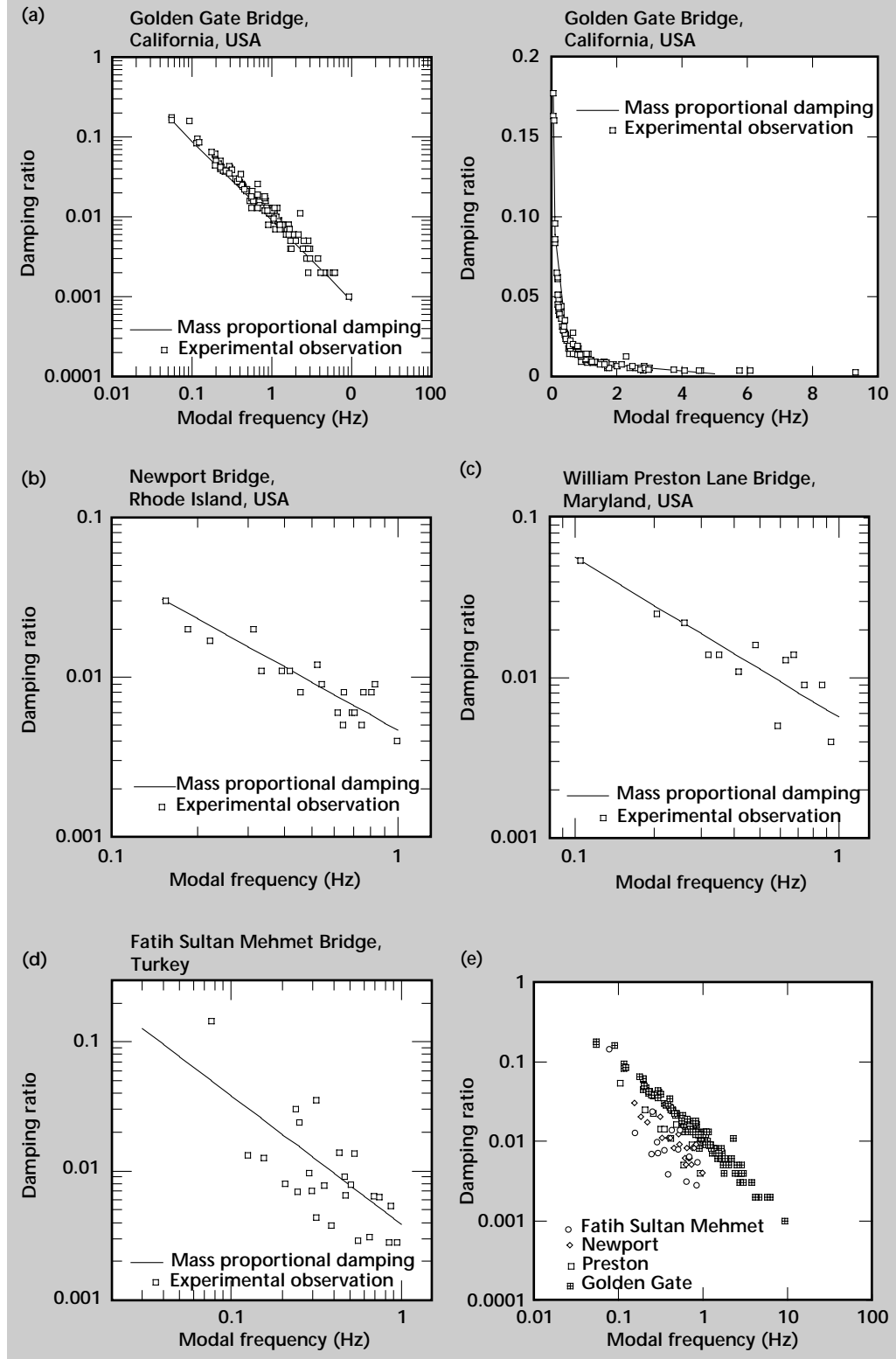
structures, it must be kept in mind that the damping values were obtained from small amplitude vibrational data. In practice, it is necessary to augment the mass proportional damping with some stiffness-proportional damping to ensure high-frequency modes are appropriately damped. This issue is particularly important for explicit time integration schemes where the higher frequency modes are resolved in the model.

For mathematical expediency, and lacking more specific information about the mechanical and aerodynamic partitioning of the damping in cable bridges, an assumption of viscous, absolute velocity-dependent damping was assumed in the computational model. Thus, **Eq. 6** simplifies to,

$$[M]\{\ddot{D}(t)\} + [C]\{\dot{D}(t)\} + \{Q(\{D\})\}$$
$$+\{\Gamma(\{D\})\} = \{P_{Boundary}(\{D_{g_i}(t)\})\} \ . \qquad (7)$$

Traditional central difference formulas provide expressions for the velocity and acceleration,

$$\{\dot{D}\}_n = \frac{1}{2\Delta t}[\{D\}_{n+1} - \{D\}_{n-1}] \qquad (8)$$

$$\{\ddot{D}\}_n = \frac{1}{(\Delta t)^2}[\{D\}_{n+1} - 2\{D\}_n + \{D\}_{n-1}] \qquad (9)$$

where n refers to the nth time step. However, if a stiffness-proportional term is included in the damping matrix,

$$[C] = \alpha[M] + \beta[K] \qquad (10)$$

the damping matrix is non-diagonal and the finite-difference expressions in **Eq. 8** and **Eq. 9** will result in a matrix inversion for each time step of the explicit integration scheme. To avoid matrix inversions, and thus preserve the economy of the explicit integration scheme, an approximation to the velocity is used in place of **Eq. 8**,

$$\{\dot{D}\}_n = \frac{1}{\Delta t}[\{D\}_n - \{D\}_{n-1}] \ . \qquad (11)$$

This expression will result in some accuracy loss in the integration scheme, which is generally insignificant for these structures due to the short time step of the explicit integration scheme.

Combining **Eq. 7**, **Eq. 9**, and **Eq. 11**, yields the recursion relationship for displacement,

$$\frac{1}{\Delta t^2}[M]\{D\}_{n+1} = \left\{ P_{Boundary}\left(D_{g_i}(t) \right)_{n+1} \right\}$$
$$-\{Q(\{D\}_n)\} - \{\Gamma(\{D\}_n)\} + \frac{1}{\Delta t}\left[\frac{2}{\Delta t}[M] - \alpha[M] - \beta[K] \right]\{D\}_n$$
$$+\frac{1}{\Delta t}\left[\alpha[M] + \beta[K] - \frac{1}{\Delta t}[M] \right]\{D\}_{n-1} \quad . \qquad (12)$$

The application of seismic excitation is most easily introduced in these equations by specification of the displacements at the base support points of the structure. Specified displacements are introduced by assigning identity equations for each specified support displacement in **Eq. 12**, yielding,

$$\frac{1}{\Delta t^2}[M]\{D\}_{n+1} = \Delta t^2[M]^{-1}\{D_g\}_{n+1} - \{Q(\{D\}_n)\}$$
$$-\{\Gamma(\{D\}_n)\} + \frac{1}{\Delta t}\left[\frac{2}{\Delta t}[M] - \alpha[M] - \beta[K] \right]\{D\}_n \qquad (13)$$
$$+\frac{1}{\Delta t}\left[\alpha[M] + \beta[K] - \frac{1}{\Delta t}[M] \right]\{D\}_{n-1}$$

where vector $\{D_g\}$ contains the earthquake ground motion displacement time histories of the bridge supports, the terms of which are zero except at the structure support locations. For the Bay Bridge evaluation, the structure is founded directly on bedrock and the support displacement time histories were obtained directly from a massively parallel finite-difference model.[16]

The equations expressed in **Eq. 13** provide the explicit recursion relationships for update of the structural model displacements at time step n+1, based on the displacement vectors at previous time steps n and n–1. Because of the velocity approximation which has been invoked, and the fact that the model mass matrix is always a diagonal due to lumped mass assumptions, no matrix inversions are required for the solution of $\{D\}_{n+1}$. This explicit integration is conditionally stable, with the maximum time step permitted being governed by the Courant limit for the discretization of the particular bridge model at hand. The approximation invoked in **Eq. 11** does effect the integration stability time step, which must be accounted for in the selection of the integration time step.[18]

For earthquake ground motions, there are two fundamental differences between the explicit algorithm defined in **Eq. 13** and traditional seismic analyses methods. In the explicit formulation, ground motion is defined in terms of ground displacement time histories rather than acceleration time histories, and the computed displacement quantities are absolute displacements rather than displacements relative to the ground reference frame.

Element Technologies

With careful construction and appropriate validation, it is often possible to develop an accurate reduced-order model of a bridge system which captures the salient features of the dynamics of the system, yet

results in a significant reduction of the global degrees of freedom relative to a classical discretization from a general-purpose finite-element program.

The element technologies developed were aimed at significantly reducing the number of equations in the global bridge model. The Courant time step limit for stability of the explicit integration scheme depends on the transit time of a stress wave through the smallest elements in the bridge model, and is thus a function of the physical dimensions of the elements in the computational model. To maximize the integration time step, an additional objective was to construct element technologies which resulted in physically large element dimensions.

Tower Flexural Fiber Model. A fiber flexural element was developed for characterization of the bridge towers. The element can also be used for other bridge members which may require a flexural bending element characterization. The element incorporates both geometric and material nonlinearities. The framework for tracking geometry changes and initial stress inclusion are common to the bridge deck truss and cable elements described in a subsequent section.

For 3-D bending with finite (large) rotations, rotations are nonvectorial and must be incrementally updated. The flexure element uses three local element coordinate systems to track both the finite displacements and the finite rotations of the beam segments. Two local coordinate systems rotate and translate with the principal axes of the beam element at each end (the x'', y'', z'' and x''', y''' and z''' axes in **Fig. 3**), and the third updated Lagrangian system (x', y', z') extends between the element end nodes and tracks the overall displacement and rotation of the element.

A fundamental assumption of the element is that incremental rotations occurring between equilibrium iterations in the implicit solution procedure or between time steps in the explicit dynamic solution, are small and can be transformed vectorially between the local coordinate systems. This assumption is easily met for practical problems, particularly with explicit integration where the time steps are quite small. The element also assumes the deformational rotations, for example, the rotations between the x', y', and z' axes and the x'', y'', and z'' axes, are small.
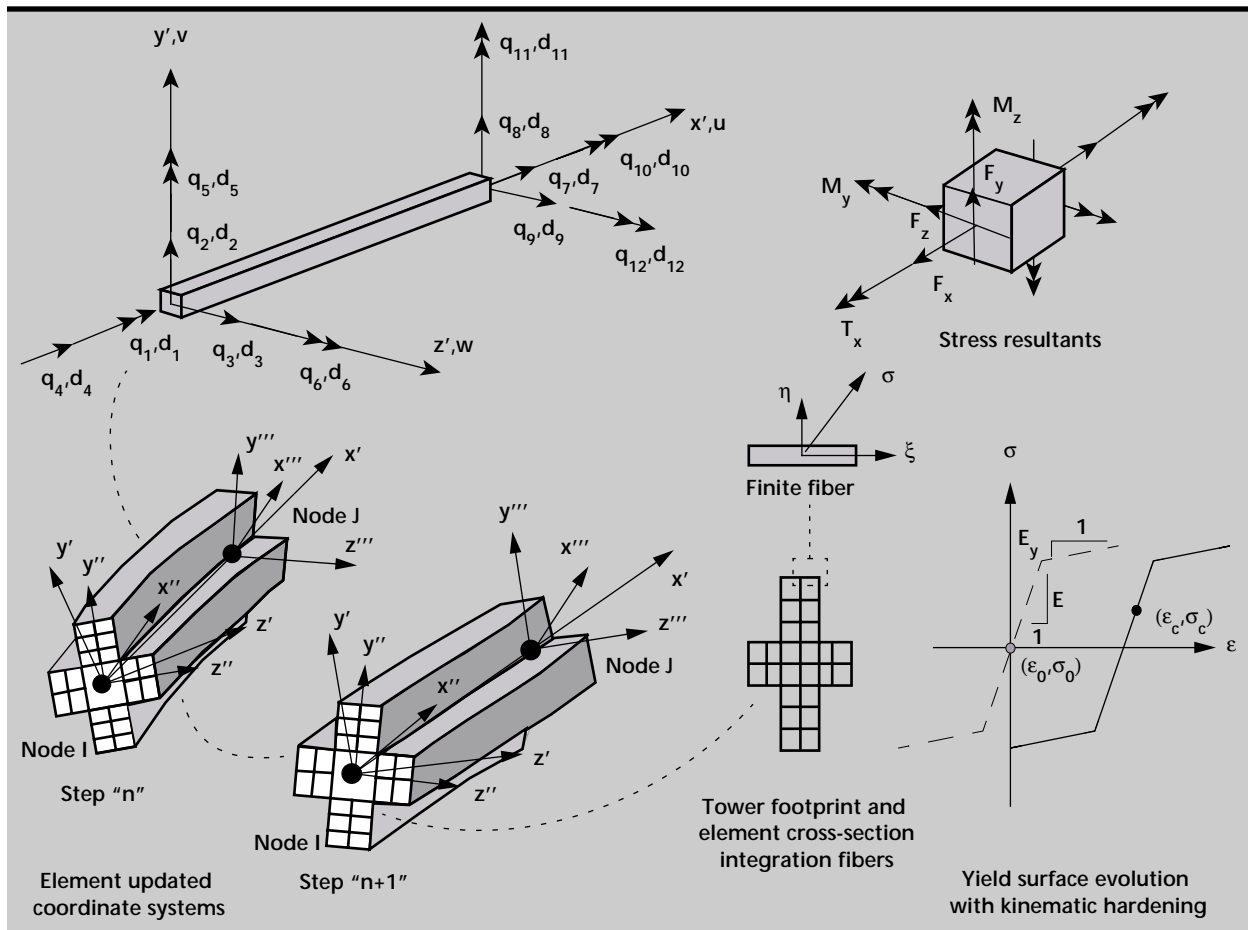

Figure 3. Finite rotation tower fiber flexure element.

Gross rigid-body rotations and translations are removed via the updated coordinate systems. However, to include the initial stress (geometric stiffness) contributions for the flexural element, which is required for initiating the bridge model, it is necessary to include all nonlinear terms in the strain-displacement relationships. To ensure efficiency of the element for linear as well as nonlinear problems, a cubic displacement field approximation is used for the transverse displacements of the flexural element.

Inelasticity in the flexure element is accounted for by division of the cross-section into a number of fiber zones with uniaxial plasticity defining the normal stress-strain relationship for each fiber zone, as indicated in **Fig. 3**. The element stress resultants are determined by integration of the fiber zone stresses over the cross section of the flexural element. The evolution of the yield surface is monitored by tracking the center of the yield region, and a stress update algorithm was implemented to allow accurate integration of the stress-stress constitutive law for large strain increments, including full load reversals.

To ensure path independence of the solution, the implementation of the plasticity model for the implicit Newton-Raphson equilibrium iterations uses a path-independent procedure whereby the element stresses are always updated from the last fully converged equilibrium state. The transformation between element local and global coordinates is accomplished through a vector transformation of element forces and displacements in which the transformation matrix consists of the direction cosines of the current updated element coordinate system. The flexural element matrices in natural coordinates are given by,[17]

$$\{Q_{Flexure}\} = [T]^T \int_{-1}^{1} [B]^T \{F\} J d\xi \qquad (14)$$

$$[K_{Flexure}] = [T]^T \quad \times$$

$$\left(\int_{-1}^{1} [B]^T \left[\frac{\partial F}{\partial \varepsilon} \right] [B] J d\xi + \int_{-1}^{1} \left[\left[\frac{\partial}{\partial d_k} B_G(\{d\}) \right]^T \{F\} \right]_{k=1,12} J d\xi \right) [T] \quad (15)$$

where [T] is the transformation matrix of direction cosines for the x′, y′, and z′ coordinate system, [B] is the linear strain-displacement matrix, $[B_G(\{d\})]$ is the displacement-dependent strain-displacement matrix resulting from the nonlinear strain terms, {F} is the element stress resultants, and $\left[\frac{\partial F}{\partial \varepsilon} \right]$ is the element constitutive matrix.

The second term of **Eq. 15** represents the initial stress contribution to the element stiffness, and with appropriate mathematical manipulation,[17] this matrix can be written as a function of the current axial force in the member.

For earthquake simulations, the element stiffness is only necessary for the implicit iterations required for the model gravity initiation. After gravity initiation, the element internal resisting forces are computed from **Eq. 14** for the explicit integration of the equations of motion.

The fiber element representation of the cellular Bay Bridge tower structure was assessed by comparison with detailed shell-element-based models of the Bay Bridge towers. For this comparison, a detailed shell- and beam-element model was constructed for the general purpose finite-element program NIKE3D,[19] and a reduced-order fiber model was constructed for a selected bridge tower, as shown in **Fig. 4**.

The detailed model used shell and beam elements to represent the massive laced members which constitute the tower diagonals and struts. The shell model completely discretized the internal cellular structure of the tower and included the transverse stiffening diaphragms. The fiber model uses one fiber zone for each cell segment in the tower, for example, the element uses 62 zones at the base of the tower, as shown in **Fig. 4**. The reduced-order tower model contains 126 active global degrees of freedom.

The first six natural modeshapes of the tower, as computed with detailed and reduced-order models, are shown in **Fig. 4**. The tower frequencies observed by Carder in 1936 are also shown in **Fig. 4**. Carder performed vibrational measurements of the Bay Bridge towers when the tower construction was completed prior to spinning of the main cables, thus experimental frequencies were obtained for all four of the stand-alone towers of the bridge. Carder identified the first longitudinal and first transverse mode for each tower.

The reduced-order model provides good estimates of the tower dynamics, and in light of the potential errors in the measured response, there is also good agreement between both of the numerical models and the experimental data of Carder. The mode-shapes shown in **Fig. 4** exhibit excellent agreement and the modal periods also exhibit good correlation.

Reduced-Order Deck Model. A truss bridge deck system can demand an enormous number of elements with brute force modeling based on shell and beam elements; an effective reduced-order model can dramatically reduce computational effort. The representation of a 3-D discrete lattice truss structure by an equivalent continuum has seen wide use in the development of reduced-order models.[3,20,21] For certain bridge deck configurations, beam-like continua models can adequately characterize the stiffening truss system in the mid-deck region of the structure.
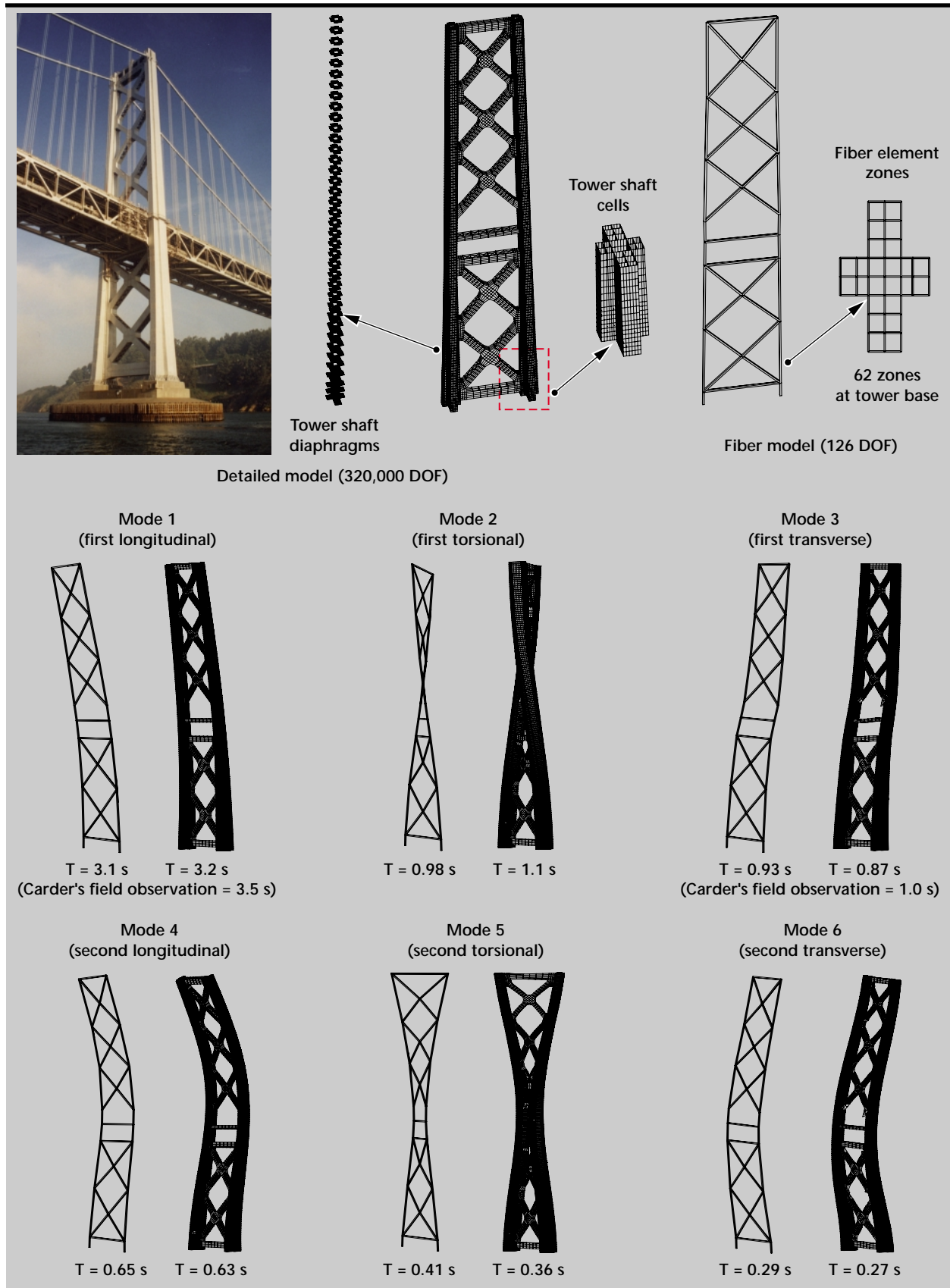
Figure 4. Detailed shell- and beam-element and reduced-order fiber bending element tower models and computed modeshapes (experimental values shown parenthetically).

However, the ability of continuum-based models to capture the effects of complex articulations at the ends of the stiffening trusses is highly suspect, especially where individual member forces can vary significantly depending on the specific connectivity between the truss joints and the towers and abutments. Accurate continuum representations also become problematic when the bridge deck system lacks transverse sway bracing, and the deck is subjected to severe warping deformation. Complex warping deformations defy attempts to represent the deformations with simple beam-like kinematics. Because of the limitations of continuum-based representations, a more detailed discrete model for bridge deck systems was developed. The resulting model represents a compromise between a highly efficient but questionably accurate continuum model of the deck system and a prohibitively expensive, highly detailed, brute force discrete shell- and beam-element model of the deck system.

The configuration and connection details in the two-level deck system of the Bay Bridge made appropriate reduced-order model construction particularly challenging. Lacking any transverse sway bracing between the upper and lower decks (**Fig. 5**), forces generated between the upper and

lower part of this structure must be transferred through bending of the stiffening truss elements in an inter-deck sway deformation. In the longitudinal direction, the deck slab-to-stiffening truss connection occurs through weak axis bending of the deck beams (**Fig. 6**), providing an extremely flexible connection between the deck slabs and the stiffening trusses. The deck slab systems, consisting of the concrete slab, deck beams, and stringers, are consequently weakly coupled to the deck stiffening truss in the longitudinal direction of the bridge, and the full membrane stiffnesses of the deck slabs are not activated by deformation of the stiffening trusses in the vertical plane. The complex kinematic characteristics associated with deck cross-section warping of this particular deck system do not readily lend this system to accurate characterization with beam-like continua.

The reduced-order model is based on special discrete elements for the deck system components. The deck model constituents consist of simple truss elements for the stiffening truss members, an orthotropic plane stress element for the deck slab and girder system, and a sway-stiffness element to account for the transverse bending of the lateral frames composed of the deck beams and stiffening truss vertical posts, as shown in **Fig. 5**. The active
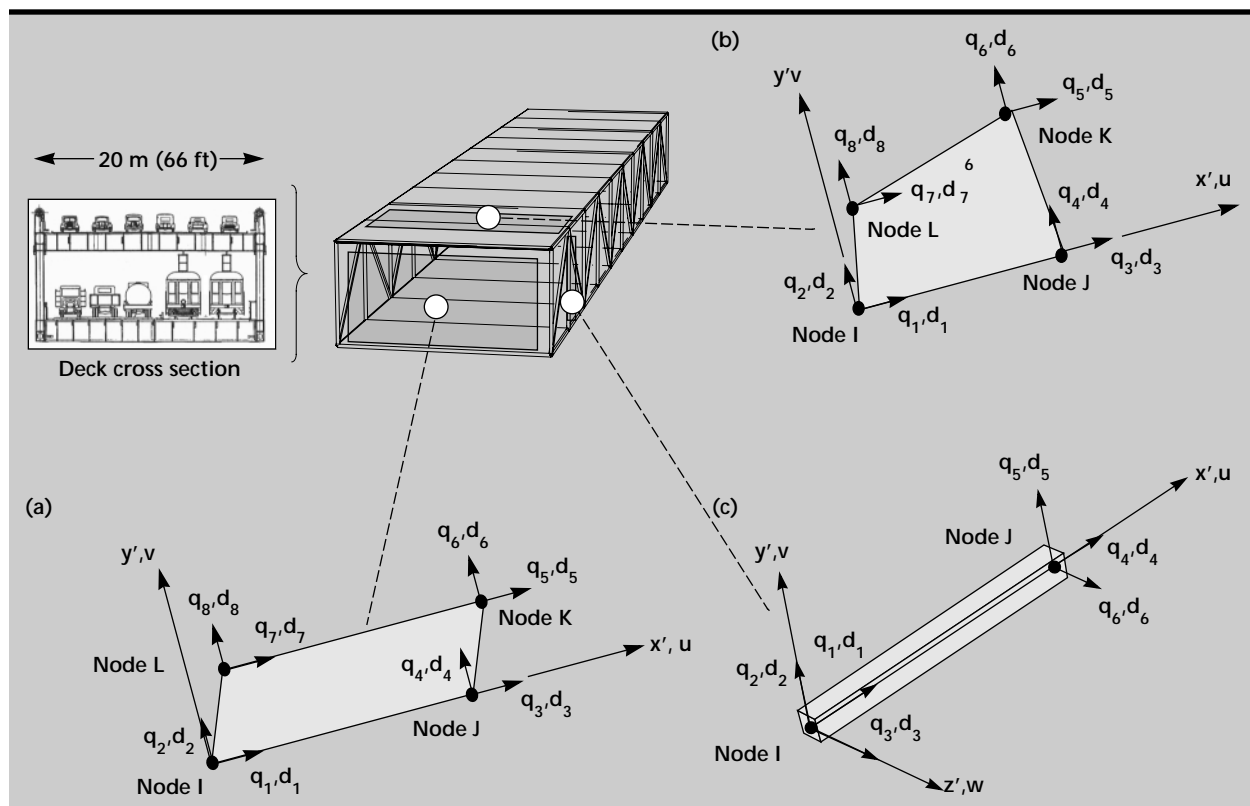

Figure 5. Reduced-order model of the deck system. (a) Sway stiffness element; (b) slab membrane; (c) stiffening truss element. All elements are shown in local element updated Lagrangian coordinate systems.

global degrees of freedom consist of three translations at each joint of the deck system. The sway-stiffness element was implemented to eliminate the need for any rotational degrees of freedom in the deck model. The capability of the deck system model to accommodate geometric nonlinearities associated with arbitrarily large displacements was included in the model to accurately capture the effects of potential large displacements occurring in a long bridge during earthquake ground motions.

Depending on the bridge system and the method by which the model is initialized to achieve the appropriate gravity configuration, gross model geometry changes and large model displacements can also occur during gravity initialization of the bridge model; and inclusion of geometric nonlinearities is necessary for the model initialization process.

The deck truss element shares common features with the flexural fiber tower model element in terms of the methodology for including geometric nonlinearities, displacement tracking, and material inelasticity. Similar to the tower flexure element, the member motions are tracked with a local element updated Lagrangian coordinate system which translates and rotates through space with the element. For the static initialization sequence, it is necessary to include the geometric component of element stiffness for some of the truss elements to create a nonsingular initial global stiffness matrix which allows equilibrium iterations to initiate. To include the initial geometric stiffness, the user must provide as input an initial axial tension in selected members of the deck stiffening truss system. For
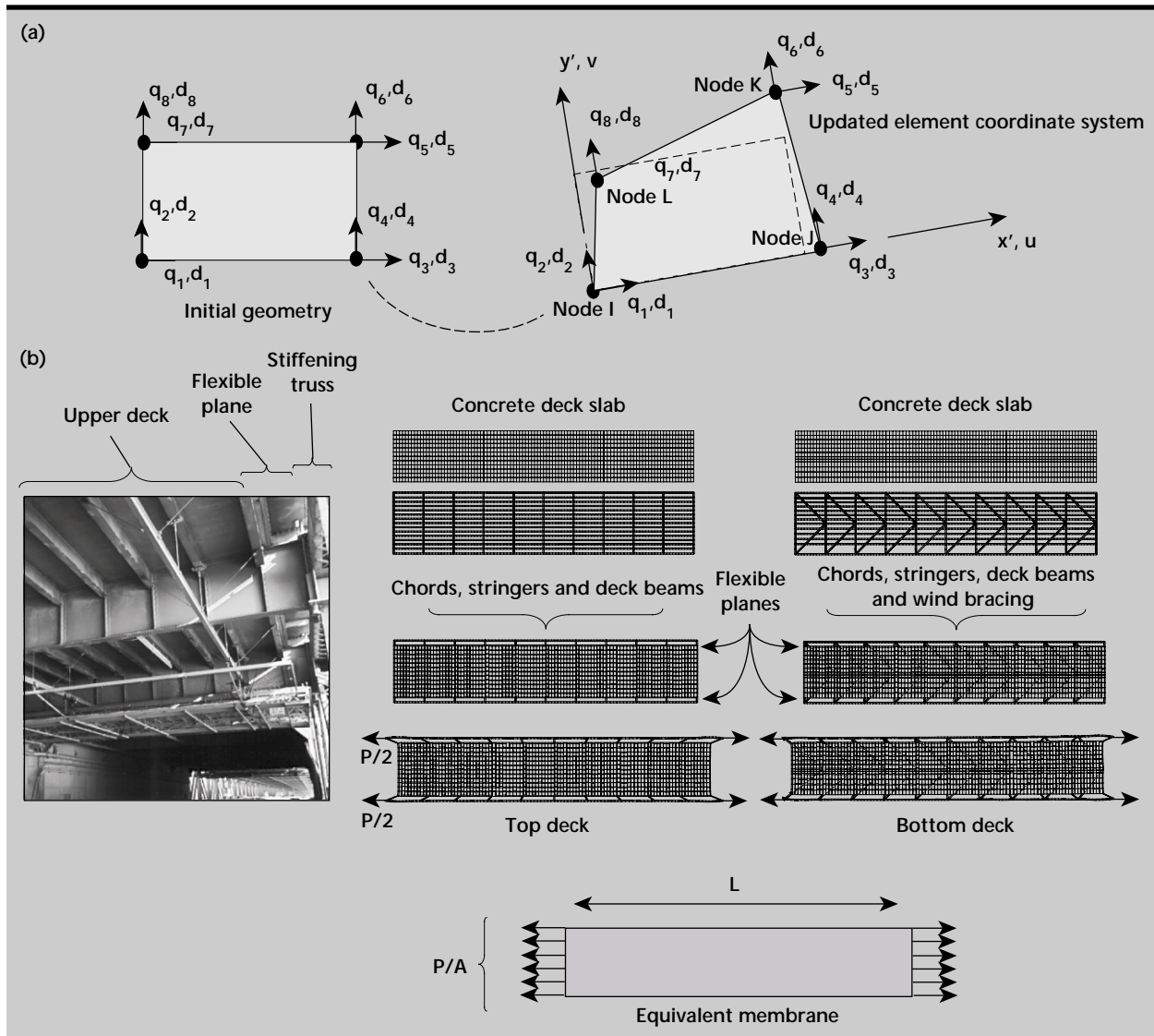

Figure 6. Deck membrane element. (a) Element degrees of freedom and updated Lagrangian coordinate system; (b) upper and lower deck in-plane models and equivalent membrane.

the Bay Bridge configuration, for example, an initial tension must be input for all of the vertical posts of the deck trusses.

For some vintage truss members, such as steel laced members, recent research[22] indicated the inelastic behavior can be controlled by inelastic buckling of the member or buckling of the plate connections at the end of the members, and can be quite complex. For these members, a simple elasto-plastic model is not an accurate representation of the complex inelastic buckling behavior. However, idealized elasto-plastic representation can be appropriate for modern bridge members where elements consist of rolled sections, and connections are based on sound inelastic design methods. The incorporation of complex inelastic buckling of vintage laced members and their connections will be addressed in future SUSPNDRS developments.

The deck membrane element, which represents the deck slab, beams, stringers, and any existing in-plane sway bracing, consists of a four-node, isoparametric, orthotropic plane stress element. The potentially large rigid-body displacements of the element are accounted for with an updated coordinate system which tracks with the element through space, as indicated in **Fig. 6**. The element matrices are based on a classical four node isoparametric formulation.

Selection of appropriate membrane properties was a nontrivial problem in the development of the reduced-order deck model for the Bay Bridge deck system. Because of the flexible connection between the deck system and the stiffening trusses (**Fig. 6**), there is weak longitudinal coupling between the deck slab system and the stiffening truss. This significantly reduces the composite action of the deck slabs and stiffening trusses. The deck membrane element requires elastic constants which will characterize the stress-strain behavior of the deck system.

Because of the complex coupling in the Bay Bridge deck system, the effective membrane properties cannot be easily obtained analytically from consideration of first principles. Because of the complex deformations, the equivalent membrane elastic properties were determined numerically by selective loading of detailed models of deck segments (**Fig. 6**). The detailed deck models shown in **Fig. 6** were constructed to include the weak connection between the deck system and the stiffening truss chords. The effective membrane properties are obtained from the detailed model analysis. For example, the longitudinal membrane effective elastic modulus is given by,

$$E_{Effective} = \frac{\dfrac{PL}{\Delta_1} - 2(EA_{Chords})}{A_{membrane}} \quad (16)$$

where Δ_1 is the stretch of the deck system for an applied load of P. After determining the appropriate elastic constants, the membrane element contribution to the element internal resisting forces and instantaneous stiffness are given by,[17]

$$\{Q_{Membrane}\} = \left[\int_{-1}^{1} \int_{-1}^{1} [B]^T [E][B]tDetJd\xi d\eta \right]\{d\} \quad (17)$$

$$[K_{Membrane}] = \int_{-1}^{1} \int_{-1}^{1} [B]^T [E][B]tDetJd\xi d\eta \quad (18)$$

where [E] contains the effective material constants obtained from the detailed deck segment models. Classical four-point Gaussian quadrature integration is used for the natural coordinate integration of the matrices.

The sway-stiffness element accounts for the lateral sway deformation between the upper and lower decks which results from flexure of the frame consisting of the deck beams and stiffening truss vertical posts. In the deck model the sway stiffness element is an 8×8 stiffness matrix which relates nodal forces to a measure of the lateral sway deformation of the frame. The sway and truss elements are shown in **Fig. 7**. The sway deformation between the decks is approximated by the summation of angles γ_1 and γ_2,

$$\gamma_{sway} = \gamma_1 + \gamma_2 \quad (19)$$

where,

$$\gamma_1 = \left(\left(\frac{d_4 + d_6}{2} \right) - \left(\frac{d_8 + d_2}{2} \right) \right)/W \quad (20)$$

$$\gamma_2 = \left(\left(\frac{d_5 + d_7}{2} \right) - \left(\frac{d_3 + d_1}{2} \right) \right)/H. \quad (21)$$

The nodal forces associated with sway deformation can be obtained either analytically or numerically by analysis of the cross-section frame with the loading and boundary conditions shown in **Fig. 7**.

For elastic behavior of the frame, the nodal forces associated with sway are given by,

$$\begin{bmatrix} F_H \\ F_V \end{bmatrix} = \begin{bmatrix} k_h \\ k_v \end{bmatrix} \gamma_{sway} \ . \tag{22}$$

Combining **Eq. 19** through **Eq. 22**, and using overall equilibrium relationships between the nodal forces in **Fig. 7**, the sway element stiffness matrix is given by,

$$\begin{bmatrix} q_1 \\ q_2 \\ q_3 \\ q_4 \\ q_5 \\ q_6 \\ q_7 \\ q_8 \end{bmatrix} = \frac{k_h}{2D} \begin{bmatrix} 1 & \eta & 1 & -\eta & -1 & -\eta & -1 & \eta \\ \eta & \eta^2 & \eta & -\eta^2 & -\eta & -\eta^2 & -\eta & \eta^2 \\ 1 & \eta & 1 & -\eta & -1 & -\eta & -1 & \eta \\ -\eta & -\eta^2 & -\eta & \eta^2 & \eta & \eta^2 & \eta & -\eta^2 \\ -1 & -\eta & -1 & \eta & 1 & \eta & 1 & -\eta \\ -\eta & -\eta^2 & -\eta & \eta^2 & \eta & \eta^2 & \eta & -\eta^2 \\ -1 & -\eta & -1 & \eta & 1 & \eta & 1 & -\eta \\ \eta & \eta^2 & \eta & -\eta^2 & -\eta & -\eta^2 & -\eta & \eta^2 \end{bmatrix} \begin{bmatrix} d_1 \\ d_2 \\ d_3 \\ d_4 \\ d_5 \\ d_6 \\ d_7 \\ d_8 \end{bmatrix} \tag{23}$$

or,

$$\{q\} = [k_s]\{d\} \tag{24}$$

where $\eta = \dfrac{H}{W}$. **Equation 23** provides the sway element nodal forces in terms of the nodal displacement quantities. The element matrices in global coordinates are provided by the transformation between the element instantaneous updated Lagrangian system and the global system coordinates,

$$\left[Q_{sway} \right] = [T(\{d\})]^T [k_s]\{d\} \tag{25}$$

$$\left[T_{sway} \right] = [T(\{d\})]^T [k_s][T(\{d\})] \ . \tag{26}$$

To evaluate the adequacy of the deck model, a number of comparisons were made between the reduced-order deck model and a detailed beam- and shell-element model of the Bay Bridge deck system. The first five natural modes of a simply-supported twenty-bay segment of the Bay Bridge deck, as computed from detailed and reduced-order models, are shown in **Fig. 8**. The mode shapes computed with the two models exhibit excellent correlation, and the frequencies are within approximately 10% for all of the first five modes. The simulations of the deck segment verified the reduced-order deck model can adequately capture the deck deformational modes, and the reduced-order model only necessitates a one-element discretization across the width of the deck.

This simple example provides a challenging problem for the reduced-order model because the discrete boundary conditions applied at the base of the deck segment result in modes which exhibit severe racking and warping of the deck (see mode 5, for example). In a deck with distributed support, such as the suspended deck of the bridge, the important deck modes will be of significantly longer wavelengths, and the effect of the discrete boundary
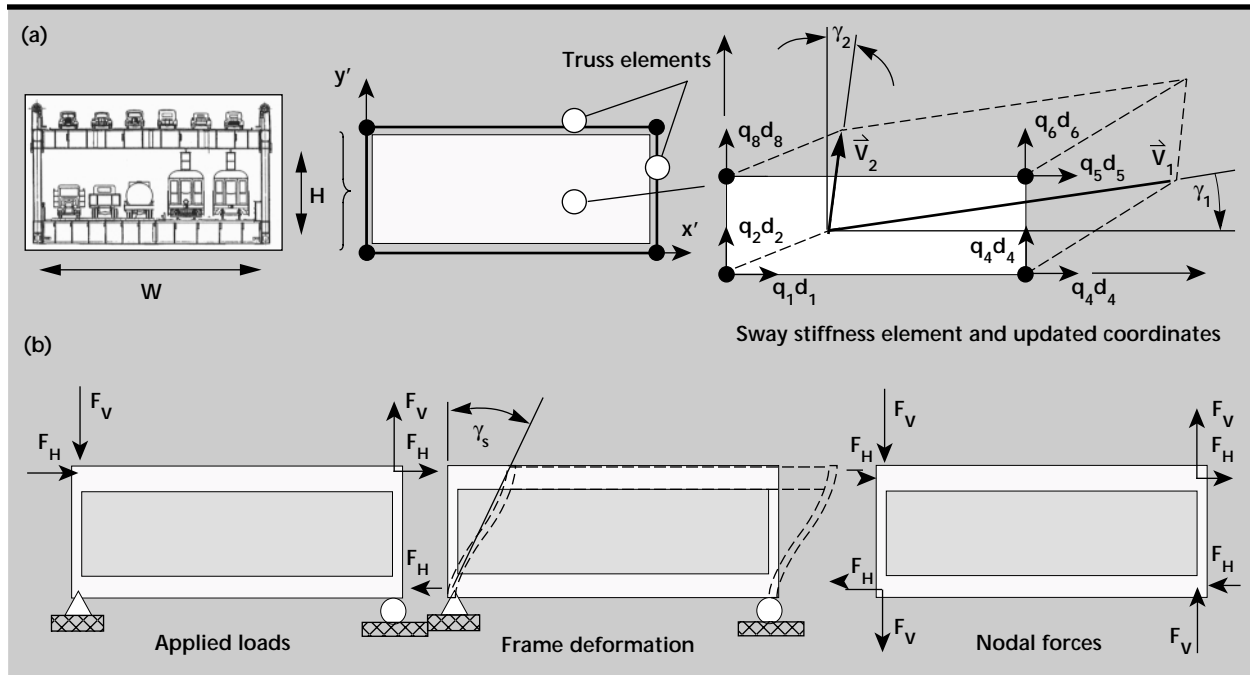

Figure 7. Sway stiffness element providing lateral sway resistance. (a) Sway and truss elements; (b) determination of sway element nodal forces for a sway displacement.

conditions will be more localized rather than propagating throughout the entire deck system, as is the case with the twenty-bay segment.

Bridge Cable Model. The bridge cables are modeled with a simple tension-only two-force member. The cable element is essentially identical to the deck truss element with the exception that the element coding does not permit compression to develop in any of the cable elements. If the cable element attempts to compress, the element stiffness and residual contributions are neglected in the implicit solution and the element forces are neglected in the explicit solution. An initial stress contribution to the element instantaneous stiffness is included to render the initial global tangent stiffness matrix of the bridge system nonsingular during gravity initialization. All of the bridge cable elements require an initial estimate of the cable tension as user input; a gross estimate of cable tension proved to be adequate to initialize the implicit static solution.

The procedure developed to define the initial geometry of the cables is based on constraining the cables by the initial unstretched cable length and allowing the Newton-Raphson equilibrium iterations to determine the natural sag geometry and tension of the cables. With the initial unstretched cable length of each cable serving as the constraint for the cable system model, the initial definition of the cable geometry in the finite-element model can be quite arbitrary and only affects the number of equilibrium iterations required to achieve the natural sag.

A SUSPNDRS program simulation of a simple sagging cable based on this approach is illustrated in **Fig. 9**. The initial geometry in the finite element model is crudely represented with two prescribed initially linear segments of cable elements, the total length of which exactly equals the total unstretched length of the actual cable. A uniform initial tension guess is applied as user input to each cable element for initialization of the initial stress contribution, and once gravity is applied, full Newton-Raphson equilibrium iterations achieve the appropriate cable geometry rapidly within five equilibrium iterations. The individual cable elements displace through large rigid-body displacements, and the overall geometry rapidly progresses to the appropriate hanging cable geometry. The numerical simulation results precisely match experimental data for the hanging cable obtained by Irvine and Sinclair.[23] Application of a point load was also considered after gravity initialization, and the simulation model accurately computed the deformed shape under gravity plus point loading, as shown in **Fig. 9**.

In the case of the Bay Bridge, the design and construction objectives included achieving a stress state in which the chords and diagonals of the stiffening truss were essentially stress free under full gravity dead load. The vertical posts of the truss
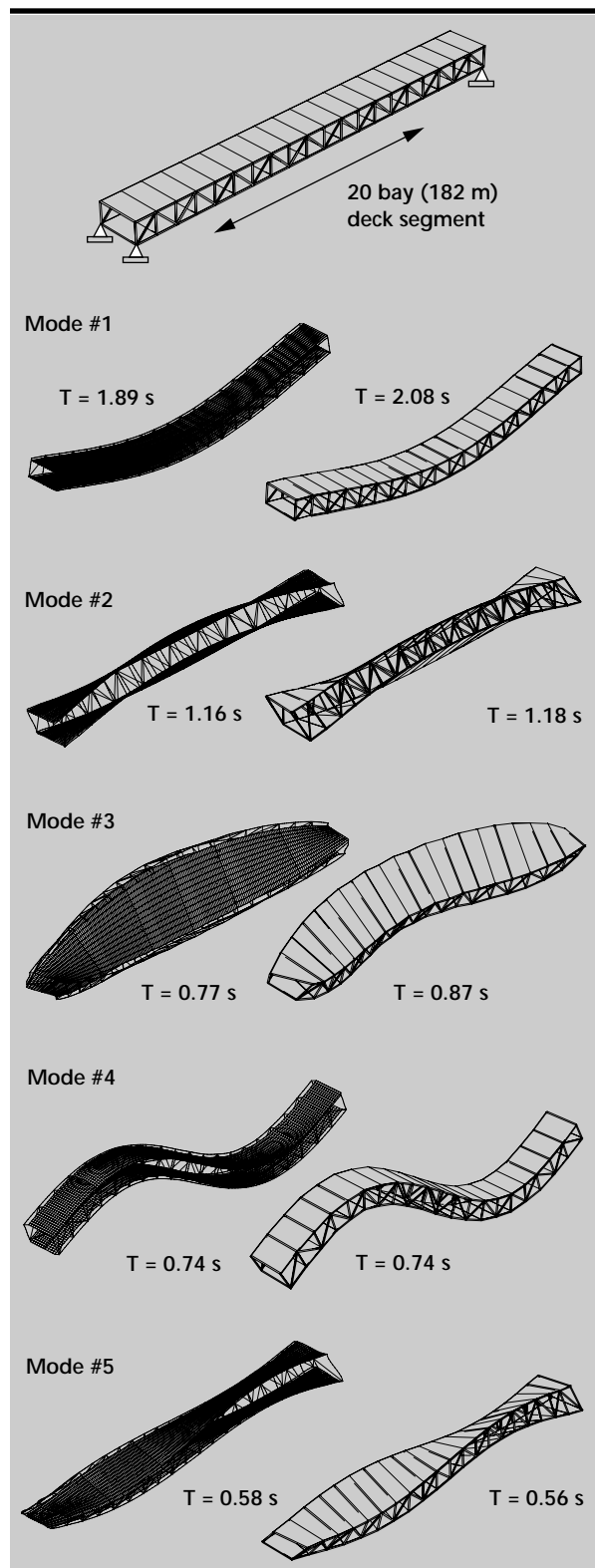

Figure 8. Natural modeshapes of a twenty-bay deck segment from detailed and reduced-order models.

were thus assumed to be the only gravity stressed members in the deck truss. This condition was obtained in field construction by allowing the truss joints to remain loosely tied together with construction pins until the deck was entirely supported from the vertical suspenders, with final riveting of the joints after the entire deck was suspended.

As a result of this construction sequence, the deck stiffening truss did not resist the bridge's gravity load as a composite structure. This design objective is common for many lattice deck suspension bridges. On the Bay Bridge, hydraulic jacking was also used between the main cables and the cable saddles atop the towers prior to application of the deck system to ensure the towers would be straight, vertical, and free of large shear forces at the completion of the construction sequence.

The computational procedure for model initialization must emulate this construction sequence. To initialize the bridge model to the appropriate gravity configuration, an automated procedure was developed. The procedure (**Fig. 10**) first analyzes the main cables and towers under full bridge dead load to determine the final main cable elevations under full gravity load (**Fig. 10b-c**).

In practice, the arbitrary geometry shown in **Fig. 10** is not used. Because of the availability of powerful mesh generators, once the initial unstretched cable lengths are determined, a subroutine mesh generator produces an initial bridge model based on a parabolic approximation of the main cable geometry. For most bridges, the parabolic approximation provides a geometry close to the correct shape. Use of a parabolic geometry is only used for computational expediency; any initial geometry could actually be used, the only computational difference being the computational effort required to achieve the final geometry. The achievement of the final bridge configuration, starting with two entirely different initial geometries, is shown in **Fig. 11**. The only difference between the
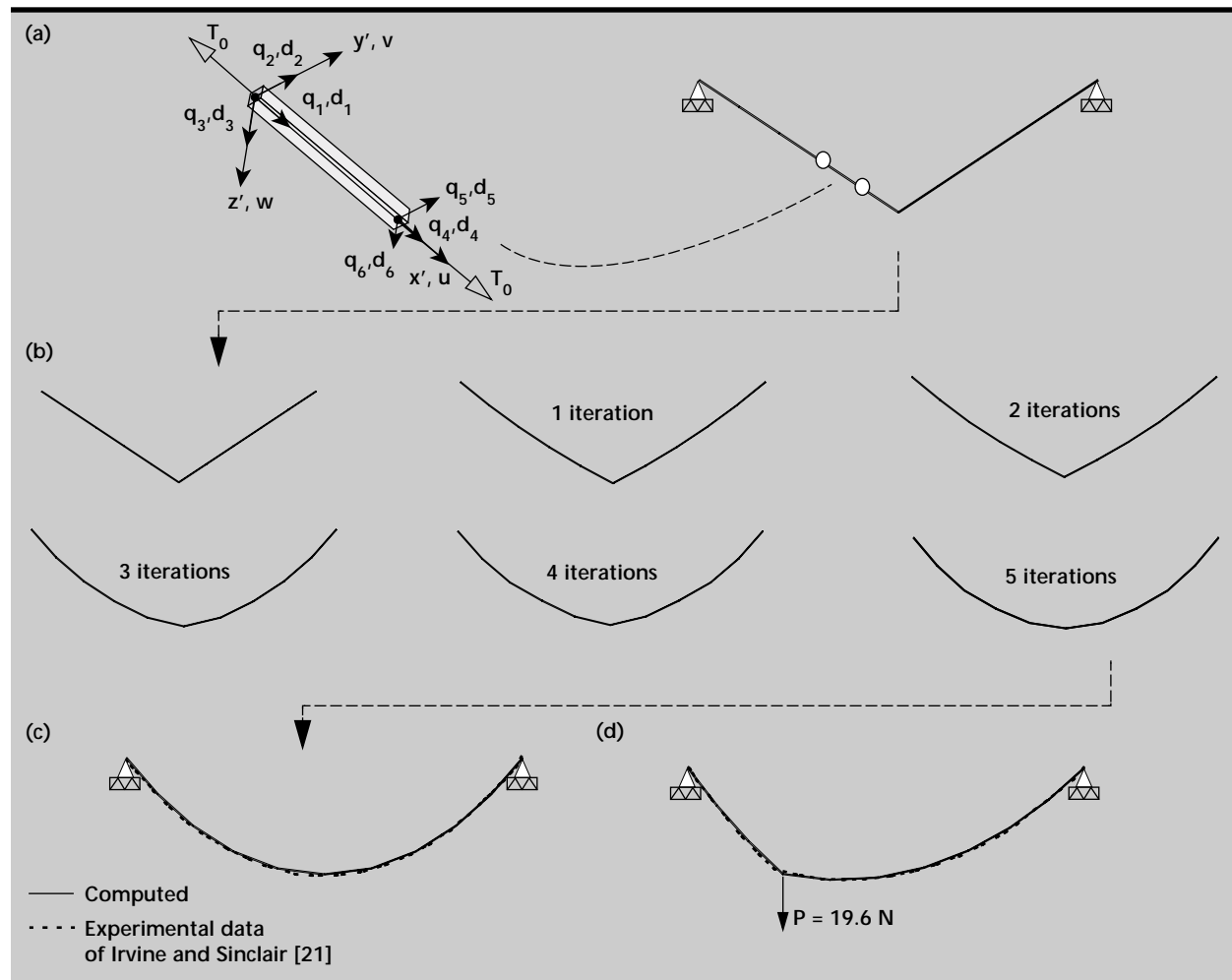

Figure 9. Analysis of a hanging cable. (a) Ten-element cable model with initial tension and constrained length; (b) deformed shape at each equilibrium iteration; (c) computed and observed cable geometry under gravity load; (d) computed and observed cable geometry under gravity and point load.

models is the required number of equilibrium iterations to achieve the final gravity-loaded model.

The parabolic shape is computed such that the main cables have the appropriate length, and the initial locations of the deck nodes are determined by dropping to an elevation corresponding to the unstretched length of the vertical suspenders. The chord and diagonal elements of the truss are inactivated for the gravity initialization, therefore the deck truss will not contribute stiffness to the model during gravity initialization. In addition, the main cables are allowed to slip horizontally relative to the tops of the towers, in order that the towers will be straight and subjected to pure axial load at the end of gravity initialization.
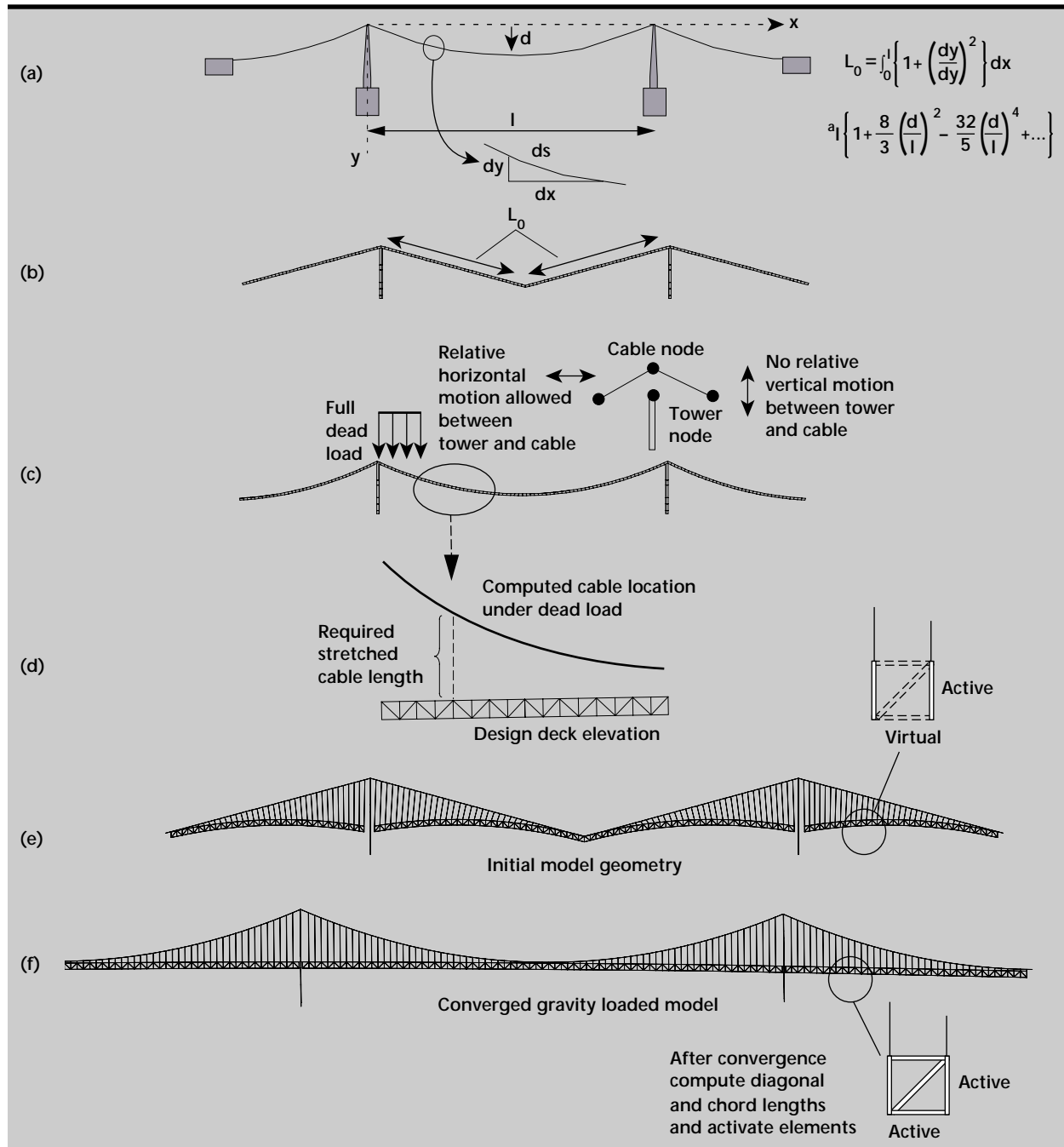
Figure 10. Development of a model with appropriate gravity shape and forces. (a) Estimate unstretched length of main cables based on bridge design and cable field survey data; (b) generate simple model geometry with appropriate unstretched lengths; (c) perform static load analysis of main cables with full dead load of deck system; (d) based on computed main cable geometry and design deck elevations, determine stretched lengths of suspenders under gravity load; (e) generate a model with arbitrary geometry constrained by unstretched cable lengths; (f) perform implicit Newton-Raphson equilibrium iterations for gravity loads until convergence.

Once the gravity load equilibrium iterations are complete, precise new element lengths are computed internally by the SUSPNDRS program and stored for the chord and diagonal members, so that they will be exactly unstressed at the gravity load geometry when the dynamic analysis is initiated. The gravity deformed shape and tension stress fields obtained from the static analysis become the initial condition state for the transient earthquake computation. Once the appropriate gravity load configuration is achieved, the main cables, which were allowed to slip relative to the towers under gravity initialization to keep the towers vertical and absent of longitudinal shear loads, are slaved to the top of the towers to provide cable-to-tower connectivity for the transient response analysis.

The model developed for half of the Bay Bridge geometry, based on this procedure, is shown in **Fig. 11**. This model initialization procedure ensures that the bridge computational model will have the correct as-built bridge geometry.

Deck and Caisson Contact Models. Bridge deck systems typically contain a number of structural discontinuities at interior expansion joints and at abutments to accommodate thermal deformations. These discontinuities can have a pronounced influence on the dynamic response of the bridge system and can result in significant dynamic impact between disjoint bridge segments. Observational measurements of the earthquake response of bridges have indicated the occurrence of large accelerations and inter-segment forces as a result of impact of adjacent bridge segments.[24]

In addition to deck segment impact, during seismic motions, bridge foundations can potentially be subjected to rocking and uplift, with multiple occurrences of impact. For the Bay Bridge, the towers are placed on large caissons which rest on bedrock, the caissons are unanchored to the bedrock, and the potential exists for rocking and uplift of the caissons under strong ground motion. Foundation rocking can significantly affect the superstructure response to earthquake ground motions[21] and should be accounted for in an accurate numerical simulation.

To simulate deck impact and foundation rocking, a simple node-to-node contact element was developed for the SUSPNDRS program which allows two nodes to close within a specified stand-off distance before node-to-node contact occurs. The element also admits tensile forces to develop between the nodes as the nodes separate to allow representation of displacement-limiting structural details which can prohibit large separation of two bridge segments. For the Bay Bridge, the main suspended spans are connected to the towers and central anchorage caisson with a slip joint that couples the deck to the tower or caisson in the transverse direction, but allows limited longitudinal motion once static friction of the joint is overcome, as shown in **Fig. 12**. This construction detail can be compressive when the deck moves into the caisson or tensile when the deck pulls away from the caisson.

In the node-to-node contact element, the nodal force contributions are generated vectorially and translated into the global bridge geometry based on
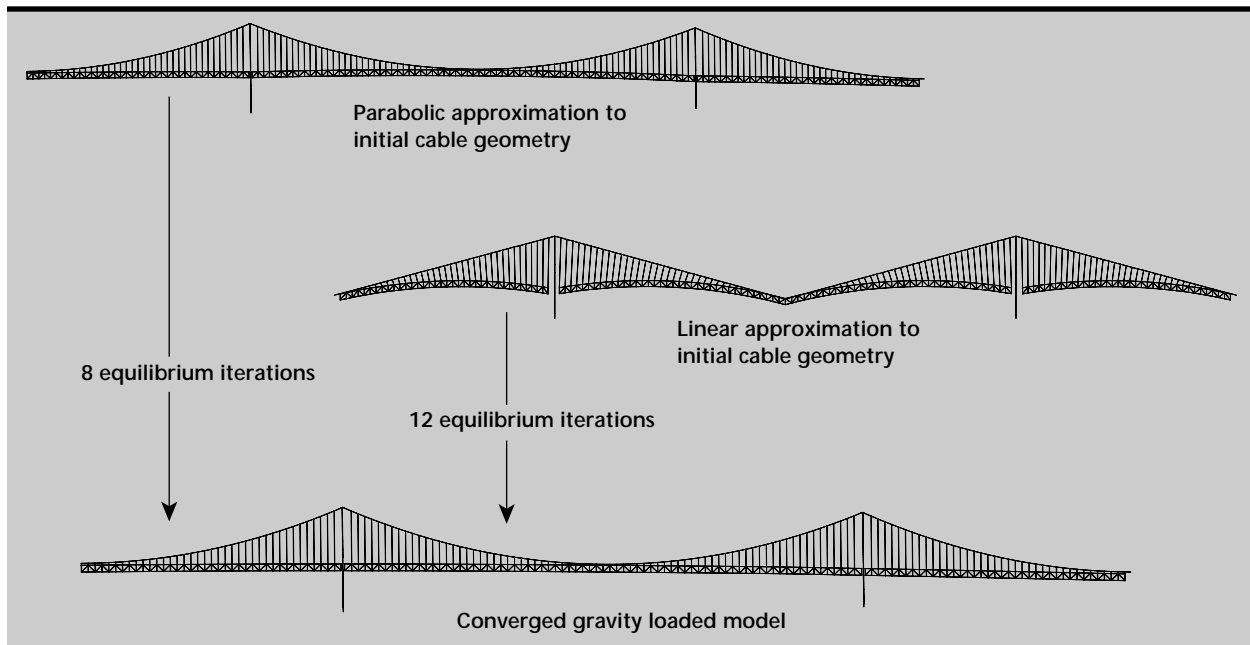

Figure 11. Gravity initialization of the model with different initial model geometries.

the current deformed shape of the bridge system. The contact forces are given by,

$$\begin{bmatrix} \Gamma_1 \\ \Gamma_2 \end{bmatrix} = K_C \left[\begin{bmatrix} 1 & -1 \\ -1 & 1 \end{bmatrix} \begin{bmatrix} d_1 \\ d_2 \end{bmatrix} + \begin{bmatrix} -1 \\ 1 \end{bmatrix} \delta_C \right] \left(\psi_C(d_2, d_1, \delta_C) \right) + K_T \times$$

$$\left[\begin{bmatrix} 1 & -1 \\ -1 & 1 \end{bmatrix} \begin{bmatrix} d_1 \\ d_2 \end{bmatrix} + \begin{bmatrix} 1 \\ -1 \end{bmatrix} \delta_T \right] \left(\psi_T(d_2, d_1, \delta_T) \right) \quad (27)$$

where,

$\psi_C(d_2, d_1, \delta_C) \equiv 1.0$ when $((d_1 - d_2) - \delta_C) > 0$ and $\psi_C(d_2, d_1, \delta_C) \equiv 0$ when $((d_1 - d_2) - \delta_C) \leq 0$, $\psi_T(d_2, d_1, \delta_T) \equiv 1.0$ when $((d_2 - d_1) - \delta_T) > 0$ and $\psi_T(d_2, d_1, \delta_T) \equiv 0$ when $((d_2 - d_1) - \delta_T) \leq 0$.

The nodal contact forces are assumed directed collinear along the line defined by the two contact nodes (Node I and Node J in **Fig. 12**) and can be transformed to global coordinates based on the direction cosines of the line segment.

With explicit time integration, the numerical values of the effective contact stiffnesses K_T and K_C must be selected in a way which does not result in a reduction of the Courant time step, or alternatively, the Courant time step must be decreased to reflect the added stiffness to the system when contact occurs. Numerical experimentation has indicated that if the contact stiffnesses are selected such that they are of the same order as the stiffness of the structural elements which couple to the point of contact, the interface stiffness will not adversely affect the integration time step. Based on this, upper-bound limiting values for the interface stiffnesses have been used in the SUSPN-DRS contact elements.

Impact between bridge segments or foundation rocking with impact can result in sudden large nonlinearities in the bridge system model. Rigorous representation of impact phenomena presents a computationally difficult problem, and based on the authors' experience with implicit time-integration finite-element programs, the seismic analysis of bridges with multiple impacting segments can be quite difficult with many equilibrium iterations and potential converge failure for each severe impact event. At best, multiple impacts significantly detract from the efficiency of implicit time-integration schemes.
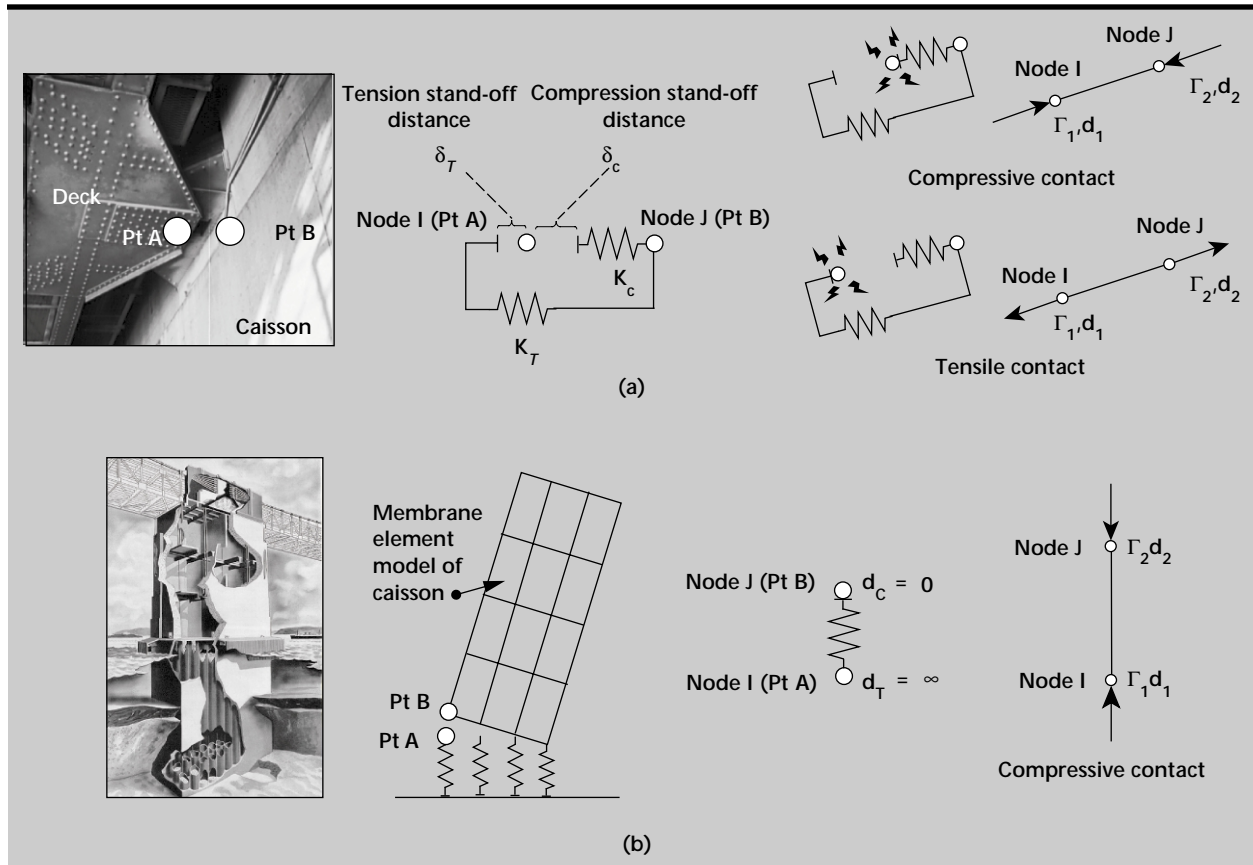

Figure 12. Nodal contact in the bridge model. (a) Contact at the deck-to-tower and deck-to-caisson connection; (b) contact at the base of a caisson.

Explicit time-integration, on the other hand, is particularly adept at accurately tracking impact events, with essentially no detriment to the algorithm efficiency when impact occurs. This was one of the primary motivators for including explicit integration in the SUSPNDRS program.
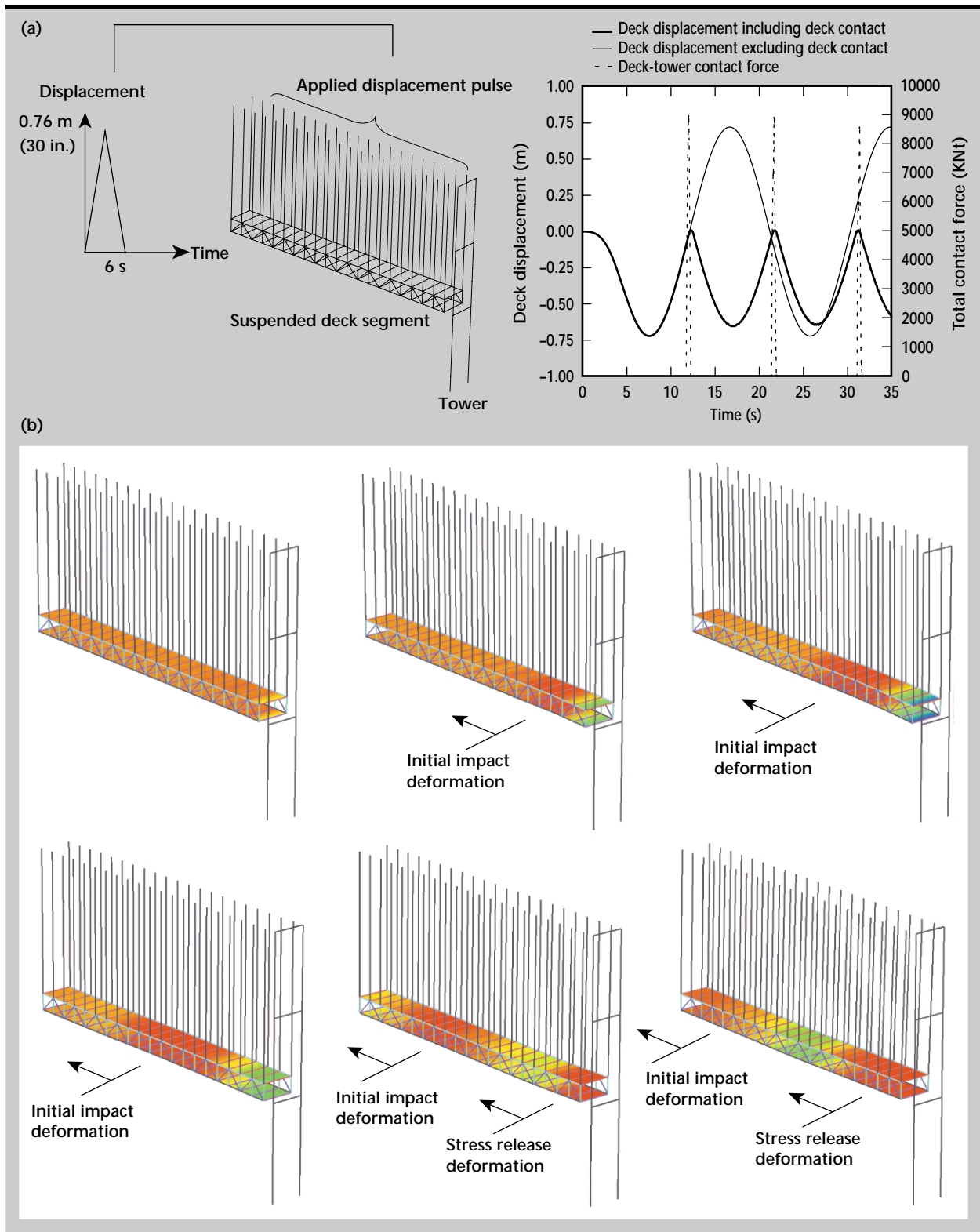

Figure 13. Impact of a deck segment with a tower. (a) Deck displacement and contact forces; (b) impact and relief stress wave propagating in the deck.

An example of computed deck-tower impact with the SUSPNDRS program is shown in **Fig. 13**. A twenty-segment length of bridge deck is given an initial applied displacement pulse by moving the top of the suspension cables with a prescribed 0.75-m displacement over 6 s. This support motion imparts an initial swinging motion into the deck segment. The deck segment is moved away from the tower, and as the segment swings back freely toward the tower, impact occurs between the deck segment and the tower. A stand-off distance is included in the contact element which represents the physical width of the tower at the location of the bridge deck, so the model will initiate impact at the correct physical location in space.

When the deck segment impacts the tower, large compressive forces are developed in the deck and stiffening truss elements, and a compressive wave propagates down the deck system. During the impact, the relatively flexible deck is in contact with the tower for a finite length of time, generating large contact forces, and when the deck swings back away from the tower, a propagating release wave is generated as the stresses in the deck slab and stiffening truss system are suddenly relieved. The simulation shown in **Fig. 13** was carried out through three successive impacts as the deck swung back and forth. The significance of the impact phenomenon on the deck dynamics can be seen by comparing the deck displacements for the cases in which impact is included and neglected, respectively (**Fig. 13a**). The impacts significantly change the displacements of the deck segment as the flexible deck system essentially bounces off of the stiff tower three times.

The simulation was performed for an undamped system, and the explicit integration algorithm accurately tracked the impacts and the impact-generated waves. Computer animations of the impact sequences indicated that the waves generated with each impact continued to travel back and forth across the deck without dissipation for as long as the simulation was continued.

The explicit time integration scheme implemented in the SUSPNDRS program has no difficulties tracking the sequence of impacts and modeling the wave propagation up and down the deck segment.

Global Model Dynamics and Transient Earthquake Response

Once the bridge model geometry is appropriately initialized under gravity loading, eigenvalue analyses can be performed to determine the natural mode-shapes and the transient response to earthquake ground motion can be computed. For one span of the San Francisco-Oakland Bay Bridge, selected computed natural modes are shown in **Fig. 14a**. The fundamental mode of the model consists of transverse motion of the main span and this concurs with the fundamental mode observation made by Carder in 1936. The computed modal period also agrees well with the observation of Carder.

The range of period values from the computed model reflect different assumptions of connectivity between the deck and tower with the lower period corresponding to an assumption of a locked expansion connection at the deck-tower interface and the higher value corresponding to a completely free connection.

A major objective of the research was to develop understanding of the response of long-span bridges to near-field ground motions. The companion paper discusses in some detail the relationship between the near-field ground motions and transient bridge response.[16]

As an example of the potential effects of near field motions, the response of the bridge segment to 80 s of earthquake ground motion is shown in **Fig. 14b**. The ground motions indicated included a large long-period displacement pulse and permanent ground displacement which result at the Bay Bridge site due to a M = 7 Hayward fault earthquake (see **Fig. 1**). The exaggerated bridge displacements indicate that when the large displacement pulse occurs, the flexible deck cannot react as fast as the stiff towers and lags behind, as the towers begin to return in the opposite direction, the deck has finally begun to respond and essentially flings through the towers in the opposite direction. This type of motion can impart tremendous energy into the bridge system right at the initiation of the earthquake motions, and is not unlike the near field phenomenon described for buildings by Hall *et al.*[25,26]

Conclusions

A new nonlinear computational tool has been developed for numerically simulating the earthquake response of suspension bridges. The resulting finite-element model incorporates geometric nonlinearities due to large displacements, potential contact and impact between disjoint bridge segments, rocking foundation uplift, and material nonlinearities due to steel plasticity.

The system solution algorithms use a combination implicit-explicit solution scheme to achieve appropriate nonlinear static initialization and nonlinear transient analysis of the bridge system. The model relies on reduced-order characterizations
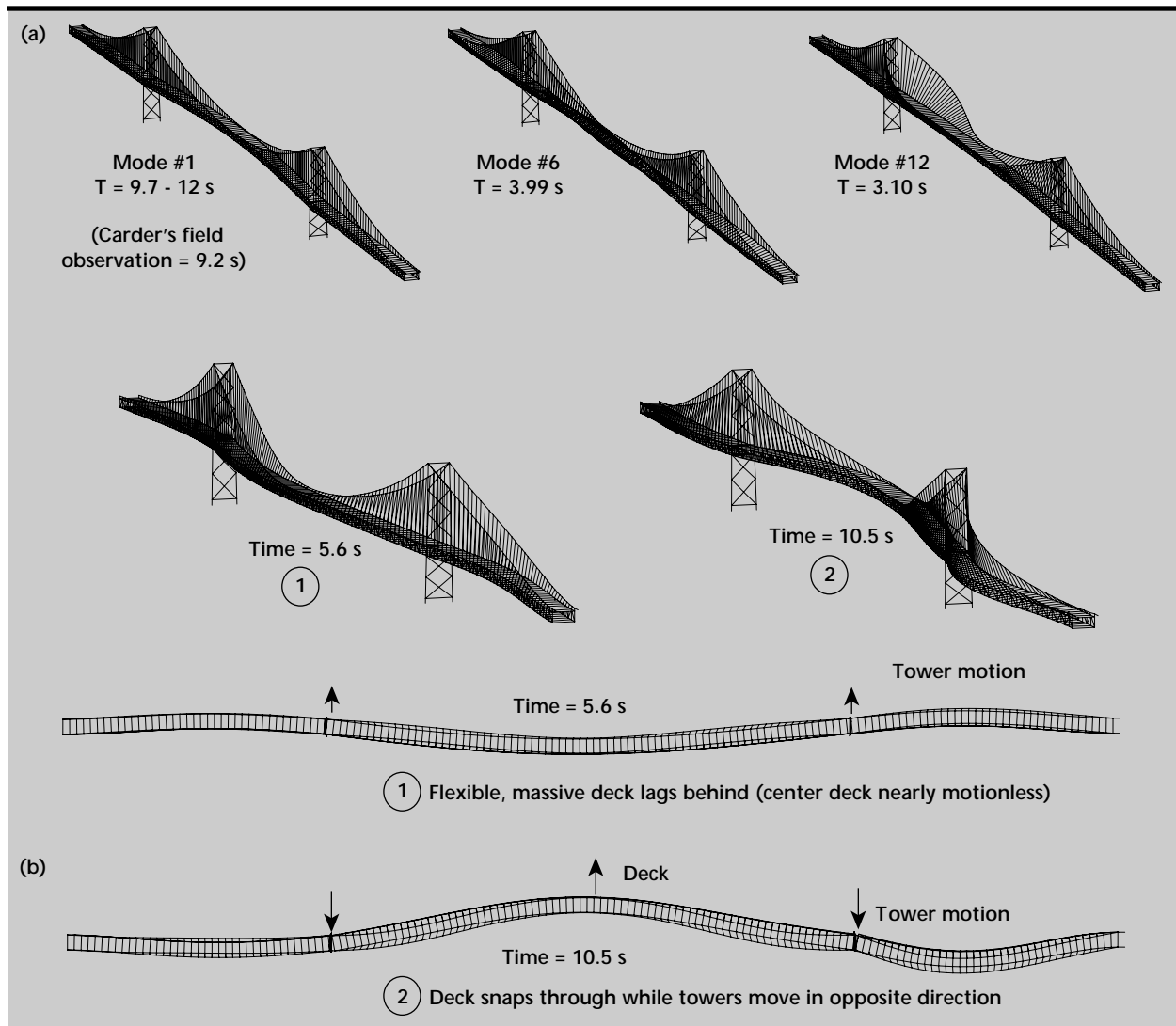
Figure 14. Global response of a Bay Bridge span. (a) Computed modeshapes (experimental values shown parenthetically); (b) transient response due to near-field motions.

of the bridge components to minimize the number of equations in the bridge system model and to ensure element physical dimensions will be large, thus maximizing the time step for the conditionally stable explicit solution algorithm.

The robust nature of the explicit time-integration scheme provides a numerical solution framework ideally suited to the transient analysis of a system with severe nonlinearities and to ultimate collapse simulations. This framework will readily accommodate and exploit new characterizations of complex individual member nonlinearities (such as laced members and structural joint nonlinearities and joint failures) as the information becomes available from experimental research.

Acknowledgments

References

1. A. M. Abdel-Ghaffar (1978), "Free lateral vibrations of suspension bridges," *J. of the Structural Division*, ASCE, Vol. **104**, No. 3, pp. 503–525.

2. A. M. Abdel-Ghaffar (1979), "Free torsional vibrations of suspension bridges," *J. of the Structural Division*, ASCE, Vol. **105**, No. 4, pp. 767–788.

3. A. M. Abdel-Ghaffar (1982), "Suspension bridge vibration: continuum formulation," *J. of Engineering Mechanics*, ASCE, Vol. **108**, No. 6, pp. 1215–1231.

4. A. A. Dumanoglu, J. M. W. Brownjohn, and R. T. Severn (1992), "Seismic analysis of the Fatih Sultan Mehmet (second Bosporus) Suspension Bridge," *Earthquake Engineering and Structural Dynamics*, Vol. **21**, pp. 881–906.

5. D. S. Carder (1937), "Observed vibrations of bridges," *Bulletin of the Seismological Society of America*, Vol. **29**, No. 4, pp. 267–303.

6. A. M. Abdel-Ghaffar and R. H. Scanlan (1985), "Ambient vibration studies of Golden Gate Bridge: suspended structure," *J. of Engineering Mechanics*, ASCE, Vol. **111**, No. 4, pp. 463–482.

7. A. M. Abdel-Ghaffar and R. H. Scanlan (1985), "Ambient vibration studies of Golden Gate Bridge: suspended structure," *J. of Engineering Mechanics*, ASCE, Vol. **111**, No. 4, pp. 483–499.

8. J. M. W. Brownjohn, A. A. Dumanoglu, and R. T. Severn (1992), "Ambient vibration survey of the Fatih Sultan Mehmet (second Bosporus) Suspension Bridge," *Earthquake Engineering and Structural Dynamics*, Vol. **21**, pp. 907–924.

9. V. R. McLamore, G. C. Hart, and I. R. Stubbs (1971), "Ambient vibration of two suspension bridges," *J. of the Structural Division*, ASCE, Vol. **97**, No. 10, pp. 2567–2582.

10. A. M. Abdel-Ghaffar and L. I. Rubin (1983), "Nonlinear free vibrations of suspension bridges: theory," *J. of Engineering Mechanics*, ASCE, Vol. **109**, No. 1, pp. 313–329.

11. A. M. Abdel-Ghaffar and L. I. Rubin (1983), "Nonlinear free vibrations of suspension bridge: application," *J. of Engineering Mechanics*, ASCE, Vol. **109**, No. 1, pp. 330–345.

12. A. S. Nazmy and A. M. Abdel-Ghaffar (1990), "Non-linear earthquake response of long-span cable-stayed bridges: theory," *Earthquake Engineering and Structural Dynamics*, Vol. **19**, pp. 45–62.

13. A. S. Nazmy and A. M. Abdel-Ghaffar (1990), "Non-linear earthquake response of long-span cable-stayed bridges: application," *Earthquake Engineering and Structural Dynamics*, Vol. **19**, pp. 63–76.

14. T. J. Ingham, S. Rodriguez, and M. Nader (1997), "Nonlinear analysis of the Vincent Thomas Bridge for seismic retrofit," *Computers and Structures*, Vol. **64**, No. 5/6, pp. 1221–1238.

15. S. C. Larsen and C. A. Schultz (1995), "ELAS3D: 2D/3D elastic finite difference wave propagation code," Lawrence Livermore National Laboratory, Livermore, California (UCRL-MA-121729).

16. D. B. McCallen, and A. Astaneh-Asl (1999), "A reduced order model for nonlinear suspension bridge analysis," *Computers and Structures*, (in review).

17. D. B. McCallen and A. Astaneh-Asl (1997), "SUSPNDRS: a numerical simulation tool for the nonlinear transient analysis of cable supported bridge structures, part I: theoretical development," Lawrence Livermore National Laboratory, Livermore, California (UCRL-ID-127626).

18. R. D. Cook, D. S. Malkus, and M. E. Plesha (1989), "Concepts and applications of finite elements," John Wiley & Sons.

19. B. N. Maker (1995), "NIKE3D - a nonlinear, implicit three-dimensional finite element code for solid and structural mechanics," Lawrence Livermore National Laboratory, Livermore, California (UCRL-MA-105268 Rev. 1).

20. D. B. McCallen and K. M. Romstad (1990), "A contin-uum model for lattice structures with geometric and material nonlinearities," *Computers and Structures*, Vol. **37**, No. 5, pp. 795–822.

21. D. B. McCallen and K. M. Romstad (1994), "Nonlinear model for building-soil systems," *J. of Engineering Mechanics*, ASCE, Vol. **120**, No. 5, pp. 1129–1152.

22. A. Astaneh-Asl, S. W. Cho, C. M. Bowen, and M. Blondet (1993), "Post-buckling ductility of critical members of the Golden Gate Bridge," University of California at Berkeley, Report UCB/CE-Steel-93/01.

23. H. M. Irvine and G. B. Sinclair (1976), "The suspended elas-tic cable under the action of concentrated vertical loads," *Int. J. of Solids and Structures*, Vol. **12**, pp. 309–317.

24. P. K. Malhotra, M. J. Huang, and A. F. Shakal, "Seismic interaction at separation joints of an instru-mented concrete bridge," *Earthquake Engineering and Structural Dynamics*, Vol. **24**, pp. 1055–1067.

25. J. F. Hall, T. H. Heaton, M. W. Halling and D. J. Wald (1995), "Near-source ground motion and its effects on flexible buildings," *EERI Earthquake Spectra*, Vol. **11**.

26. T. H. Heaton, J. F. Hall, D. J. Wald, and M. W. Halling (1995), "Response of high-rise and base-isolated buildings to a hypothetical M = 7.0 blind thrust earth-quake," *Science*, Vol. **267**.

Seismic Studies of the San Francisco-Oakland Bay Bridge

David B. McCallen
Center for Complex Distributed Systems

Shawn C. Larsen
Computer Systems and Applications
Computation Directorate

Abolhassan Astaneh-Asl
Department of Civil and Environmental Engineering
University of California at Berkeley
Berkeley, California

We have developed new methodologies and computational tools for simulating earthquake ground motions and the seismic response of cable-supported bridges. The simulation tools are described and an example application for an important long-span suspension bridge is demonstrated. The application portion of the study has particular focus on the potential damaging effects of long period displacement pulses and permanent ground displacements which can occur when a bridge is located in the near-field of a major earthquake fault.

Introduction

Realistic and accurate simulation of the seismic response of long-span bridges presents a significant technical challenge. The generation of broad-band, spatially varying ground motion is a difficult seismological and geotechnical problem, particularly for bridges located near a causative fault where long-period near-field effects may dominate the ground motion hazard for flexible structures. Accurate simulation of the transient dynamic response of large bridges also presents the structural engineer with a significant challenge. Nonlinear response simulations are computationally intensive for long-span bridges due to the size of the structural systems. If significant nonlinearities are prevalent in the structural system, such as geometric nonlinearities associated with large displacements, material nonlinearities due to members yielding or buckling or strong nonlinearities due to impact at expansion connections or rocking foundations, the computational requirements for general purpose finite-element codes may be prohibitive.

A multidisciplinary research and development project conducted by the University of California at Berkeley and the Lawrence Livermore National Laboratory is investigating both earthquake ground motion and structural response issues for long-span bridges. The research is developing a new massively parallel linear finite-difference computer program for modeling earthquake wave propagation in bedrock on a regional basis.[1] A special purpose finite-element program has also been developed for simulating the nonlinear response of cable-supported bridges.[2] This program exploits the special characteristics of cable-supported bridges to arrive at an efficient and economical simulation model for nonlinear time history analyses.

These tools are being applied in a case study to an important bridge on the West Coast of the US. The San Francisco-Oakland Bay Bridge is located in California, crossing the San Francisco Bay and connecting the cities of San Francisco and Oakland (**Fig. 1**). The bridge was completed and opened to traffic in 1936. Currently, the bridge carries an average of more than 280,000 vehicles per day and is one of the busiest major bridges in the US. The bridge consists of two steel suspension bridges in tandem on the western crossing of the bridge, and a series of cantilever and simply-supported truss spans on the eastern crossing. The bridge has two decks, each deck with five car lanes. During the 1989 Loma

Prieta earthquake, a 15-m-long segment of the eastern crossing bridge deck collapsed, causing closure of the bridge for one month. Since the Loma Prieta earthquake, this bridge system has been the subject of a number of research and design studies supported by the California Department of Transportation. This bridge was selected for the current study because the bridge and surrounding seismic setting embody all of the important issues related to long-span bridge response. The bridge is also a key transportation link for the San Francisco Bay Area and additional insight into the seismic response adds information to the knowledge base for this critical structure.

Progress

Ground Motion Modeling

Ground motion synthetics for long-span bridges must include waveform information across a frequency range which encompasses the characteristic frequencies of the structure. In long-span cable bridge structures, this can represent a very broad frequency range since the long wavelength modes of the deck system can exhibit very low frequencies (0.1 to 0.05 Hz) relative to the vibrational frequencies of the bridge towers (5 to 8 Hz). Historically, very long period motions have not been accounted for in seismic hazard characterizations because of a lack of understanding of ground motion phenomenology and the unknown existence of long-period ground motion pulses. In the last few years, with additional insight gained by a handful of near-field ground motion measurements, the importance of long-period motions have become clear. Analytical and numerical studies of wave radiation patterns have confirmed the potential for large, long-period ground displacement pulses and significant permanent ground displacements in the near field. Ground motion observations obtained from the 1992 Landers, California earthquake in particular have provided insight into these important issues, with observations of large, long-period displacement pulses near the fault.[3] However, the paucity of near-field strong motion measurements leaves significant uncertainty regarding the precise waveforms of near-field motions. Seismologists must rely on analytical and numerical methods to provide engineers with estimates of the near-field wave forms.
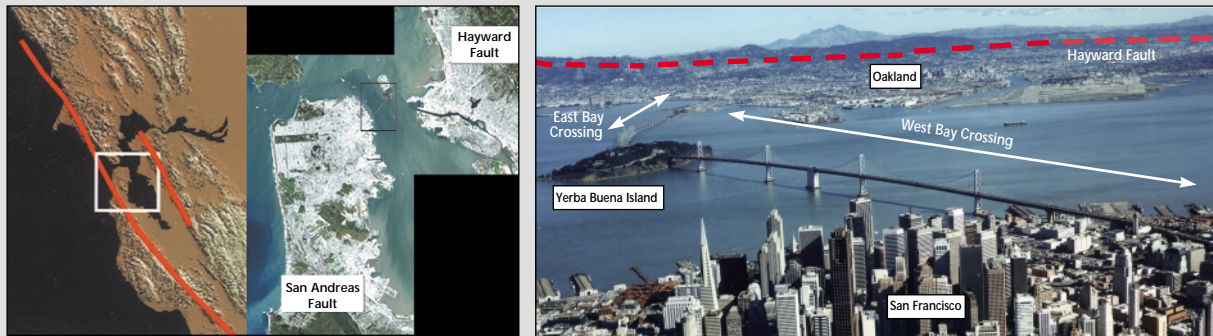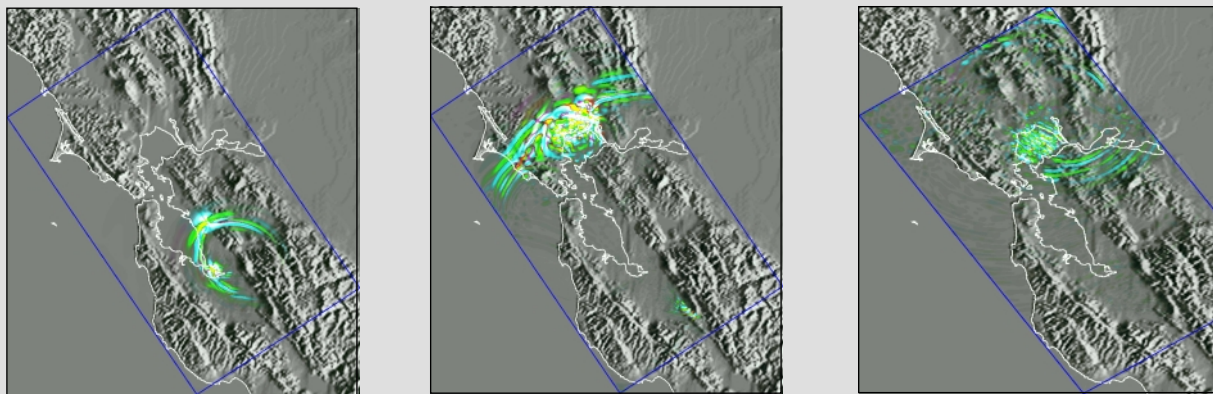

Figure 1. The San Francisco-Oakland Bay Bridge and local faulting. (a) Eastern and western crossings and fault locations; (b) computed regional wave propagation for an M = 7 Hayward fault earthquake.

The ground motion estimates completed for this study were generated using forward computations with physics-based models. To capture the required broad-band motion two approaches were used. The high-frequency components of motion were determined based on a Green's function approach in which small micro-earthquakes occurring along the Hayward fault were measured over a period of time with sensitive seismic sensors in bedrock (**Fig. 2a**) at the Bay Bridge site. The small earthquakes serve as empirical Green's functions which incorporate information about the complex path and site response characteristics as seismic waves emanate from a "patch" on the fault to the site of the structure in question.
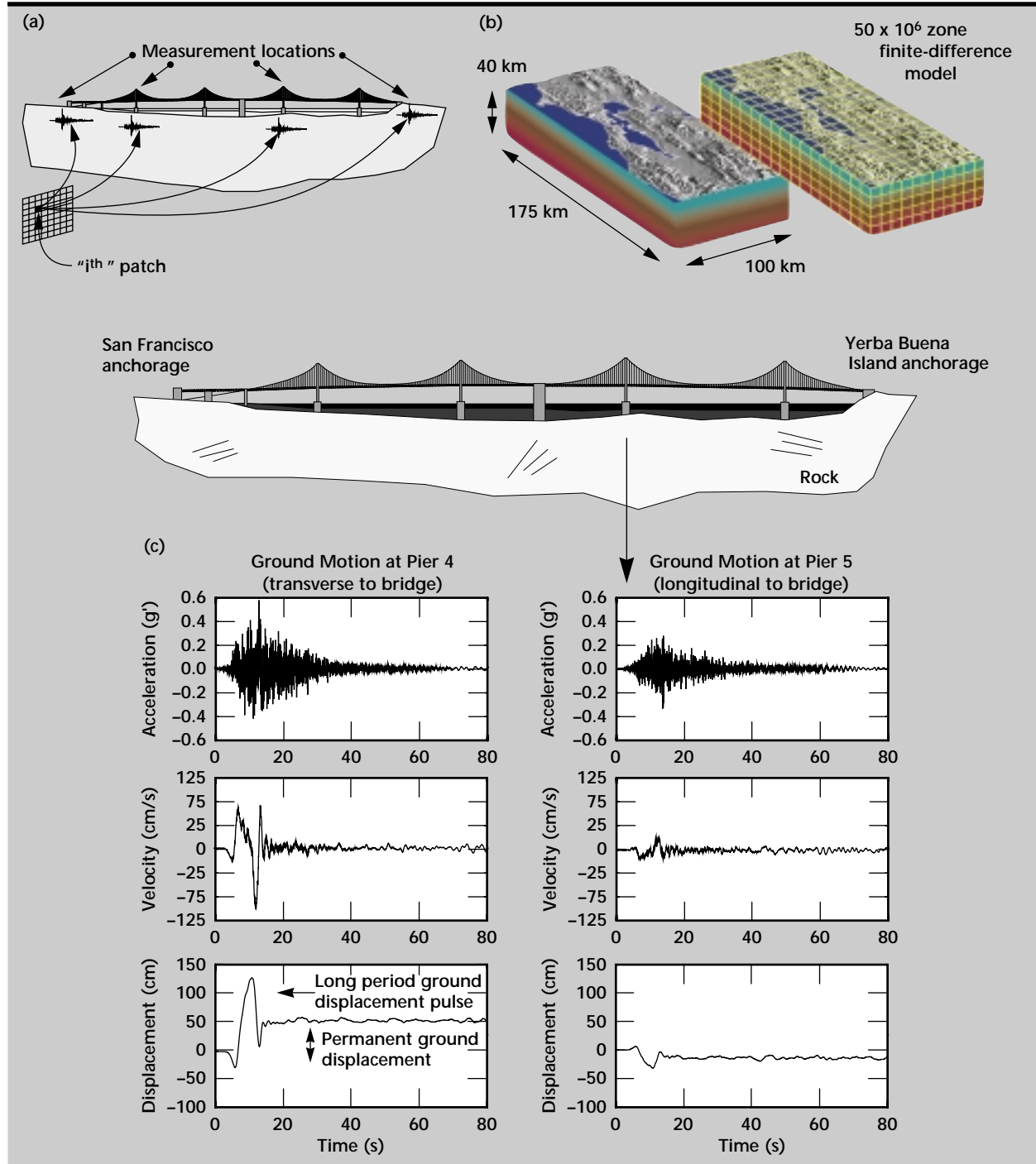
Figure 2. Broad-band synthetic ground motion generation. (a) Measured small micro-earthquake motions at the bridge site serve as empirical Green's functions for high-frequency motions; (b) regional massively parallel finite-difference model for low-frequency motions; (c) bedrock motions for one idealized fault rupture scenario for an M = 7 Hayward fault earthquake.

By appropriately summing up the sources for the entire fault region through a convolution process, the site motion for a large earthquake can be estimated.[4,5] The small micro-earthquakes which are recorded to construct the empirical Green's functions are deficient in long-period information because the small events do not generate significant energy at long wavelengths. Research studies have indicated that the Green's functions can resolve motions down to approximately 1 Hz, with lower frequency motions being in the signal noise.

To develop understanding of the long-period motions which could occur at the bridge site, and to augment the high-frequency motions from the Green's function method, a massively parallel finite-difference model was constructed for the Bay Area region. This model consisted of 50×10^6 regular finite-difference zones of 1/4 km dimensions. The existing geologic database does not provide sufficient spatial detail on the inhomogeneities in the earth to warrant any finer discretization of the geology.

This lack of geology definition on a fine scale results in a frequency limitation in the simulation as higher frequency wave components of motion are scattered by the inhomogeneities which cannot be characterized in the model. As a result, the numerical simulations provide information at frequencies of approximately 1 Hz and lower. The complete synthetic broadband characterization of site ground motions is obtained by a frequency domain merging of the high-frequency motions obtained from the empirical Green's functions method with the low-frequency motions obtained from the massively parallel simulations.

The specific manner in which the fault rupture evolves during an earthquake has a large effect on the ground motions at a specific site. Since the precise manner in which the fault ruptures is not known *a priori*, a number of potential fault rupture scenarios must be investigated when developing the hazard for a particular site. Recent research indicates that on the order of 25 to 30 rupture scenarios should be examined to capture the variability of the fault rupture process. **Figure 2** shows example synthetic ground motions at the Bay Bridge site for one particular rupture scenario for an M = 7 Hayward fault earthquake. This particular rupture scenario, which corresponds to a bilateral rupture propagation on the Hayward fault with rupture initiating adjacent to the Bay Bridge, results in a particularly large ground displacement pulse at the bridge site.

Structural Modeling

The San Francisco-Oakland Bay Bridge consists of two segments: the West Bay Crossing, which is the subject of this study, connecting the city of San Francisco with Yerba Buena Island, and the East Bay Crossing, which connects Yerba Buena Island with the city of Oakland (**Fig. 1**). The West Bay Crossing consists of twin suspension bridges in tandem connected to a central anchorage pier. The central anchorage pier was specially designed to resist the unbalanced live load of the suspension cables of the two suspension bridges. The foundation system chosen for the bridge was open caissons, which include the central anchorage caisson and the caissons which support each tower. The caissons were placed directly on bedrock and rely entirely on self weight to maintain contact with the bedrock. There is no positive anchorage system to resist uplift of the caissons. The San Francisco anchorage consists of a concrete block supported on bedrock and the Yerba Buena anchorage consists of a cable bent and eye-bar chains buried in two reinforced concrete filled tunnels.

The steel towers are attached to the piers by 40 anchor bolts connected to steel girders deep in the concrete piers. The suspension bridge towers consist of two multi-cell legs braced to each other with diagonal elements and struts. The tower legs are silicon high-strength steel while the diagonals and struts are mild carbon steel. Each of the main cables are attached to the tower tops with a single cast steel saddle. The main cables consist of 37 strands with each strand having 472 wires, each wire having a diameter of 5 mm. The deck stiffening trusses are Warren type trusses with the individual truss members constructed with laced steel members. The ends of the stiffening trusses are supported on rocker posts. The rocker posts provide transverse restraint but permit longitudinal movement of the stiffening trusses to accommodate thermal expansion and contraction. Expansion joint connections limit longitudinal motion of the trusses to approximately 36 cm outward and 25 cm inward.

In this research, a special purpose nonlinear finite-element program, SUSPNDRS, has been developed for the transient nonlinear analysis of cable bridge structures. The program uses special element technologies which were developed to significantly reduce the number of degrees of freedom required to accurately characterize a cable bridge system. The program includes capabilities for both geometric and material nonlinearities. The program accounts for finite displacements in the

bridge system and uses an updated Lagrangian framework for each structural element in which a local element coordinate system tracks with the element through space and time to remove gross rigid body displacements.

The five major components of the bridge model are illustrated in **Fig. 3**, and the details of the bridge model element technologies are provided in the referenced report.[2]

One of the objectives of the simulation model development was the construction of a transient solution framework which could handle a multiplicity of strong nonlinearities, including the abrupt and strong nonlinearities associated with impact and contact in the bridge system. The solution algorithm which was developed consists of a hybrid implicit-explicit algorithm whereby the initial static state of the bridge under gravity load is determined based on an implicit solution with Newton equilibrium iterations. A static load initialization procedure has been developed which allows the SUSPNDRS program to compute the correct static geometry and element forces starting with any arbitrary initial geometry definition of the bridge cables and deck.[2] Once the appropriate gravity configuration is achieved, transient earthquake analysis is carried out with an explicit, central difference-based time-integration scheme. The explicit scheme is particularly powerful, and has significant advantages over implicit time-integration schemes traditionally used in earthquake computations, when modeling the impact and contact associated with caisson rocking or deck-to-tower or deck-to-caisson impacts. Rigorous modeling of contact phenomenon can lead to significantly increased computational effort, or complete lack of appropriate convergence in implicit integration schemes, whereas the efficiency of explicit schemes is not adversely effected by contact.

In the explicit scheme, the bridge equations of motion are formulated in terms of absolute displacements rather than the displacements relative to the ground and the specification of multiple support input motions is trivially simple.
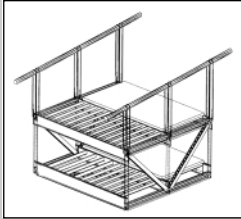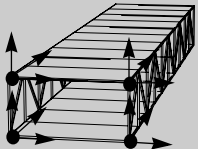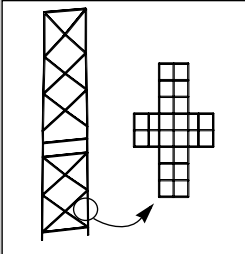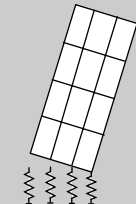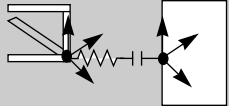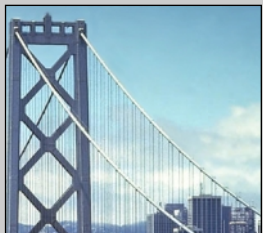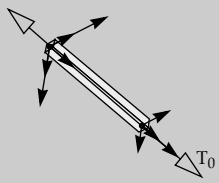

Figure 3. Components of the bridge system model.

Simulated Earthquake Response

The large ground displacement pulse in the synthetic earthquake records (**Fig. 2**) has a total time duration on the order of 5 s. For stiff structures, which exhibit natural periods of vibration significantly shorter than 5 s, the structure would have minimal dynamic response to this long duration pulse and would move essentially as a rigid body with the ground motion. For long-period flexible structures, on the other hand, this long-period pulse can significantly excite the lower frequency modes of vibration, providing a significant dynamic impulse to the structure.

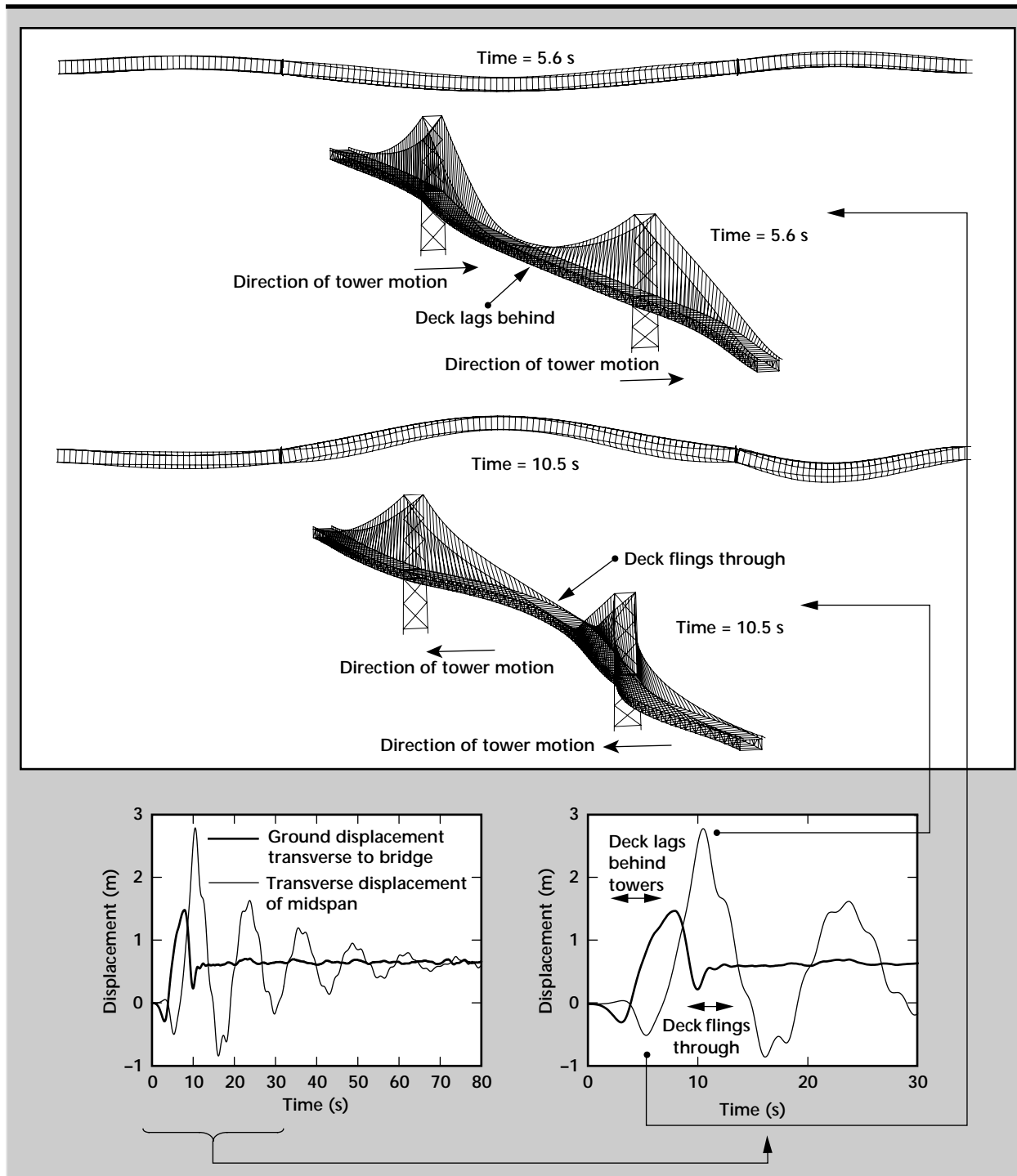The fundamental vibrational mode of one of the Bay Bridge suspension segments consists of

Figure 4. Displacements of bridge system due to near-field motions containing a large displacement pulse.

transverse vibration of the main span. Based on field measurements completed in 1936, and natural mode computations from the current study, the fundamental mode has a period of approximately 9 to 10 s. Thus the ground motion pulse duration is almost exactly one-half the natural period of the bridge. The result is that the ground displacement pulse imparts tremendous energy to the Bay Bridge system at the start of the earthquake motions. Animation of the bridge response indicates that the towers of the bridge move with the ground, while the mainspan deck can't respond fast enough due to its large mass and flexibility and it essentially lags behind the towers. As the deck finally starts to move to catch up with the displaced towers, the tower motion has reversed direction and started to move with the ground displacement pulse in the opposite direction (**Fig. 4**). The result is that the main span deck is essentially flung between the towers in sling shot fashion, with a large transverse displacement and corresponding high stresses in the deck system.

An assessment of the member forces for this earthquake loading indicated that a large number of main load-bearing members would be significantly overstressed. The deck beams, which connect the deck slabs to the stiffening trusses, would be particularly susceptible to damage from the deformations associated with the deck fling.

Conclusions

Two new computational tools have been developed for simulating earthquake ground motions and the response of long-span cable bridges. These tools are shedding light on the nature of near-field ground motions, including long-period and permanent displacements which can occur in the near-field, and the damaging effects these motions can have on flexible, long period structures.

References

1. S. C. Larsen and C. A. Schultz (1995), "ELAS3D:2D/3D elastic finite difference wave propagation code," Lawrence Livermore National Laboratory, Livermore, California (UCRL-MA-121792).

2. D. B. McCallen and A. Astaneh-Asl (1997), "SUSPN-DRS: A numerical simulation tool for the nonlinear transient analysis of cable supported bridge structures," Lawrence Livermore National Laboratory, Livermore, California (UCRL-ID-127626).

3. W. D. Iwan and X. Chen (1995), "Important near-field ground motion data from the Landers earthquake," *Proc. 10th Eur. Conf. on Earthquake Eng.*, A. A. Balkema, Vol. **1**, pp. 229–234.

4. L. J. Hutchings (1991), "Prediction of strong ground motion for the 1989 Loma Prieta earthquake using empirical Green's functions," *Bull. Seis. Soc. of Am.*, Vol. **81**, pp. 88–121.

5. L. J. Hutchings (1988), "Modeling strong earthquake ground motion with an earthquake simulation program EMPSYN that utilizes empirical Green's functions," Lawrence Livermore National Laboratory, Livermore, California (UCRL-ID-105890).

Signal Processing for Evaluation and Update of Simulation Models in Structural Analysis

Gregory C. Burnett and Gregory A. Clark
Defense Sciences Engineering Division
Electronics Engineering

David B. McCallen
Center for Complex Distributed Systems

Charles R. Noble
New Technologies Engineering Division
Mechanical Engineering

We are developing a methodology that uses model-based signal processing to compare simulations of structural responses with measured data. The work completed to date indicates that the model-based signal processing can readily identify significant differences between a simulation model and an actual measured structure. The signal processing algorithms can also be used to detect changes in a structure associated with damage in the system. The appropriate placement of sensors in under-observed systems is critical and sensor locations should be based on as much structural insight as possible.

Introduction

The design of engineering systems has traditionally resulted from a mix of theory, empiricism, and experience based on historical performance. With the advent of high-performance computers and massively parallel computations, the hope is that simulations based on first principles will play an even more commanding role in the engineering process. However, for this to come about, it is essential that large-scale simulation models yield demonstrably accurate results for the particular problem type under study. The ability to validate computational models, based on a rigorous comparison between the actual measured system response and the simulated response, is a requisite to building confidence toward a simulation-dominated engineering process.

Progress

Objectives

Our project is concerned with the evaluation and validation of computational structural models. The methodology under development relies on model-based signal processing to compare simulations with measured structural response. The signal processing algorithms are intended to determine the degree to which the simulation model represents the actual behavior of the structure, and to provide guidance on how the simulation model could be improved. In addition, the signal processing can sense changes in the structural system, which offers the potential for establishing an approach for damage detection in large structural systems.

There are important programmatic applications which could immediately benefit from the ability to reconcile simulation models with actual measured structural response. These applications span a range of structural types and loading regimes including the rather violent vibrational response of reentry vehicles in missile flight tests, the small amplitude ambient vibrations of optical components and structures for the National Ignition Facility (NIF), and the vibrations and transient response of large transportation structures to earthquake ground motions (**Fig. 1**).

In year one of this study, the framework for model-based signal processing has been established and the ability of the signal processing to sense differences between a simulated and a measured structure has been studied parametrically. We have also investigated the degree to which model-based signal processing can identify the regions of the

structural model which are deficient and the ability of the signal processing to provide guidance on how to update the computational model to enhance accuracy. The important questions of observability and how many sensors are required to provide adequate measurements have also been addressed.

Model-Based Signal Processing

The signal processing methodology under development follows the procedure outlined in **Fig. 2**. The essential inputs to the signal processing include the matrices which result from the finite-element structural simulation model, including mass $[M]$, damping $[C]$, and stiffness $[K]$ matrices, and the measured response of the structure for a given loading. Ideally, the structure should be subjected to carefully controlled white noise type of excitation for the initial model identification process so that the input forcing function is precisely known and a wide range of vibrational modes are excited.

The model-based signal processor uses the finite-element-generated system matrices as a starting point and constructs a simulator of the system based on a state-space first-order equation system characterization of the second-order finite-element equations of motion. A Kalman filter-based residual whiteness test is used to detect any divergence between the simulation model and the actual structure response. A Gauss-Newton search routine minimizes

Figure 1. Applications of model-based signal processing.
(a) Understanding complex fluid-structure iteration in flight dynamics, including model validation and appropriate data reduction; (b) validating design model simulations and understanding ambient vibrations for NIF; (c) validating simulation models for massive transportation structures and developing damage detection capabilities.

a) High fidelity flight test

Complex fluid-structure interaction
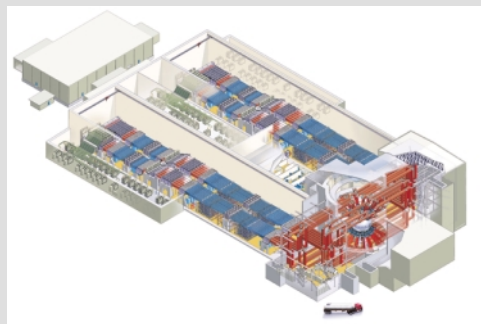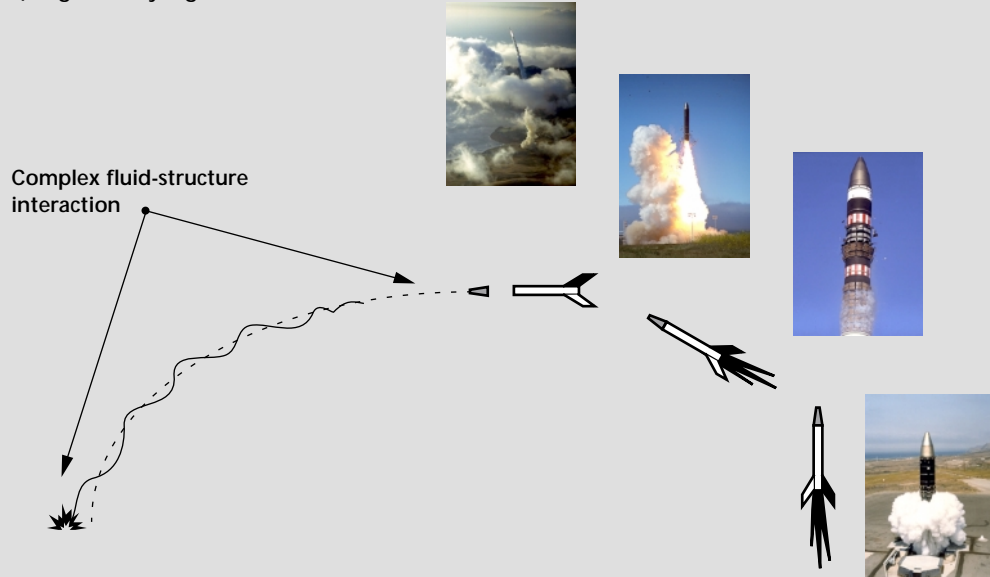
b) Large applied physics facilities

c) Earthquake response

the differences between the simulation model and the measured structure in a least squares sense. The minimization process results in system identification in which optimal structural model parameters are identified. These optimal parameters (indicated by the updated system matrices in **Fig. 2**), can be passed back to the finite-element model for parameter update. The signal processing also provides a methodology for damage detection in that changes in the structure which are associated with damage can be sensed once the virgin, undamaged structure is appropriately identified.

The signal processing procedure which has been developed has been studied parametrically by extensive investigation of a simple dynamic structural system, a five-story building model, as shown in **Fig. 3**. The utility of this example is that with appropriate idealization of the member section properties, the number of degrees of freedom in the model can be easily varied from as low as 5, to as high as 500, with maintenance of the same basic system dynamics. The equations of motion can also be readily written down analytically as shown in **Fig. 3**. This allows issues of observability and scaling of the signal processor to be readily investigated.

This simple example was used in paper studies to evaluate the ability of the signal processing to detect divergence between simulated and real structures and to identify appropriate model parameter modifications. To achieve this, a finite-element model was constructed for the structure, and a perturbed finite-element model was constructed to represent the "real" structure. For example, one perturbation might consist of modifying all stiffnesses of the structure by a significant margin. Another might consist of modifying selected segments of the structure in a local fashion. The signal processing algorithm was then called upon to identify differences between
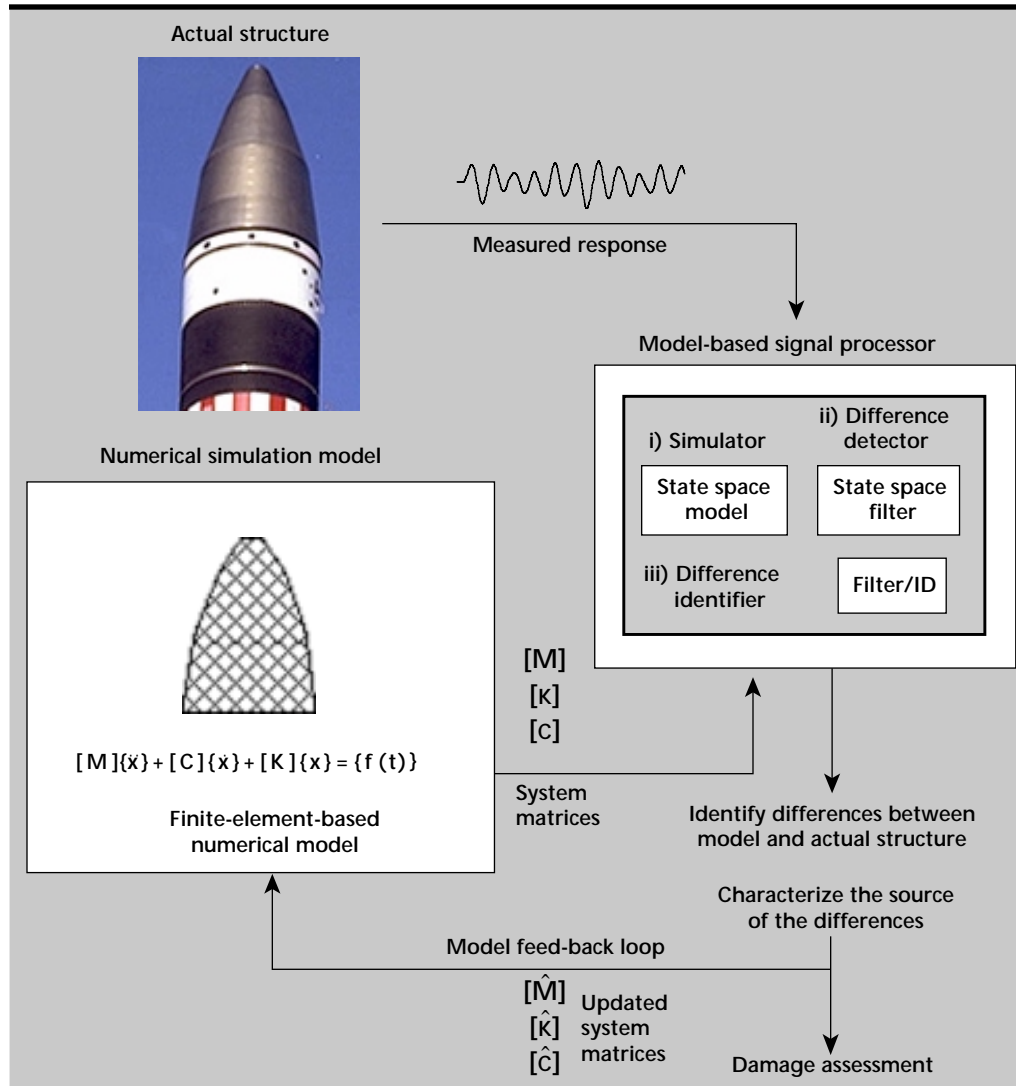

Figure 2. Model-based signal processing for evaluation and update of simulation models.

the simulated and "real" structures and to identify structural parameter updates for the simulation model.

These studies were carried out in blind fashion, whereby the mechanical engineering team members constructed the simulated model and the data from the measured "real" structure and passed this information to the electrical engineers responsible for the signal processing. Thus the signal processors were dealing with two sets of information with no prior knowledge of the structural perturbations.

For the simple baseline system with 5 degrees of freedom fully observed, the signal processing algorithms readily identified the differences between the

simulated and "real" structure, and provided the appropriate parameters for the model update, as illustrated with a subset of examples in **Fig. 4**. For this analysis the response of the model was simulated for a white noise forcing function applied at the top of the structure, and the "measured" response of the "real" structure was also computed with a perturbed model for the same white noise forcing function.

For a fully observable system (for example, the acceleration response of all five floors was assumed measured), the signal processing was found to be very robust, and could accurately ascertain that the
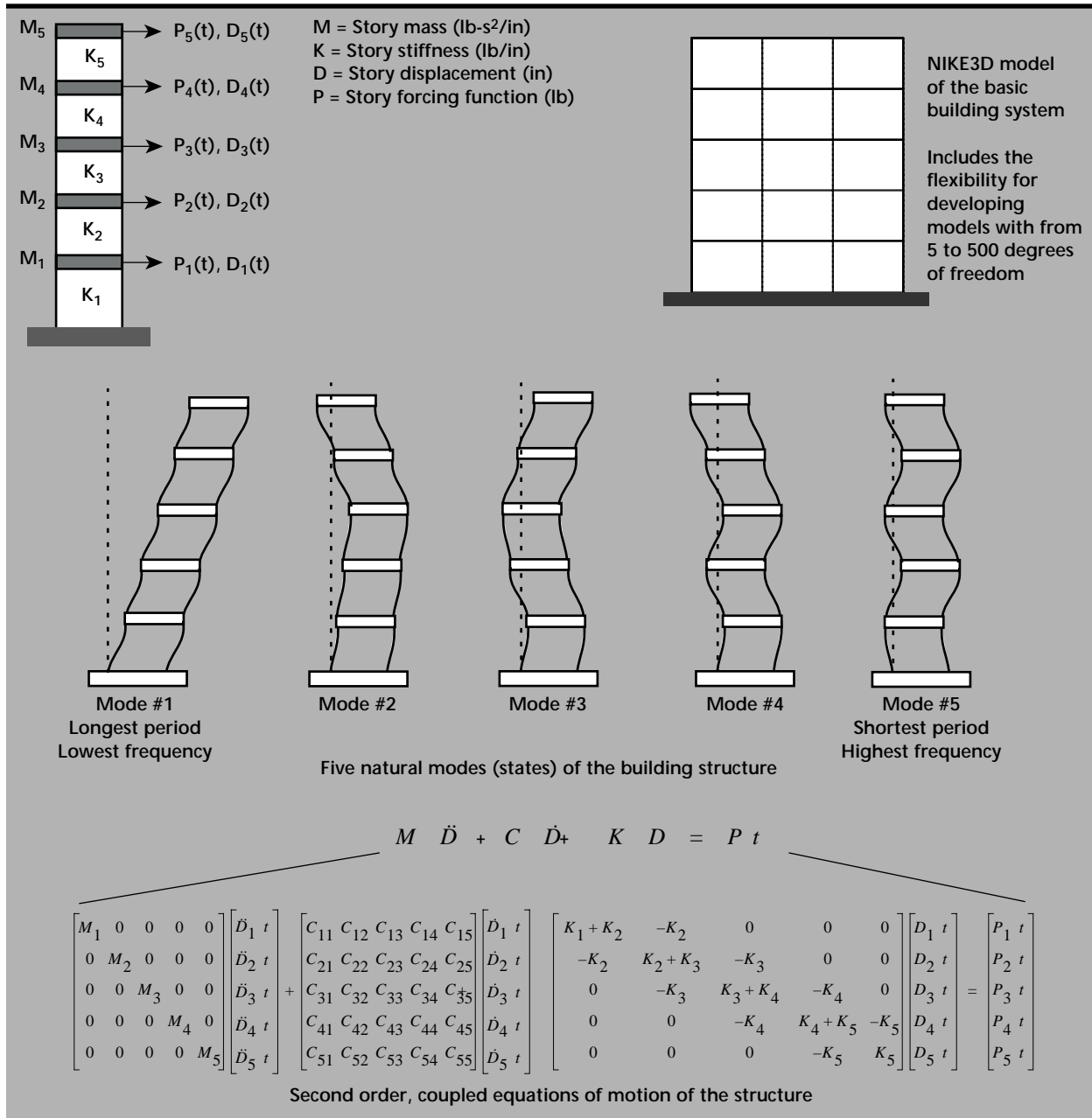

$$M \ddot{D} + C \dot{D} + K D = P\,t$$

Second order, coupled equations of motion of the structure

Figure 3. Simple dynamic system consisting of a five-story shear building.
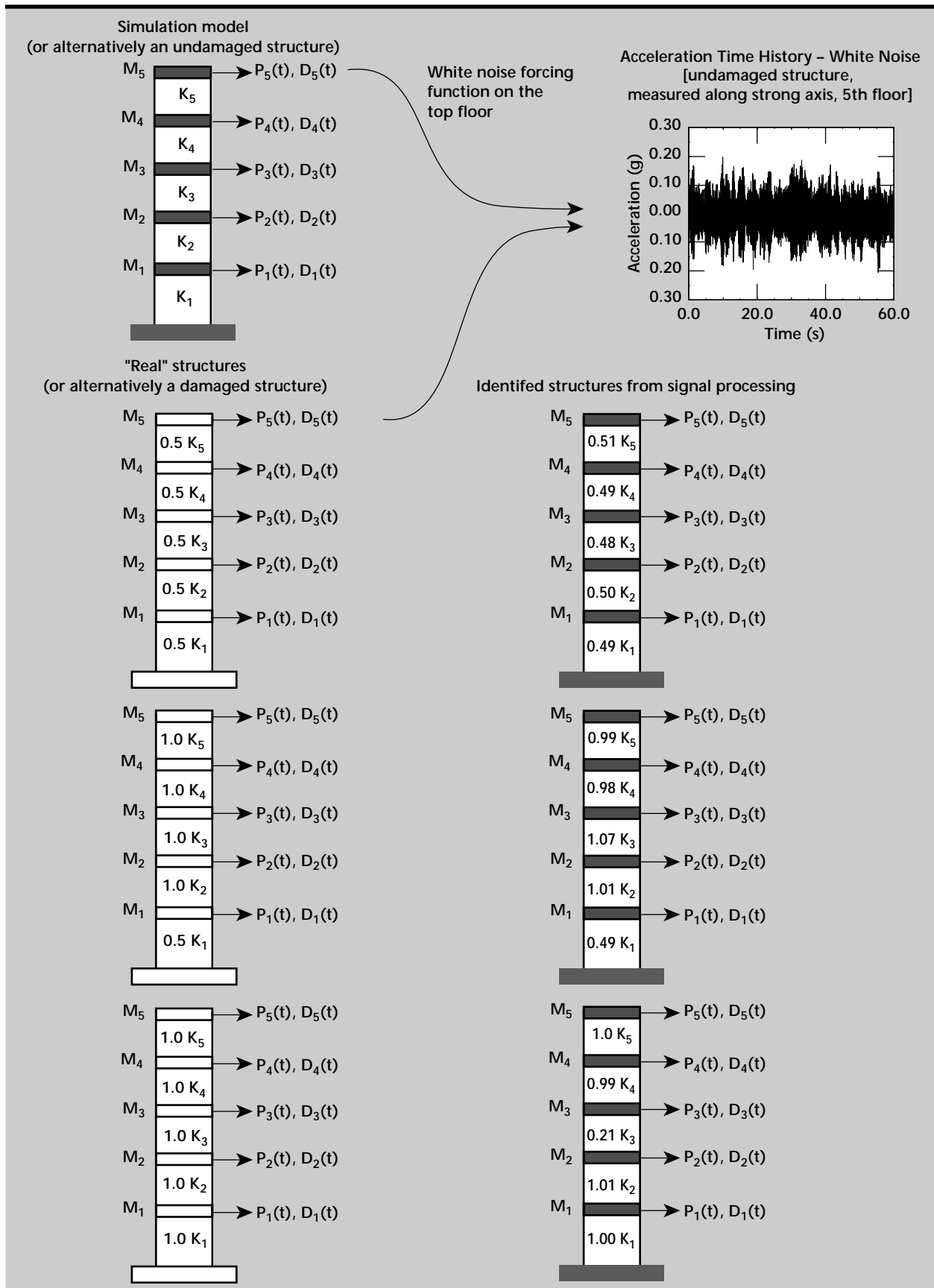
Figure 4. Identification of structural properties from the model-based signal processor.

model and "real" structure were different, as well as identify the correct distribution of the stiffness in the "real" structure.

It should be noted that the differences between the simulated and "real" structure in **Fig. 4** could equally well be interpreted as the differences between an undamaged structure (the modeled structure) and a damaged structure (the "real" structure). Thus, if one can ascertain that two structures are different and how they are different, damage detection is enabled.

In actual large structures, full observability (for example, every point in the actual structure corresponding to a degree of freedom in the finite-element model is measured), is a condition which will rarely if ever be achieved. Because of typical limitations in the number of sensors and the amount of data which can be measured practically, almost any real system will be significantly under-observed.

The potential impact of low observability has also been investigated with the simple shear building model. For this investigation, the dimension of the model was increased to 10 degrees of freedom with appropriate master-slaving of the active degrees of freedom. The ability of the signal processing algorithm

to correctly identify the structure with a reduced set of observations was investigated for a number of different observation schemes. For this analysis the perturbation to provide the "real" structure was as indicated in **Fig. 5**. This perturbation represented a significant and complex change from the original structure. With all 10 degrees of freedom observed the mean error in the identified stiffness parameters was $1.2 \times 10^{-9}\%$, which verifies that precise identification is achieved for a fully observed system. The mean error in the system identification for various under-observed scenarios is summarized in **Fig. 5**.

In **Fig. 5** the cross-hatched box indicates a floor at which translation was "measured" and a hollow box indicates a floor at which translation was not measured. These results indicate that the accuracy of the signal processing identification tends to be significantly lower if measurements are not made for the top two stories of the building. This is correlated to the fact that the fourth and fifth stories have the most significant change in stiffness and, if there is not a local sensor measurement to capture the dynamics of this softening region, the system identification can miss these significant changes.
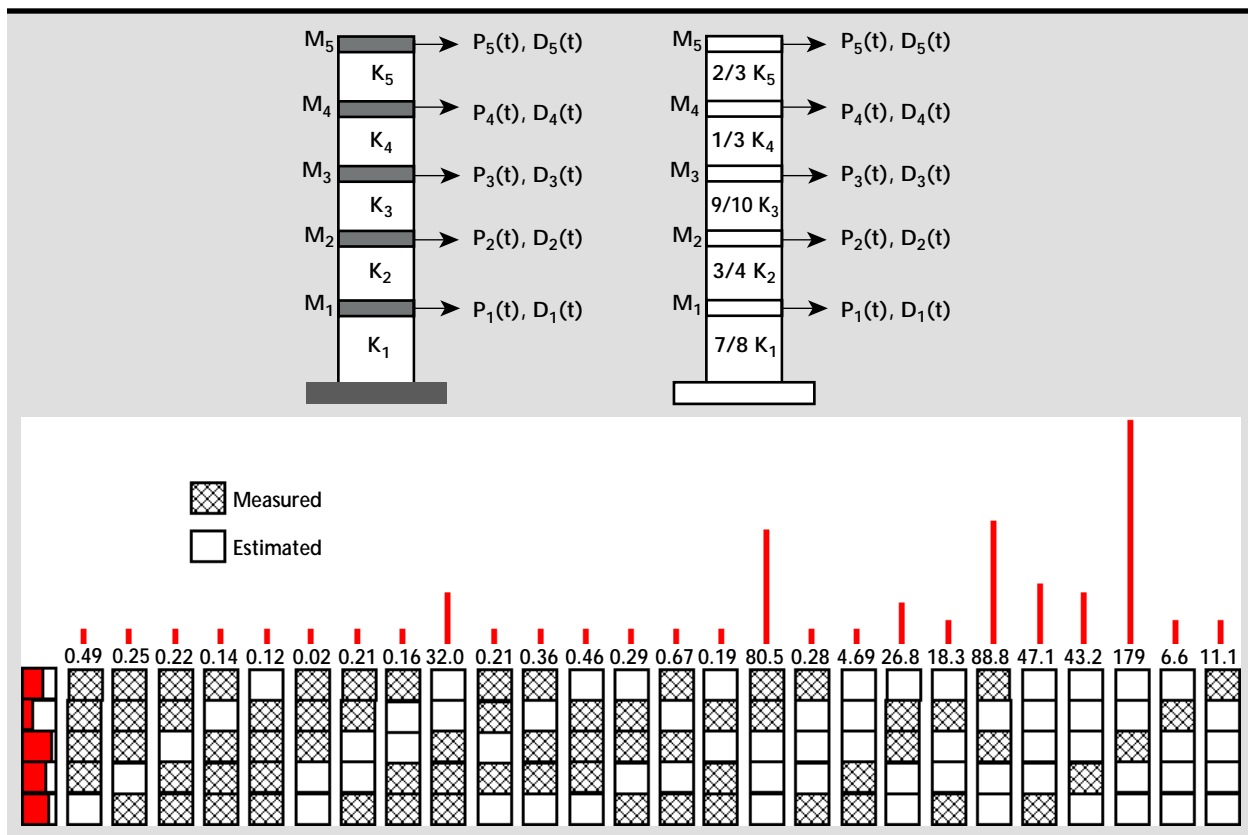

Figure 5. Accuracy of signal processing system identification if reduced observations are made.

Perhaps just as significant is the observation that if the top floor alone is measured (such as with only one observation), the system identification still does a reasonable job of parameter estimation. These observations underscore the need to have adequate measurements in the regions of the structure for which a high degree of uncertainty is anticipated or, alternatively, regions where damage to the structure might be anticipated.

Future Work

The second year of this project will investigate applications for some real structures, in which real-world issues associated with noisy data come into play. The focus will also include scaling up the existing signal processing algorithms to attack much larger structures.

Controlled Biological Systems for Sensor Platforms

Dino R. Ciarlo
Electronics Engineering Technologies Division
Electronics Engineering

Jonathan Simon
New Technologies Engineering Division
Mechanical Engineering

Matt Harren
Cornell University
Ithaca, New York

We have been developing wireless circuits for the control of the Madagascan Hissing Cockroach with the intention of using them as distributed sensors or possibly in search and rescue missions.

Introduction

During the past several years there has been research into the controllability of various insects by external stimuli such as electrical pulses to their antennae area. Prof. I. Shimoyama started the work at the Tokyo University in Japan. In the U.S., Prof. S. Crary, a physicist at the University of Michigan, conducted pioneering work. More recently there have been over 30 projects of this type funded by the Defense Sciences Office of DARPA. The scope of the DARPA projects includes: the response of the animals to stimuli, animal experiments, animal models and the development of low power, light weight controlling circuits and sensors. For the past year, we have been developing wireless circuits for the control of the Madagascan Hissing Cockroach with the intention of using them as distributed sensors or possibly in search and rescue missions.

Progress

We decided to experiment with the Madagascan Hissing Cockroach following the advice of Prof. Crary of the University of Michigan and Dr. M. Willis, an entomologist at the Arizona Research Laboratory, Division of Neurobiology, University of Arizona. Both Crary and Willis are being funded by DARPA to study the neural control of flight steering in the *Manduca sexta* moth.

The Madagascan cockroach is a robust animal, easy to work with. These animals are often used as displays in grammar and high school biology classes. The name hissing comes from the hissing noise they make when annoyed. They generate the noise by expelling air from their abdomens. The Carolina Biological Supply Co. in North Carolina sells them but they cannot be shipped into California. We found cockroach colonies at the University of California at Davis and at the Clorox Co. in Oakland; the managers of these facilities were ready to give us animals to experiment with. Instead, we purchased three adult female cockroaches from a pet store for $5 each. We kept them in a suitable container and fed them dried dog food, bread, lettuce and water. They remain quite active even after six months of experiments.

In our experiments, we attempted to steer the Madagascan cockroach by the use of two LED light sources mounted on either side of the cockroach's head. **Fig. 1** is a photograph of the electronics components. The larger circuit board on the left contains the left and right button and the transmitter electronics. The smaller circuit board on the right contains the receiver circuit and is mounted on the animal's back. We used transmitters/receivers from RF Monolithics and microcontrollers from Microchip Technology to remotely activate one or the other of the LEDs. The transmitter/receiver operates at a frequency of 916.5 MHz. The circuit was designed so that if a 1-kHz signal was received by the receiver
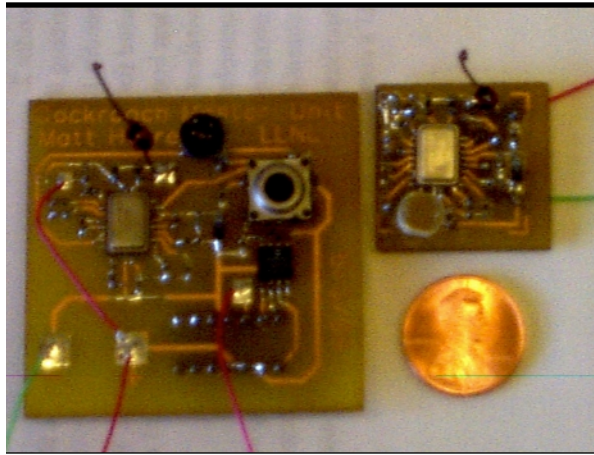
Figure 1. Photograph of electronics system used to steer cockroach.

Figure 2. Photograph of cockroach with installed electronic backpack and two LEDs.

on the animal's back, the left LED would light, but if a 3-kHz signal was received the right LED would light. The entire backpack on the animal, including the 3-V battery weighs 5 g. The cockroach weighs 7 g and is capable of carrying over 100 g. **Fig. 2** is a photograph of this configuration of a cockroach with the installed electronic backpack and two LEDs. These animals are nocturnal and the thought was that they have an aversion to light and would turn in a direction away from any light source.

In actual tests, we did see a tendency for the animal to turn away from the light source. However, this was observed once the animal was in forward motion. Often we had to resort to extra effort to get the animal moving (such as a slight nudge from behind). In addition, the turns in response to the light signals tended to be rather gradual. We did not see any right angle turns. Also, of the three animals we had in captivity, one was especially responsive while the other two showed little interest in our experiments.

Future Work

We demonstrated the ability of the Madagascan cockroach to carry wireless, battery powered circuits on their backs. They certainly have enough carrying capacity to add an environmental sensor to the transmitter/receiver package we used. The cost of this electronics is not high, just a few dollars. We concluded from our work that best scenario would be to outfit hundreds of these animals with such electronic backpacks and then let them wander on their own, sending back information on the environment, without attempting to steer them.

An Instrumentation System for Remote Monitoring of Large Structures

Mathew S. Hoehler, and Charles R. Noble
New Technologies Engineering Division
Mechanical Engineering

David B. McCallen
Center for Complex Distributed Systems

Jon P. Lewis
Defense Sciences Engineering Division
Electronics Engineering

We have developed a new instrumentation system for the remote monitoring of structures. A key element of the system, which enables practical application to large structures, is a wireless communication capability, allowing remote contacting of the system to provide commands and to retrieve measured data. The application of this system to vibration monitoring has demonstrated the utility of such a system and has provided the opportunity for optimization and fine tuning of the system design.

Introduction

The design and analysis of large structural systems has become increasingly reliant on computational simulation. As the speed of computational engines increases, computer memories grow, and massively parallel simulations become commonplace, the trend toward reliance on simulations will continue and likely become even more pervasive. With the increase in fidelity of simulation models, there are great expectations that simulations will provide improved understanding and insight into the way in which structures respond to various loading conditions. However, in many respects our ability to discretize and compute has significantly outpaced our ability to test and verify our computational models. There is a pressing need to ensure that the ever larger models which are being constructed are actually representative of the structure being simulated.

There are two topical areas which necessitate research and development attention to address the growing model validation deficit.

The first area deals with the need for expedient collection of response data from large, distributed structures. Traditional wired sensor and data acquisition systems are not capable of practical monitoring for very large structures. Recent experience with wired system monitoring of large structures (**Fig. 1**) has shown that the placement and continuous data collection tasks will be intractable for structures like a large applied physics facility on the scale of the National Ignition Facility (NIF) at Lawrence Livermore National Laboratory (LLNL) or a transportation structure of the size of the Bay Bridge (**Fig. 2**). For example, LLNL engineers recently performed field experimental testing of the famous Bixby Creek Bridge near Carmel, California (**Fig. 1**), and that experience was found to stretch the application of wired data acquisition systems to the limit.

The second topical area deals with the processing of measured response data once the data is obtained. There is an immediate need to develop robust algorithms which rigorously compare simulated system response and actual measured system response, quantify limitations and shortcomings of the simulation model, and prescribe appropriate perturbations to the simulation model.

The project described here dealt with the problem of monitoring large structural systems. A companion article in this report deals with the second issue of data processing and model update.

Progress

Our focus was the development of a wireless instrumentation system which can be used to monitor very large structural systems. The overall
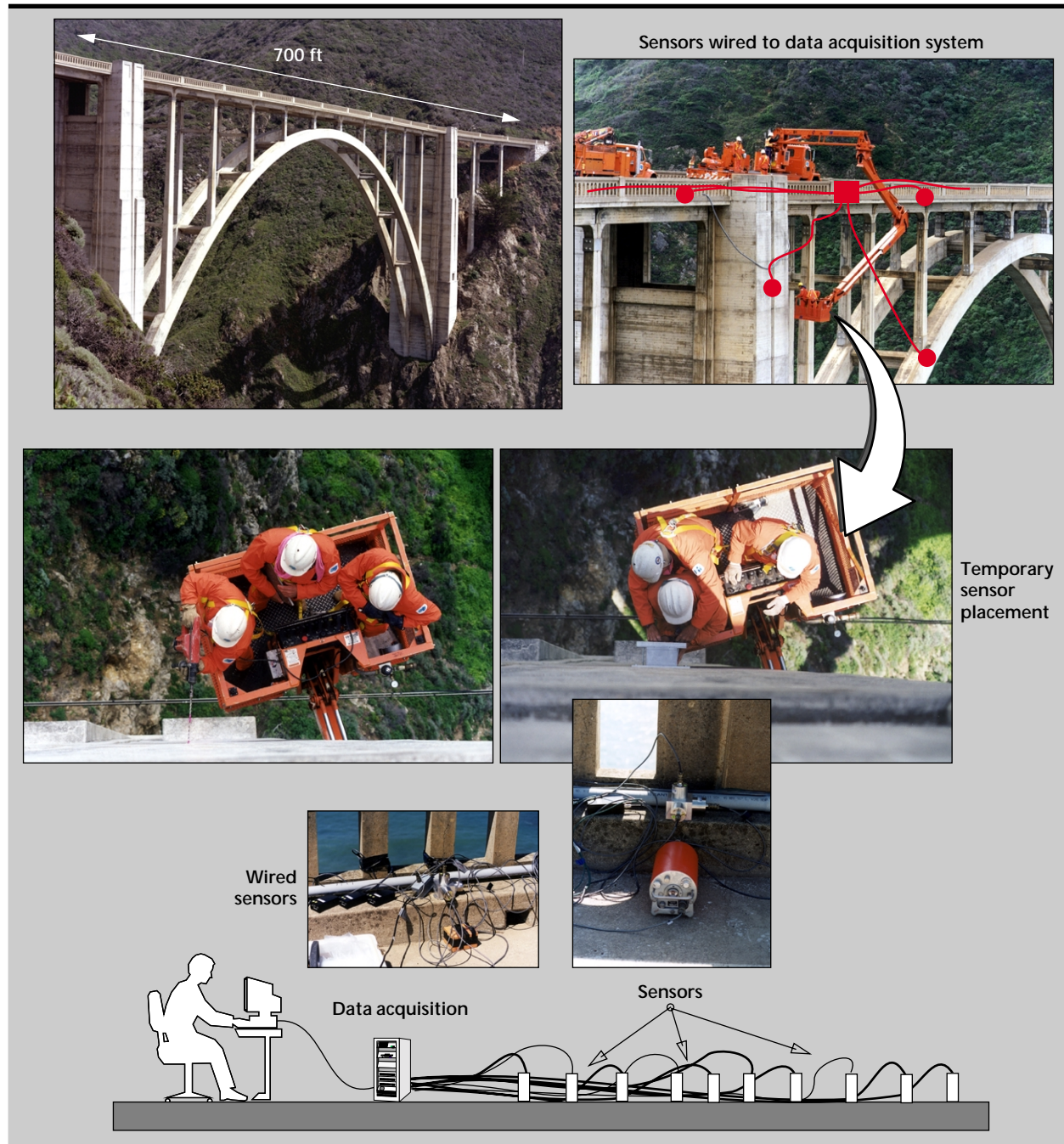
Figure 1. Traditional structural monitoring with a wired system. LLNL study of Bixby Creek Bridge is shown.

strategy was to construct the most economical system with readily available, commercial off-the-shelf components. The specifications for this system included:

1. capability for remote access to allow adjustment and setting of system parameters and downloading of data;

2. incorporation of sensors, amplifiers and sampling rate which would allow selectable data acquisition over a large amplitude range (such as ambient vibrations to strong earthquake motions) and a broad frequency band (from 15-Hz modal vibrations typical of stiff NIF structures, to 0.1 to 0.2 Hz vibrations of a long-span bridge); and

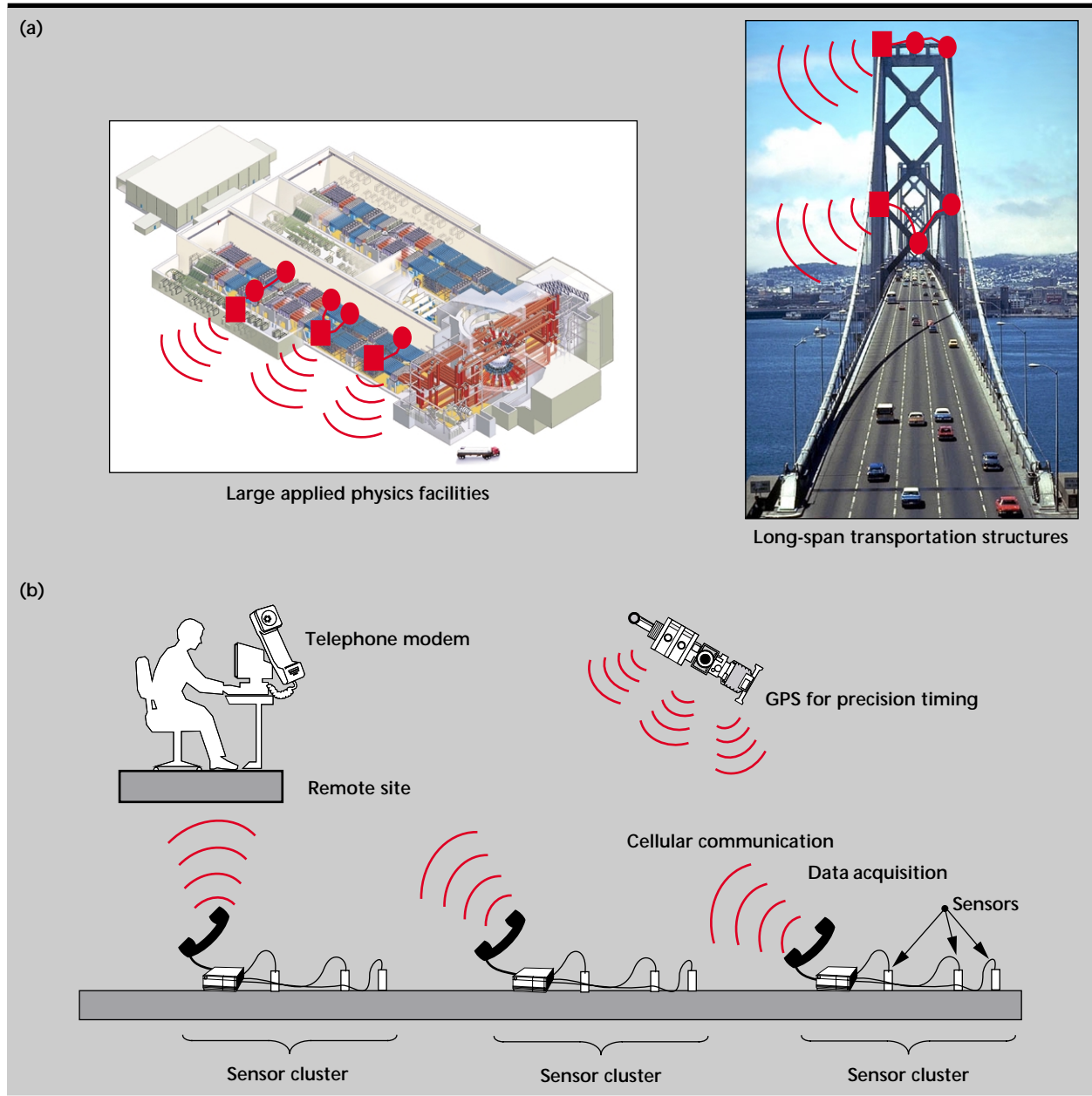3. capability for accurate time keeping so that all measurements can be referenced to a precise time scale.

Figure 2. Structural monitoring of large distributed systems with remote data transmission. (a) Example structures which would benefit from distributed monitoring; (b) distributed individual sensor clusters.

In addition to these basic functions, the intent was to develop a modular system so that the various options could be mixed and matched to most economically suit a specific application. The project included the design of the overall system, construction and testing of a prototype system and a field application of the prototype system at the NIF construction site. A corollary objective was to provide data for validation of the NIF vibrational design criteria.

The ultimate objective of the instrumentation system is to allow placement of an array of sensor clusters around a distributed structure, such that the local sensor clusters are wired to individual data acquisition systems and each data acquisition system can be remotely accessed for data download, as indicated in **Fig. 2**. This pattern of instrumentation was selected after careful review of the maturity of communication technologies and consideration of system costs and reliability. For example, wireless communication between individual sensors and the data acquisition system would be very desirable, but was judged too expensive and potentially problematic with regard to reliability within the context of cost-effective 1999 technology.
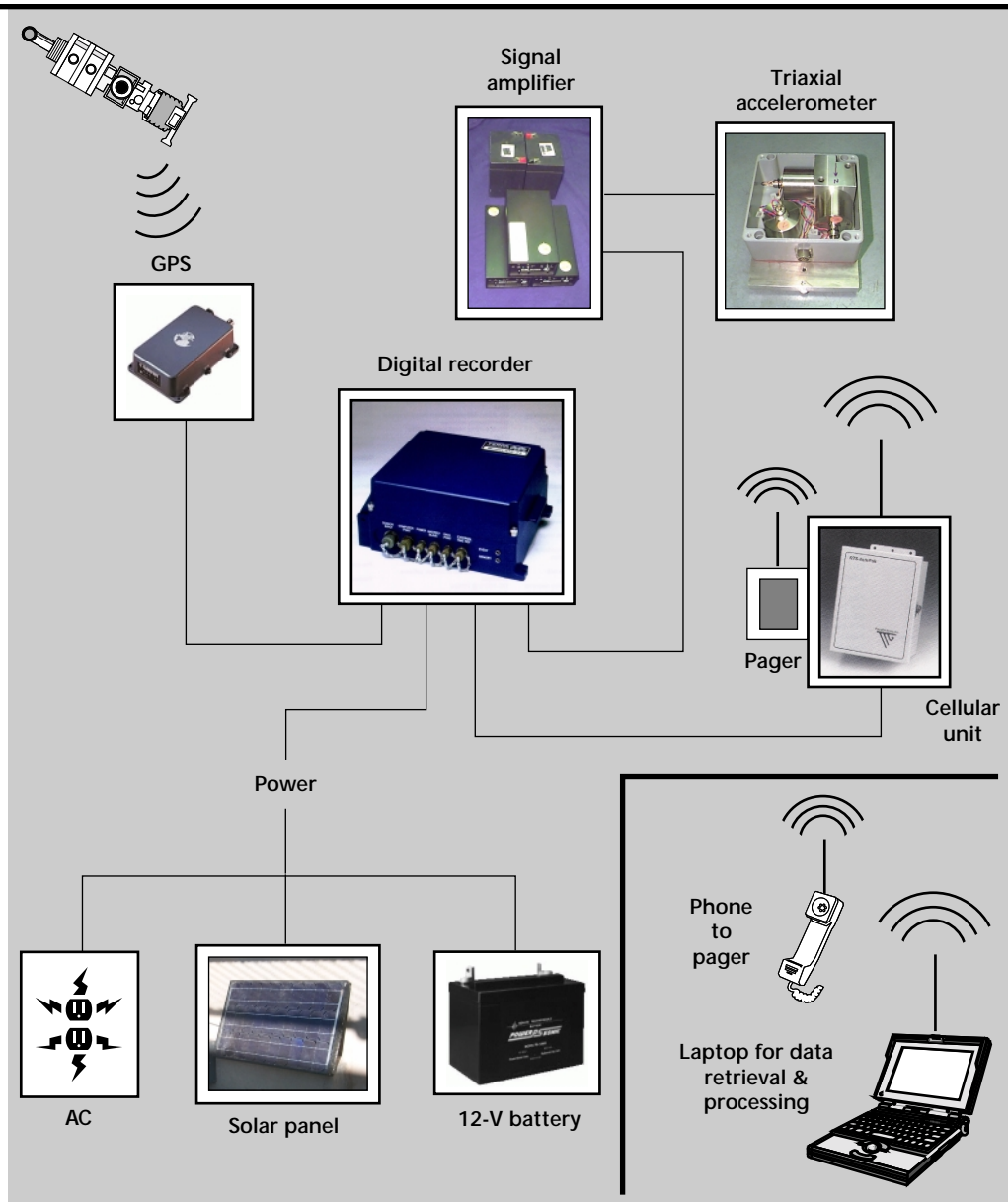
Monitoring System

The monitoring system, shown schematically in **Fig. 3**, was developed to provide the required funtionality. All of the system components, with the exception of the sensor housing, were commercially purchased. The system sensors consist of heavy seismographic accelerometers, housed in a stiff aluminum container designed and built at LLNL. The massive accelerometers provide good signal-to-noise performance in the low frequency regime. The sensor housing was designed to ensure strong coupling through rigid mounting and to mitigate potential vibrations of the housing which could affect sensor measurements. Commercial signal amplifiers were used, and the digital recorder was constructed to LLNL specifications by a commercial vendor. Each digital recorder has a companion GPS unit for accurate positioning and precision timing, and a cellular-phone-based communication transmitter/receiver for remote communication with the system. The system can be contacted via a laptop computer with a phone modem. The system can be powered with AC hook-up or a solar panel. A battery power option was included for immediate applications in the NIF construction area.

In the course of the development, it was found that the cellular communication system was a major source of power consumption in the instrumentation system. To assist in minimizing power usage, a pager system was implemented which allowed the system to be "beeped," thus powering up and turning

Figure 3. Instrumentation for sensing, data recording and storage, precision timing, and communications.

GPS

Signal amplifier

Triaxial accelerometer

Digital recorder

Pager

Cellular unit

Power

Phone to pager

Laptop for data retrieval & processing

AC

Solar panel

12-V battery

on the cellular communication package. The cellular package can then be powered down after information is relayed or data is retrieved.

An essential element of the development of any data acquisition system is the establishment of the accuracy of the measured data. This is particularly important when a number of different electronic components are being interfaced together. The accuracy of data obtained with remote monitoring instrumentation system was thoroughly evaluated by careful comparison with existing high performance data acquisition systems (**Fig. 4**). A series of experiments

were conducted for a number of different types of dynamic loadings and the performance characteristics of the system were established by comparison of the new remote monitoring system with a system which has had long-term use and multiple validations for LLNL seismological applications.

After validating the first prototype of the remote monitoring system, the system was deployed at the NIF construction site to monitor ambient ground motions over an extended period. Such a deployment provided for evaluation of system performance, including communications, power usage, and data
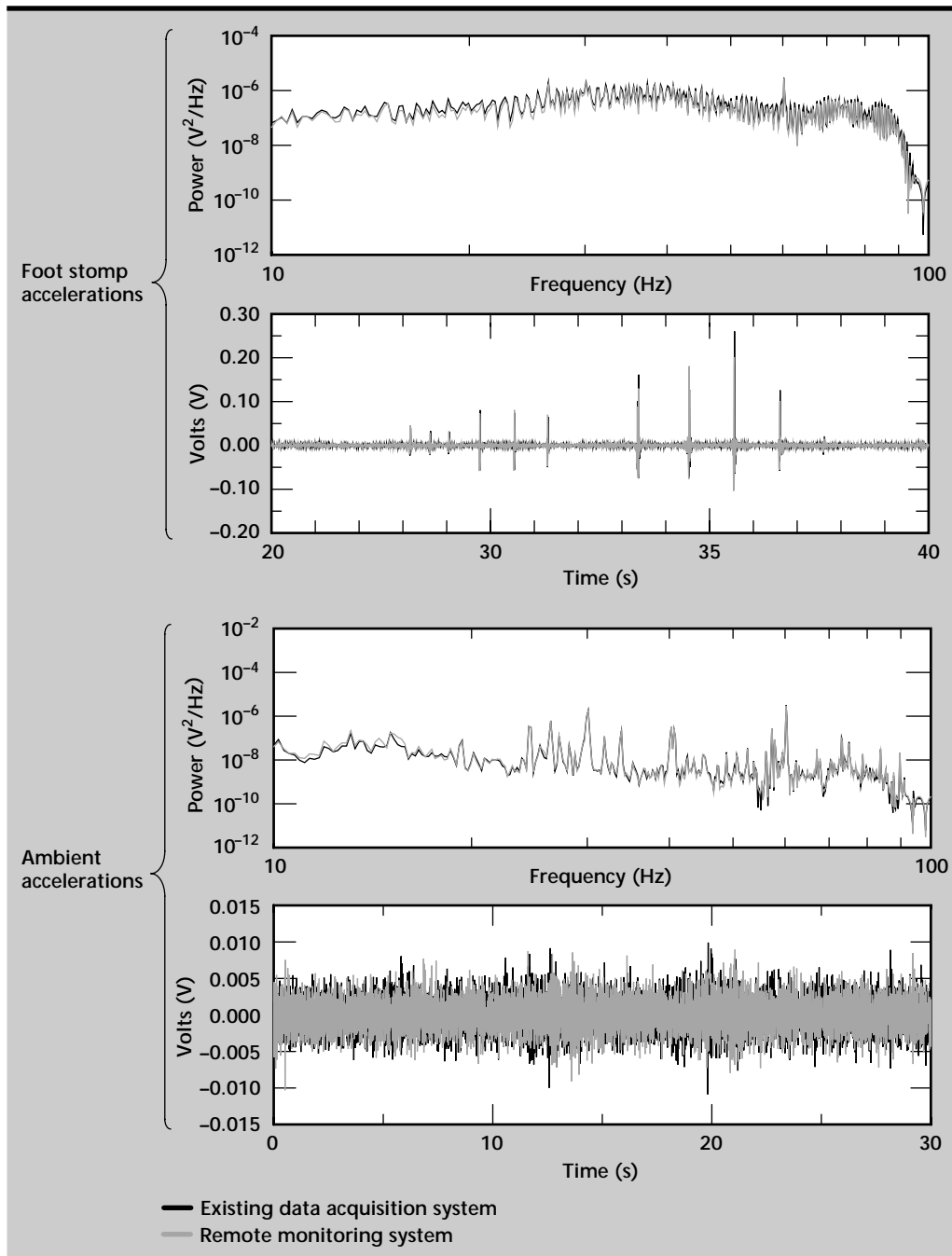

Figure 4. Power spectral density functions and time histories of existing data acquisition system and remote monitoring system for various loadings.

Foot stomp accelerations

Ambient accelerations

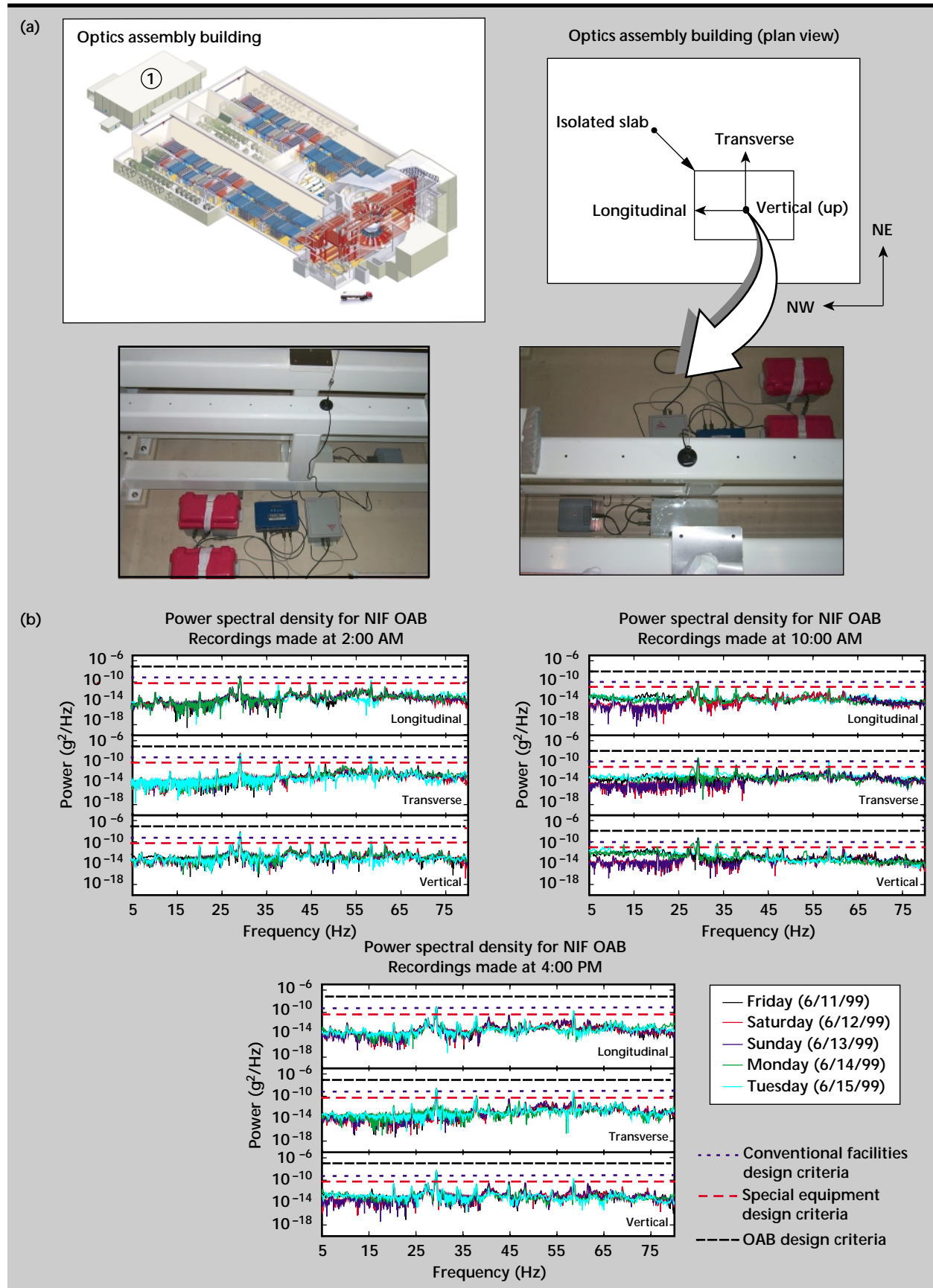— Existing data acquisition system
— Remote monitoring system

Figure 5. Measurements of ambient vibrations at LLNL's NIF. (a) Instrument locations; (b) measured vibrations at different times of the day.

transfer rates, and also provided important site specific data for validation of the NIF ambient vibration design criteria. The monitoring system was located in the Optics Assembly Building (**Fig. 5**), where the facility was at cleanroom Protocol 2 during the measurements and the access was limited. In addition, AC power was unavailable, so battery operation of the monitoring system was essential. The capability to remotely contact the system, to set recording starting and stopping times, and to download measured data, was essential for this application.

The ambient vibration measurements indicated that the site vibrations were generally within the NIF design specifications (**Fig. 5**). There were spikes in the power spectral density plots at 30 Hz and 60 Hz which were indicative of vibrations due to running equipment. As NIF construction progresses, ground vibration monitoring will continue and particular attention will be paid to the equipment frequency ranges.

Conclusion

An effective wireless system has been developed for monitoring large structural systems. This system provides a tool for practical acquisition of vibration data essential to understanding system response and validation of system computational models.

Underground Facilities Characterization

Rexford M. Morey
Laser Engineering Division
Electronics Engineering

Michael H. Buettner and William D. Daily
Electronics Engineering Technologies Division
Electronics Engineering

Neutralization of underground facilities (UGFs) is identified by the US military as a high priority because underground facilities may be used for the manufacturing and storage of weapons of mass destruction (WMD) or for other purposes of military importance. Effective neutralization and battle-damage assessment, especially in a hostile environment, requires the deployment of unattended sensor systems for detecting and/or imaging subsurface conditions. For the past several years geophysical techniques have been evaluated for solving this problem. However, seismic methods cannot provide the level of detail the military needs on the internal structure of UGFs.

Ground penetrating radar (GPR) has been used to investigate shallow subsurface situations. In many soil conditions the penetration depth of a single GPR unit is limited. Theoretical considerations and preliminary experiments indicate that a large array of simultaneously excited radar transmitters will substantially increase the depth of penetration (on the order of tens to hundreds of meters). To our knowledge, the design and deployment of a multi-element GPR array has not been done because of the cost, complexity and data-handling requirements. Several preliminary experiments were performed at tunnel sites at the Nevada Test Site (NTS) to evaluate the efficacy of GPR arrays to characterize underground structures. These tests included measuring the bulk conductivity of the rock and soil over UGFs, profiling a tunnel with a 25-MHz GPR system, deploying a small array of two synchronized GPR transmitters, and performing an electrical resistivity topography (ERT) survey over the same tunnel.

Introduction

Electromagnetic (EM) propagation through dispersive, inhomogeneous, and conductive materials, such as soil, rock, and biological tissue, is of continuing interest, especially when the goal is to "see" deeper targets with greater clarity. Currently, single-channel instruments, such as GPR, have a limited range of investigation in lossy media due to a limited equipment dynamic range or performance factor. However, new simulation and experimental evidence suggests that arrays of radar sensors could increase characterization depths of subsurface targets. The array would be composed of multiple, synchronized transmitters and/or receivers.

This report presents the initial steps of a new program to develop a core technology in high power arrays for 3-D image formation and visualization in dense media, such as the subsurface of the earth. The program is built on the extensive body of work at Lawrence Livermore National Laboratory (LLNL) in geophysics,[1–5] GPR imaging,[6–8] and laboratory measurements of EM properties of materials.[9] To determine the utility of high power ultra-wideband (UWB) arrays, "proof-of principle" experiments were performed. These experiments included EM measurements over tunnels at NTS.

Applications of high power arrays include characterizing UGFs, battle-damage assessment of targeted UGFs, detection and mapping of unexploded ordnance (UXO), and geophysical surveys, such as earthquake assessment and monitoring fluid flow. The deployment of a sparse multi-element UWB array, which includes multiple time-synchronized transmitters, has not been done before.

Progress

Electrical conductivity of soil and rock determines the depth of penetration of EM signals in these materials. High conductivity means limited penetration, low conductivity leads to greater penetration. Therefore, field measurements were made to get estimates of the bulk electrical conductivity of the rock at four sites at NTS. With this information estimates of the RF attenuation in the rock are calculated, and thus estimate the penetration depth of GPR at these sites.

Four areas at NTS were investigated: (1) the BEEF facility in area 4, (2) U-tunnel in area 12, (3) tunnel 16-A, and (4) tunnel 16-B. To measure the bulk conductivity we used a standard two-loop induction survey with a Geonics EM-34 tool. This system is designed to be used in the vertical dipole mode (coil lying on the ground surface) or the horizontal dipole mode (coils normal to the surface and coplanar). The instrument is designed to work with fixed loop spacings of 10, 20, and 40 m, and conductivity is read directly on a panel meter in mS/m. **Figure 1** shows the Geonics EM-34 being used at the BEEF facility.

Table 1 lists the measurement results at the four locations along with the estimated depth of penetration for a GPR operating at 25 MHz. **Figure 2** is a plot of maximum radar range as a function of electrical conductivity showing ranges to the tunnel sites. Available single-channel GPR systems have an advertised performance factor (Q) of about –110 dB. Improvements in Q, such as with multiple transmitters or signal processing, will increase depth of penetration.

Since Tunnel 16-B is an "active" tunnel being used as a test site by a number of investigators, and since reasonable penetration is predicted, GPR and ERT experiments were performed over this tunnel in September 1999. The GPR work used equipment rented from Sensors and Software, Inc. and was operated at 25 MHz. The ERT data acquisition system was developed at LLNL over a period of many years, and has been used successfully for a wide variety of imaging applications. Survey lines were established on the ground surface (**Fig. 3**), normal to the tunnel axis at overburden thicknesses of approximately 10, 12.5 and 20 m. The survey line at 12.5 m was used for ERT data collection.

The GPR equipment was assembled, set up, and tested. Profiles were collected along the 10- and 20-m lines, in the constant offset mode. That is, the transmitter and receiver were kept at a constant spacing (4 m) from each other, and the pair was moved in steps of 1 m along the survey line from 50 m on the east side of the tunnel to 50 m on the west

Figure 1. Electrical conductivity measurements at the BEEF facility, NTS.

Table 1. Results of electrical conductivity measurements at NTS.

Location	Rock	Conductivity (mS/m)	Estimated radar detection range* (m)
U-Tunnel	Dolomite	1.0 to 1.5	20 to 26
Tunnel 16-A	Ash-fall tuff	9 to 15	3.7 to 5
Tunnel 16-B	Limestone	2 to 2.4	14 to 16
BEEF	Gravel/soil	30 to 35	2.2 to 2.4

*Assumptions for GPR: 110 dB effective dynamic range, 25 MHz, metal mesh in roof.

side. At each survey point, the transmitter was fired many times, and the received signals were stacked (improves S/N) to produce a plot of received signal versus two-way travel time.

The resulting display is a series of these plots (one per survey point) slightly displaced from each other as one moves from left to right. When gain is applied to the data, the characteristic hyperbolic signature of a target (such as a tunnel) appears at about the right lateral position and depth, as shown in **Fig. 4**. The assumed dielectric constant for converting the time-scale to a depth-scale is 6, which is a reasonable value for moist rock. Our interpretation of **Fig. 4** is that the reflector at 10 m is from the top of the tunnel, while the reflectors above 10 m are moisture filled joints in the rock, joints created during tunnel construction. (There was a heavy rain about a week before this experiment.) Other reflectors appear in the data as well. A tunnel signature does not appear in the 20-m overburden profile, **Fig. 5**. These results are consistent with the predictions in **Fig. 2** for Q= –110 dB.

The final GPR work used two transmitters instead of one as described above. The reasoning is that two transmitters will increase the returned radar signal from the tunnel. The initial experiment to verify this used a receiver placed over the tunnel axis with a transmitter 4 m to the west and another 4 m to the

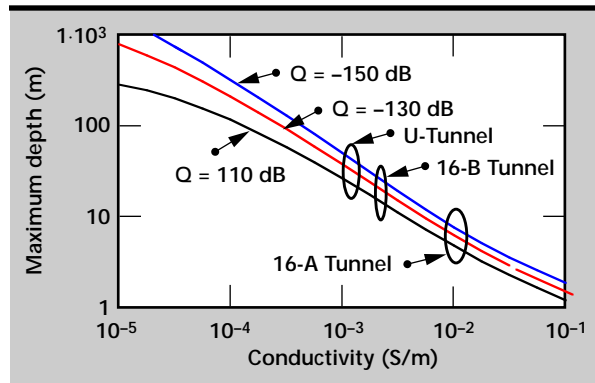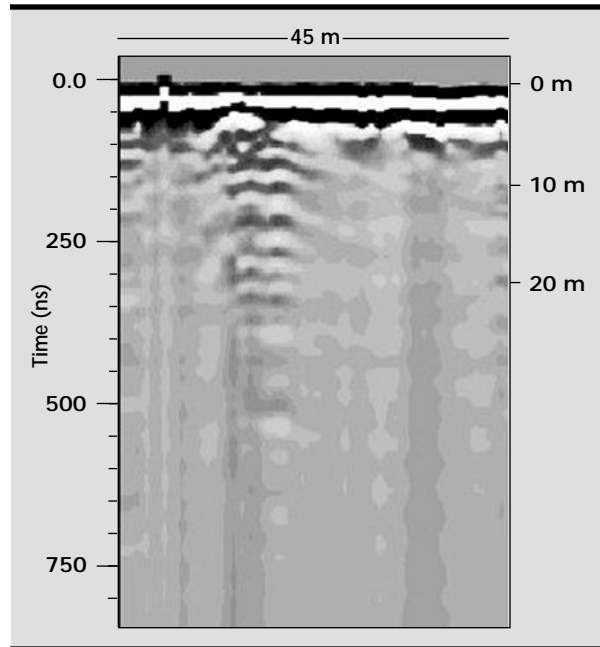*Figure 4. GPR profile at ~10-m overburden.*

Figure 2. Calculated maximum depth as a function of electrical conductivity and performance factor.

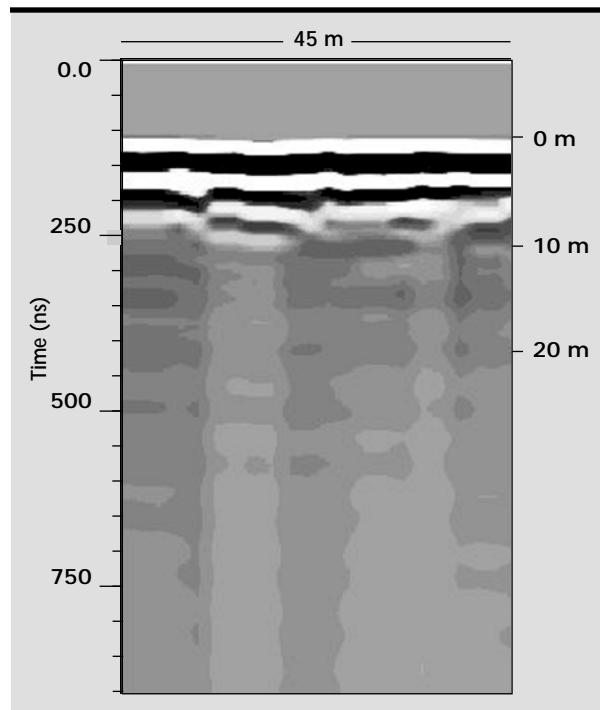*Figure 3. GPR and ERT survey area over Tunnel 16-B, NTS.*

Figure 5. GPR profile at ~20-m overburden.

east of the receiver, as in **Figs. 6** and **7**. A special trigger circuit enabled control of the trigger delay between the two transmitters. This is necessary because the paths from the two transmitters to the receivers are not exactly identical in terms of velocity. Thus to get the tunnel-reflected pulses from the two transmitters to arrive at the receiver at the same time, one needs to adjust the trigger delay between the two transmitters.

The final measurement used a receiver placed over the tunnel axis with two transmitters 4 m to the east (next to each other or collocated) of the receiver, as diagrammed in **Fig. 8**. If our hypothesis about superposing the returns from two transmitters is correct, this experiment should have essentially the same result as that described in the previous paragraph.
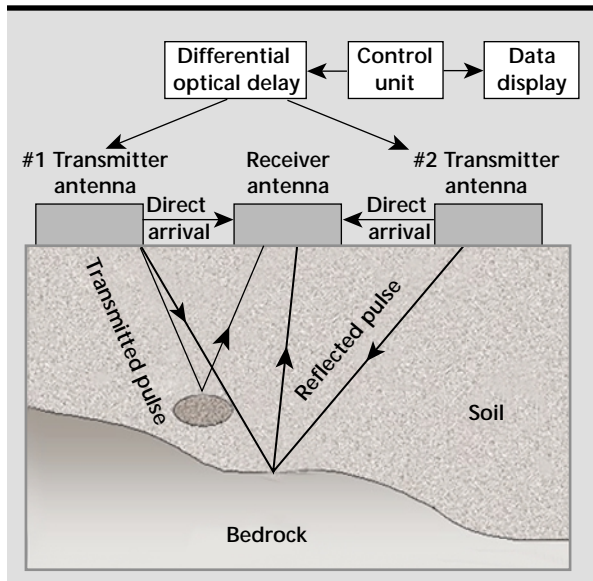
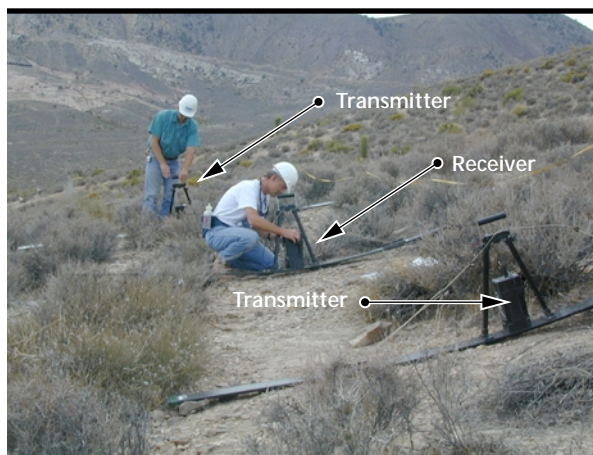The total variation in the differential trigger delay between the transmitters is about 30 ns. During the two-transmitter experiments, the differential trigger delay was incremented in 10 steps. For each delay-step, each transmitter was turned on and then off sequentially, then both transmitters were turned on together. **Figure 9** shows examples of the data for the two collocated transmitters over the tunnel. The upper panel displays the sequence of measurements for the 10 delay settings.

Interpretation involved looking for the strongest signal at a range of about 10 m, as shown in the lower left panel, where the tunnel reflections aligned in time for the three transmitter conditions, $T \times 1$ on only, $T \times 2$ on only, and then both on. The lower right panel shows the received GPR waveforms for these three transmitter conditions, plus the mathematical summation of $T \times 1$ on and $T \times 2$ on. Note that summing the two separate transmitter responses gives very similar results to having both transmitters on and time-synchronized at the target region.

The ERT survey was performed along the 12.5 m line. ERT data were collected using a 30-electrode array that extended from 145 ft (44.2 m) to the east of the tunnel axis to 145 ft. west of the tunnel axis. Data were also collected in the EOM mode in which the steel mesh and rock bolts in the tunnel are excited to some value of potential and the resulting potentials measured using the electrode array. **Figure 10** displays the two ERT inversions perpendicular to the tunnel axis.

The top image in **Fig. 10** is from data collected using only the 30 surface electrodes. The surface
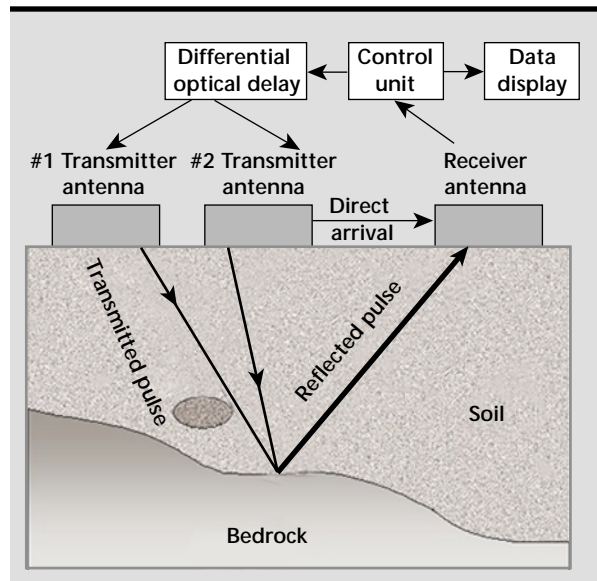

Figure 6. GPR setup using two transmitters.

Figure 7. Photograph of three GPR antennas, two transmitters and one receiver.

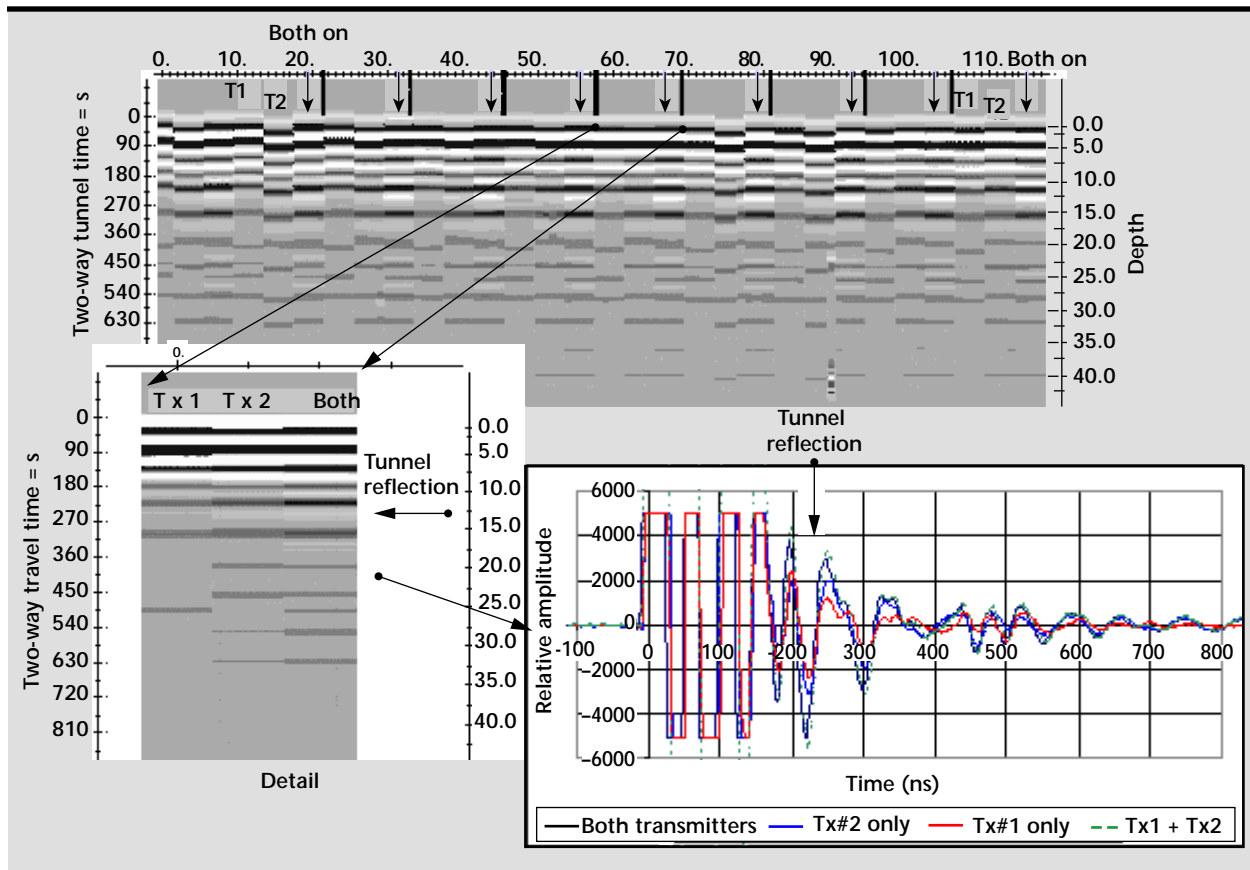Figure 8. Diagram of two transmitters collocated.

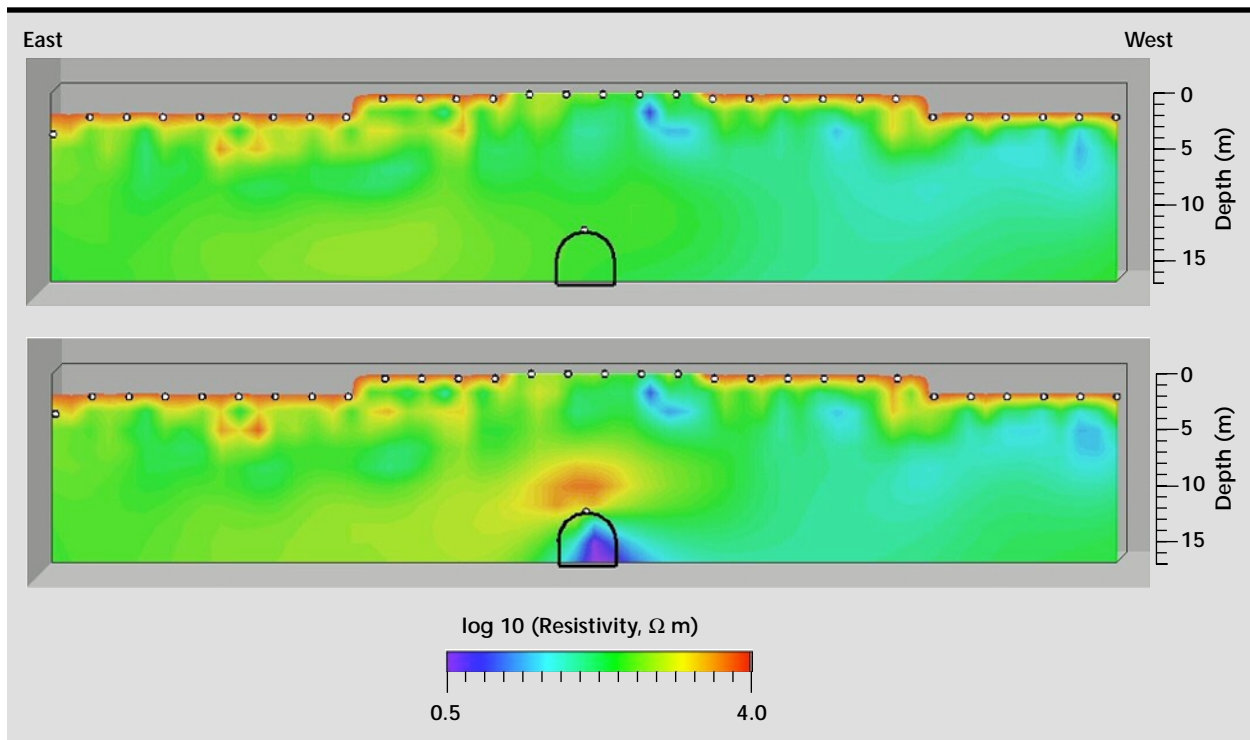*Figure 9. Examples of GPR data for the collocated transmitter experiments.*

Figure 10. ERT profiles over Tunnel 16-B, NTS.

topography is approximated by the discrete steps formed by the mesh blocks in the top row. The approximate outline of the tunnel section is superimposed. The formation resistivity varies between about 50 to 3000 Ω m with the most resistive part in the dry surface material. We do not know what geological feature causes the prominent conductive anomaly above and to the right of the tunnel. In this image the greatest sensitivity is near the surface and decreases rapidly with depth. At the tunnel depth the sensitivity is obviously too small to detect any effect of the void or the metal on the walls.

The lower image was inverted from data collected using the 30 surface electrodes and the single electrode in the tunnel. This data was collected only to see what additional information could be generated in the image using the additional electrode. Notice that the reconstruction is essentially identical to the top image except near the tunnel. The additional information added by the tunnel electrode, although distorted by the lack of spatial coverage, does give some additional information. The resistive region above the tunnel is likely the dehydration of the rock mass (loss of water results in increased resistivity) as a result of the tunnel ventilation. This region extends all the way around the tunnel but only the upper part is imaged here because of the way the electrode array is arranged. The conductive region below the electrode is likely the distorted image (again because of the electrode arrangement) of the wire mesh in the tunnel.

Summary

The GPR data indicate that (1) the tunnel was detectable at 10 m depth of overburden, but not at 20 m depth, and (2) two transmitters can be triggered properly so that additional energy can be put on target as indicated by a larger radar return. Without the additional electrode in the tunnel, the ERT survey did not detect any effect of the tunnel void or the metal in the tunnel.

Future Work

Groups both inside and outside LLNL are showing interest in multi-element UWB arrays. As an example, a presentation was made to DARPA on using UWB arrays for UGF characterization. Present day GPR will not reliably detect deep UGFs. Experimental studies indicate that a large GPR array will increase radar range to a level that will interest DARPA and also DTRA. These programs and others will be pursued.

References

1. R. J. Lytle and D. L. Lager (1972), "Electromagnetic propagation, transmission, reflection, and refraction: equations and numerical results," Lawrence Livermore National Laboratory, Livermore, California (UCRL-51245).

2. R. J. Lytle, E. F. Laine, D. L. Lager, and D. T. Davis (1979), "Cross-borehole electromagnetic probing to locate high-contrast anomalies," *Geophysics*, Vol. **44**, No. 10, October.

3. W. Daily, A. Ramirez, D. LaBrecque, and J. Nitao (1992), "Electrical resistivity tomography of vadose water movement," *Water Resource Research*, Vol. **28**, pp. 1429–1442.

4. S. D. Nelson and E. Johansson (1995), "Single pass surface-to-borehole reconstruction," Lawrence Livermore National Laboratory, Livermore, California (UCRL-53868-95).

5. A. Ramirez, W. Daily, M. Butner, and D. LaBrecque (1997), "Electrical resistivity monitoring of the thermomechanical heater teat in Yucca Mountain," *Proc. of the Symp. on the Appl. of Geophysics to Eng. and Environmental Problems*, Reno, Nevada, Vol. **1**, pp. 11–20.

6. S. D. Nelson (1994), "Electromagnetic modeling for ground penetrating radar using finite difference time domain modeling codes," *Proc. on Advanced Microwave and Millimeter Wave Detectors*, SPIE Proceedings, Vol. **2275**, July.

7. J. E. Mast and E. M. Johansson (1994), "Three-dimensional ground penetrating radar imaging using multi-frequency diffraction tomography," *Proc. on Advanced Microwave and Millimeter Wave Detectors, SPIE Proceedings*, Vol. **2275**, July.

8. E. M. Johansson *et al.*, "Three-dimensional ground penetrating radar imaging using synthetic aperture time domain focusing," *Proc. on Advanced Microwave and Millimeter Wave Detectors, SPIE Proceedings*, Vol. **2275**, July.

9. J. J. Roberts, E. Carlberg, and W. Lin, " Electrical properties of tuff from the ESF as a function of water saturation and temperature," Lawrence Livermore National Laboratory, Livermore, California (UCRL-ID-129594).